

DESIGN OF SURFACE TEXTURES IN JOURNAL BEARINGS  
FOR OPTIMIZING OPERATIONAL PERFORMANCE

GESTALTUNG VON OBERFLÄCHENTEXTUREN IN  
GLEITLAGERN ZUR OPTIMIERUNG DES  
BETRIEBSVERHALTENS

Von der Fakultät für Maschinenwesen der Rheinisch-Westfälischen Technischen  
Hochschule Aachen zur Erlangung des akademischen Grades einer Doktorin der  
Ingenieurwissenschaften genehmigte Dissertation

vorgelegt von

YUJUN WANG

Berichter/in: Univ.-Prof. Dr.-Ing. Georg Jacobs  
Univ.-Prof. Dr.-Ing. Katharina Schmitz

Tag der mündlichen Prüfung: 06.01.2026

Diese Dissertation ist auf den Internetseiten der Universitätsbibliothek online verfügbar.



## **Preface**

This dissertation was written during my doctoral study at the Institute for Machine Elements and Systems Engineering (MSE) at RWTH Aachen University. I would like to thank the China Scholarship Council for supporting my doctoral study.

I would like to express my sincere gratitude to Univ.-Prof. Dr.-Ing. Georg Jacobs for his dedicated supervision and support throughout my doctoral study. His constructive and insightful guidance was indispensable to the successful completion of this work. I would like to thank Univ.-Prof. Dr.-Ing. Katharina Schmitz for serving as the second reviewer of my dissertation and as an examiner in my doctoral examination. I would also like to thank Univ.-Prof. Dr.-Ing. Christian Hopmann for chairing my doctoral examination.

I would like to thank all my colleagues at MSE for the enjoyable and productive time we spent together. In particular, I would like to thank Prof. Dr.-Ing. Florian König for the critical and inspiring discussions, and for his support throughout this work. I would also like to thank Dr.-Ing. Shuo Zhang for his fruitful discussions during the development of numerical models. I also thank Benjamin Klinghart for his support and stimulating discussions on this work. I would also like to thank my colleagues, especially Stephan von Goedel, Mebus Lukas, Seyedmohammad Vafaei, Marius Bürger, Florian Wirsing, Ankit Singh, Merle Reimers, Ankit Saxena, Nico Gregarek, Yelvin Ragimov, Dr.-Ing. Dennis Bosse, Dirk Hamacher, Benjamin Lehmann, Markus Gilges, Julian Thao Baszenski, Pierre Kosoris, Thomas Petrzik, Mattheus Lucassen and Youchun Wang, for the open exchange and the supportive working environment. I would like to thank Jenny Teßmann for her organizational support in completing this work. I would also like to thank my students, whose curiosity and innovative discussions contributed to this work.

My heartfelt thanks go to my parents, Shiping Wang and Anhua Chen, and to my sister, Yuxia Wang, for their unconditional encouragement and support throughout my doctoral journey. Their love has always been my greatest motivation to keep going.

Aachen, in January 2026

Yujun Wang



## Summary

The growing demand for energy efficiency and power density in machinery requires journal bearings to have lower friction losses (FL) and higher load-carrying capacities (LCC). Surface textures on the sliding surface in a journal bearing have shown their promising results in both the reduction of FL and the improvement of LCC. However, the improper design of texture parameters is reported to be detrimental to both parameters.

Although numerous studies have been conducted to apply surface textures into journal bearings, the method to properly design surface textures in journal bearings is primarily constrained by inadequate prediction models and trial-and-error design methods. Therefore, a validated design method of surface textures in journal bearings is becoming essential.

This dissertation proposes a strategy to design surface textures in journal bearings with the aim of a higher LCC and a lower FL. The design strategy integrates three sub-models for textured journal bearings: the Navier-Stokes based mixed-elastohydrodynamic lubrication (mixed-EHL) model for the accurate prediction of LCC and FL, the machine learning-based surrogate model for the efficient prediction of LCC and FL, and the multi-objective optimization model to determine the design parameters of textures to achieve a higher LCC and a lower FL.

The results show that the proposed design strategy works successfully for different lubrication conditions of journal bearings. With the optimized texture design parameters, the FL is reduced by approximately 11.97% under the hydrodynamic lubrication condition and 10.39% under the mixed lubrication condition in this work. Meanwhile, the minimum film thickness is slightly increased by 1.46% under the hydrodynamic lubrication condition and 1.38% under the mixed lubrication condition, which indicates the slightly increased LCC.

The design strategy in this work offers a comprehensive approach in analyzing and designing surface textures in the application of journal bearings. It provides in-depth insights into the lubrication mechanisms of textured journal bearings and aids in the proper design of textured journal bearings for given operating conditions.

## Zusammenfassung

Die zunehmende Nachfrage nach Energieeffizienz und Leistungsdichte in Maschinen und Anlagen erfordert Gleitlager, die durch niedrigere Reibungsverluste (engl. friction losses, FL) und höhere Tragfähigkeiten (engl. load-carrying capacities, LCC) charakterisiert sind. Forschungsarbeiten haben ergeben, dass Oberflächentexturen auf der Gleitfläche eines Gleitlagers eine vielversprechende Methode darstellen, um sowohl die Reduktion von FL als auch eine Verbesserung der LCC zu erreichen. Allerdings bedingt eine fehlerhafte Auslegung der Oberflächentexturparameter negative Auswirkungen auf FL und LCC.

Obwohl zahlreiche Studien zur Anwendung von Oberflächentexturen in Gleitlagern durchgeführt wurden, wird die Methode zur richtigen Auslegung von Oberflächentexturen in Gleitlagern in erster Linie durch unzureichende Vorhersagemodelle und Trial-and-Error-Designmethoden beschränkt. Daher gewinnt eine validierte Designmethode für Oberflächentexturen in Gleitlagern zunehmend an Bedeutung.

Die vorliegende Dissertation schlägt eine Strategie zur Auslegung von Oberflächentexturen in Gleitlagern vor, mit dem Ziel, die FL zu minimieren und die LCC zu maximieren. Dabei integriert die Auslegungsstrategie drei Teilmodelle für texturierte Gleitlager. Das erste Teilmodell ist das auf Navier-Stokes basierende gemischte elastohydrodynamische Schmiermodell (engl. mixed-EHL), das eine genaue Vorhersage von LCC und FL ermöglicht. Das zweite Teilmodell ist ein auf maschinellem Lernen basierendes Ersatzmodell, das eine effiziente Vorhersage von FL und LCC ermöglicht. Das dritte Teilmodell ist ein multiobjektives Optimierungsmodell, das zur Bestimmung der Auslegungsparameter von Texturen dient, um niedrigere FL und höhere LCC zu erreichen.

Die Ergebnisse zeigen, dass die vorgeschlagene Designstrategie unter verschiedenen Schmierbedingungen von Gleitlagern erfolgreich funktioniert. Mithilfe der optimierten Oberflächentextur erfolgt eine Reduktion der FL um etwa 11,97 % unter hydrodynamischen Schmierbedingungen und um 10,39 % unter Mischreibungsbedingungen. Gleichzeitig wurde eine Erhöhung der minimalen Schmierfilmdicke unter hydrodynamischen Schmierbedingungen um 1,46 % und unter Mischreibungsbedingungen um 1,38 % beobachtet, wodurch auf eine leicht erhöhte LCC geschlossen werden kann.

Die in dieser Arbeit dargelegte Designstrategie präsentiert einen umfassenden Ansatz zur Analyse und Gestaltung von Oberflächentexturen bei der Anwendung von Gleitlagern. Die vorliegende Arbeit liefert fundierte Einblicke in die Schmiermechanismen texturierter Gleitlager und unterstützt bei der richtigen Auslegung von Gleitlagern mit Oberflächentexturen für bestimmte Betriebsbedingungen.

---

## Content

Summary.....	I
Zusammenfassung.....	II
Content.....	III
Nomenclature.....	VII
Abbreviations.....	XII
1.Introduction.....	1
2.Problem statement.....	3
3.State of research.....	5
3.1. Tribological system of journal bearings.....	5
3.2. Lubrication mechanisms of textured journal bearings.....	7
3.2.1. Single-texture contact.....	7
3.2.2. Textured journal bearings.....	10
3.3. Numerical models of textured journal bearings.....	12
3.3.1. Numerical models of textured contacts.....	12
3.3.2. N-S based CFD models for various lubrication regimes.....	14
3.4. Design of textured journal bearings.....	18
3.4.1. Design parameters of surface textures.....	18
3.4.2. Machine learning models for textured journal bearings.....	21
3.4.3. Optimization design method of textured journal bearings.....	22
3.5. Identification of research needs.....	24
4.Research concept.....	27
4.1. Research questions.....	27
4.2. Solutions.....	27
5.Numerical model of textured journal bearings.....	31
5.1. Theoretical background of the mixed-EHL model.....	32
5.1.1. Governing equation of fluid flow.....	32

- 5.1.2. Governing equation of solid deformation ..... 33
- 5.1.3. Governing equation of surface roughness..... 34
- 5.1.4. Governing equation of shaft movement..... 36
- 5.1.5. Simulation procedure..... 38
- 5.2. Mesh independence study..... 44
- 5.3. Experimental validation ..... 46
  - 5.3.1. Validation of minimum film thickness and pressure distribution 46
  - 5.3.2. Validation of friction loss ..... 49
- 6. Influence of textures on the film thickness and friction loss of journal bearings 53
  - 6.1. Influence of textures under hydrodynamic lubrication ..... 54
    - 6.1.1. Influence on the minimum film thickness and friction loss ..... 55
    - 6.1.2. Lubrication mechanism analysis..... 56
  - 6.2. Influence of textures under mixed lubrication ..... 64
    - 6.2.1. Influence on the minimum film thickness and friction loss ..... 64
    - 6.2.2. Lubrication mechanism analysis..... 67
- 7. ML-based surrogate model of textured journal bearings .....79
  - 7.1. Input and output parameters ..... 79
  - 7.2. Theoretical background of ML-based surrogate model ..... 80
    - 7.2.1. Model structure..... 80
    - 7.2.2. Performance evaluation ..... 82
  - 7.3. Model setup..... 83
    - 7.3.1. Determination of the network architecture ..... 83
    - 7.3.2. Determination of initial weights and biases ..... 85
  - 7.4. Results and discussion..... 87
    - 7.4.1. ANN model under the hydrodynamic lubrication..... 87
    - 7.4.2. ANN model under the mixed lubrication..... 91
- 8. Optimization design of textured journal bearings.....97
  - 8.1. Theoretical background of optimization model..... 97

---

8.2.	Model setup .....	99
8.3.	Results and discussion .....	100
8.3.1.	Optimization results for hydrodynamic lubrication .....	100
8.3.2.	Optimization results for mixed lubrication .....	102
9.	Summary and outlook .....	105
9.1.	Summary .....	105
9.2.	Outlook .....	108
10.	Appendix .....	109
10.1.	Governing equations of cavitation .....	109
10.2.	Governing equations of deformation .....	109
10.3.	Governing equations of surface roughness .....	110
11.	References .....	113



## Nomenclature

Latin characters

Character	Description	Unit
$a_x^t, a_y^t$	Accelerations of the shaft in $x$ and $y$ directions at time step $t$	$\text{m}\cdot\text{s}^{-2}$
$cov$	Texture coverage angle	$^\circ$
$C$	Bearing clearance	mm
$d_c$	Distance to the centre of film in the roughness-viscosity model	m
$d_t$	Texture depth	mm
$d_{k,l}(d)$	Radial nodal deformation vector in the EHS method	m
$D$	Inner diameter of journal bearing	mm
$D_{i,j}^{k,l}$	Influence coefficient matrix in the EHS method	-
$e$	Eccentricity of shaft	-
$E_1, E_2$	Elastic moduli of the shaft and bearing	Pa
$E^*$	Reduced elastic modulus	Pa
$f_a$	Friction due to the asperity contact	$\text{N}\cdot\text{m}$
$f_h$	Friction due to the fluid	$\text{N}\cdot\text{m}$
$f_{total}$	Total friction	$\text{N}\cdot\text{m}$
$F$	Load-carrying capacity	N
$F_x, F_y$	Load-carrying capacities in $x$ and $y$ directions	N
$F_{a,x}, F_{a,y}$	Load-carrying generated by asperity contact capacities in $x$ and $y$ directions	N
$F_{hx}, F_{hy}$	Load-carrying capacities generated by hydrodynamic effect in $x$ and $y$ directions	N

## Nomenclature

---

$h$	Film thickness	m
$h_{min}$	Minimum film thickness	m
$H_s$	Dimensionless film thickness	-
$\bar{I}$	Unit tensor	-
$K$	Elastic factor in the contact model	-
$L$	Width of journal bearing	mm
$L_{ext}$	External load on the bearing system	N
$m$	Mass of shaft	Kg
$MSE$	Mean square error	-
$n_j$	Radial reticulate layer for each mesh node	-
$n_{total}$	Total number of radial reticulate layers in the oil film gap domain	-
$\vec{n}$	Normal distance to the wall	-
$O_b, O_s$	Center of bearing and shaft	-
$p$	Superposition of hydrodynamic pressure and asperity contact pressure	Pa
$\bar{p}$	Specific pressure	Pa
$p_a$	Asperity contact pressure	Pa
$p_{i,j}$	Nodal pressure in the EHS model	Pa
$p_{in}$	Inlet pressure	MPa
$p_h$	Hydrodynamic pressure	MPa
$p_{sat}$	Saturation pressure	Pa
$p_{out}$	Outlet pressure	MPa
$r_b$	Radius of the journal bearing	mm
$r_s$	Radius of the shaft	mm
$R$	Correlation coefficient of the ANN model	-

---

$Re$	Reynolds number	-
$Re_k$	Roughness Reynolds number	-
$R_a$	Arithmetic mean roughness	$\mu\text{m}$
$R_q$	Root-mean-square roughness	$\mu\text{m}$
$S_v$	Gravity term	$\text{Pa/m}$
$u_s$	Sliding speed of the textured contact	$\text{m}\cdot\text{s}^{-1}$
$\mathbf{U}_m$	Velocity vector of the mixture	$\text{m}\cdot\text{s}^{-1}$
$U_{rot}$	Rotational speed	rpm
$V_x, V_y$	Motion speeds of the shaft in $x$ and $y$ directions, respectively	$\text{m}\cdot\text{s}^{-1}$
$w_t$	Texture width	mm
$W$	Distance between textures	mm
$\Delta x^t, \Delta y^t$	displacements of the shaft in $x$ and $y$ directions, respectively	m
$x, y, z$	Coordinates	m

Greek characters

<b>Character</b>	<b>Description</b>	<b>Unit</b>
$\alpha$	Starting angle of texture zone	$^\circ$
$\bar{\beta}_s$	Mean summit radius of asperity	m
$\gamma$	Mass fraction of vapor	-
$\bar{\delta}_s$	Combined mean asperity summit height	m
$\bar{\delta}_{s,1}, \bar{\delta}_{s,2}$	Mean summit height of surface 1 and surface 2, respectively	m
$\zeta_s$	Summit density of asperity	-
$\eta$	Dynamics viscosity	$\text{Pa}\cdot\text{s}$
$\eta_l$	Dynamic viscosity of lubricant	$\text{Pa}\cdot\text{s}$

---

## Nomenclature

---

$\eta_m$	Mixture viscosity	Pa·s
$\eta_s$	Roughness-viscosity	Pa·s
$(\theta, z)$	Circumferential and axial coordinates of the fluid domain in the EHS method	-
$(\theta', z')$	Circumferential and axial coordinates of the solid domain in the EHS method	-
$\kappa_l$	Kinematic viscosity of lubricant	mm <sup>2</sup> s <sup>-1</sup>
$\kappa_v$	Kinematic viscosity of vapor	mm <sup>2</sup> s <sup>-1</sup>
$\mu_{bound}$	Boundary friction coefficient	-
$\nu_1, \nu_2$	Poisson's ratios of the shaft and bearing, respectively	-
$\rho_l$	Density of lubricant	kg·m <sup>-3</sup>
$\rho_{l,sat}$	Density of lubricant at saturation pressure	kg·m <sup>-3</sup>
$\rho_m$	Mixture density	kg·m <sup>-3</sup>
$\rho_v$	Density of vapor	kg·m <sup>-3</sup>
$\rho_{v,sat}$	Density of the vapor at saturation pressure	kg·m <sup>-3</sup>
$\sigma_s$	Combined asperity summit roughness of journal and bearing	m
$\sigma_{s,1}, \sigma_{s,2}$	Asperity summit roughness of surface 1 and surface 2, respectively	m
$\bar{\tau}$	Shear stress tensor induced by fluid	Pa
$\tau_a$	Asperity shear stress	Pa
$\Psi_l$	Compressibility of lubricant	s <sup>2</sup> ·m <sup>-2</sup>
$\Psi_m$	Mixture compressibility	s <sup>2</sup> ·m <sup>-2</sup>
$\Psi_v$	Compressibility of vapor	s <sup>2</sup> ·m <sup>-2</sup>
$\omega$	Angular velocity of rotation	rad/s
$\Omega$	Interface between the solid domain and fluid domain	-

## Subscript

<b>Character</b>	<b>Description</b>
<i>a</i>	Asperity contact under mixed lubrication
<i>b</i>	Bearing
<i>h</i>	Hydrodynamic condition
<i>in</i>	Inlet
<i>j</i>	Mesh index for the radial reticulate layer
<i>l</i>	Properties of lubricant
<i>out</i>	Outlet
<i>m</i>	Mixture of lubricant and vapor
<i>max</i>	Maximum
<i>min</i>	Minimum
<i>t</i>	Texture
<i>s</i>	Shaft
<i>sat</i>	Saturation condition
$(i,j)$	Mesh indexes of fluid domain
$(k,l)$	Mesh indexes of solid domain
<i>v</i>	Properties of vapor
<i>x</i>	<i>x</i> direction
<i>y</i>	<i>y</i> direction
<i>z</i>	<i>z</i> direction

## Superscript

<b>Character</b>	<b>Description</b>
$(k,l)$	Mesh indexes of solid domain
<i>t</i>	Time index
0	Initial time step

## Abbreviations

<b>Abbreviation</b>	<b>Description</b>
ANN	Artificial Neural Network
CFD	Computational Fluid Dynamics
EHS	Elastic Half Space
EHL	Elasto-hydrodynamic lubrication
FL	Friction loss
GA	Genetic algorithm
HL	Hydrodynamic lubrication
ISO	International Organization for Standardization
LCC	Load-carrying capacity
Mixed-EHL	Mixed-ElastoHydrodynamic Lubrication
<i>MSE</i>	Mean Square Error
N-S	Navier-Stokes equations
NSGA-II	Non-Dominated Sorting Genetic Algorithm-II
OpenFOAM	Open-source Field Operation and Manipulation, a free and open-source CFD software developed primarily by OpenCFD Ltd
<i>purelin</i>	Pure linear function
<i>Re</i>	Reynolds number
RQ	Research question
<i>ReLU</i>	Rectified linear unit function
<i>Sigmoid</i>	Logistic sigmoid function
<i>tanh</i>	Hyperbolic tangent function

## 1. Introduction

With the global increase in energy prices and energy consumption, the demand for energy efficiency of machinery is growing. Approximately 20% of the world total energy consumption is used to overcome friction induced by various tribological contacts [1,2]. Among these contacts, journal bearings have attracted significant attention for their wide range of potential applications, including various subsystems in engines and powertrains [3,4].

The function of journal bearings is to carry external loads while enabling relative motion between the contacting surfaces through the formation of a lubricating film [5,6]. The shearing of the lubricant at the interface as well as the mixed friction lead to friction losses and thereby affect the energy efficiency of the machine [7]. Accordingly, when evaluating the lubrication performance of journal bearings, two key-parameters are commonly employed: load-carrying capacity (LCC) and friction loss (FL) [8]. In this context, this dissertation primarily focuses on the load-carrying capacities provided by journal bearings and their friction losses.

Nowadays, the growing demand for energy efficiency requires lower FL and higher LCC in journal bearings [9]. To achieve aforementioned requirements of journal bearings, surface texturing, among various solutions, has drawn significant interest [10]. Surface texturing is defined as the intentional introduction of well-defined, regularly patterned dimples or grooves on the bearing surface, as illustrated in Figure 1.1 [11]. These dimples or grooves are collectively named as surface textures. Textures can be manufactured using laser techniques, chemical etching, electric discharge methods and focused ion beams [12].

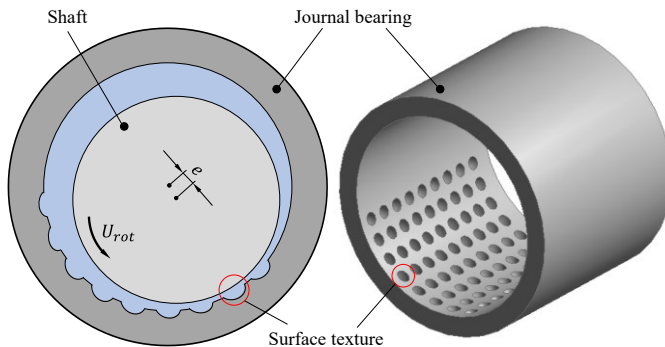


Figure 1.1 Schematic picture of a textured journal bearing

Several beneficial effects of surface textures have been identified in previous research. Surface textures can act as lubricant reservoirs and reduce the contact area [13,14]. Moreover, surface textures can generate an additional micro-hydrodynamic pressure, which contributes to an increase in the LCC [15,16]. Given these beneficial effects, surface textures are considered as a promising way to reduce the FL and increase the LCC of journal bearings.

## 2. Problem statement

The successful applications of surface textures to reduce the FL and increase the LCC in journal bearings have been reported [3,13,17,18]. However, improperly designed textures can also be detrimental to both the FL and LCC of journal bearings [19–21]. For example, as shown in Figure 2.1, the friction coefficient of the textured journal bearing is increased compared to that of the non-textured journal bearing [19]. Furthermore, the textures reduce the load-carrying capacity of the hydrodynamic lubricant film within the bearing, as can be observed by the increase of transition speed from 80 rpm for the non-textured bearing to 100 rpm for the textured bearing.

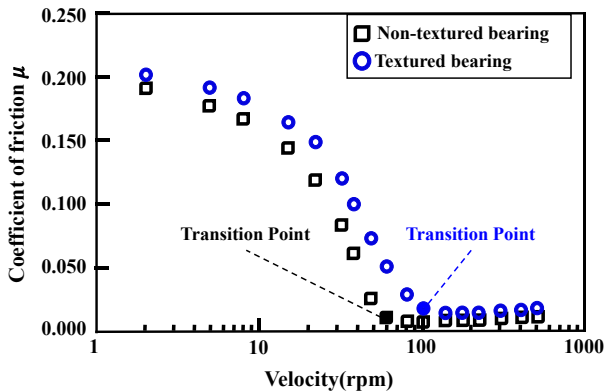


Figure 2.1 Increased friction by improperly designed textures, reproduced from [19]

Therefore, despite the promising potential of surface textures reported in previous studies, there still remains a risk that improperly designed textures could negatively influence the friction behavior and the load-carrying capacity of journal bearings. The previous study reported that improper texture designs can lead to an increase in FL by more than 14% and a reduction in LCC by more than 29% [22]. Therefore, the aim of this dissertation is to develop

### **A method to design surface textures in journal bearings for low friction loss and high load-carrying capacity**

To address this aim, the understanding of the state of research on textured journal bearings is imperative, which is discussed in the following chapter.



### 3. State of research

This chapter begins with a broad overview of journal bearings. Furthermore, it provides the current state of research on the lubrication mechanisms of textured journal bearings, which explains how surface textures influence the lubrication performance of journal bearings. Finally, it presents the state of research on the prediction and design methods of textured journal bearings.

#### 3.1. Tribological system of journal bearings

As mentioned in Chapter 1, the function of journal bearings is to carry external loads and enable relative motion between the contacting surfaces through the formation of a lubricating film. A journal bearing system can be regarded as a tribological system, which is sketched in Figure 3.1 [23,24].

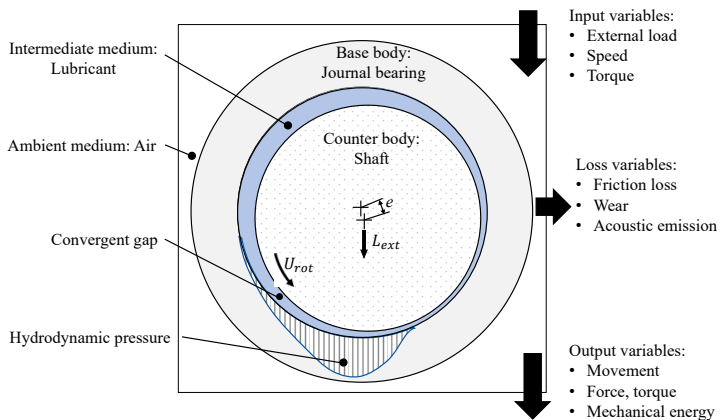


Figure 3.1 Tribology system of a journal bearing based on [23,24]

A journal bearing system consists of a stationary journal bearing as the base body and a rotating shaft as the counter body. The lubricant serves as the intermediate medium. The air surrounding the journal bearing in this example acts as the ambient medium. The input variables of the journal bearing system are the rotational speed of the shaft, and the external load acting on the shaft. In this work, the bearing operates under a static load, therefore the fatigue problem caused by the dynamic load is not discussed. The rotating shaft transports the lubricant into a convergent gap due to the eccentricity ( $e$ ) between the bearing and the shaft. The convergent gap leads to the

generation of hydrodynamic pressure. The LCC of the journal bearing is contributed by the integration of the hydrodynamic pressure over the contacting surface.

In addition to the LCC, the external load on the bearing system and the rotating shaft induce shear stress within the lubricating film. This further leads to the friction loss (FL) [25]. Based on the FL, the state of friction can be classified into three lubrication regimes according to the STRIBECK curve [26]. The STRIBECK curve describes the friction as a function of the dynamic viscosity ( $\eta$ ), the shaft rotational speed ( $U_{rot}$ ), and the specific pressure  $\bar{p}$  which is defined as Eq. (3-1).

$$\bar{p} = \frac{L_{ext}}{D \cdot L} \tag{3-1}$$

where  $L_{ext}$  is the external load on the bearing system;  $D$  and  $L$  are the inner diameter and width of the journal bearing, respectively.

The three lubrication regimes according to the STRIBECK curve are defined as follows [27,28] (see Figure 3.2):

- Hydrodynamic lubrication (HL) regime: The lubricant film can completely separate the two contacting surfaces. When the journal bearing operates under a high external load, the resulting high hydrodynamic pressure leads to a significant elastic deformation of the solid body. When the elastic deformation is of the same order of magnitude as the lubricant film thickness, the lubrication regime is specifically referred to as the elasto-hydrodynamic lubrication (EHL) regime.
- Mixed lubrication regime: The lubricant film cannot completely separate the contacting surfaces. The asperity interactions occur between the two contacting surfaces.
- Boundary lubrication regime: The lubricant film cannot be formed or sustained. The two surfaces are in contact and the asperity interactions dominate.

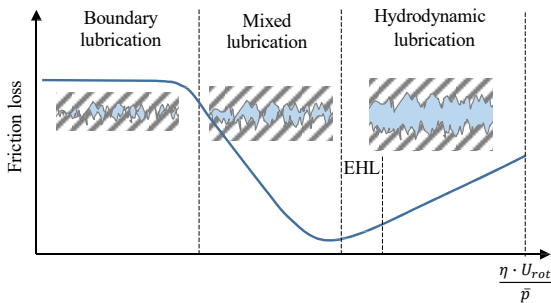


Figure 3.2 STRIBECK curve and classification of lubrication regimes

Journal bearings are typically designed to operate under the hydrodynamic lubrication regime. However, new applications of journal bearings, such as wind turbine drivetrains, often operate under high loads and low rotational speeds. According to Figure 3.2, these operating conditions increase the proportion of operation subject to the mixed lubrication, thereby leading to the higher FL. In this context, this dissertation introduces surface textures into journal bearings to reduce the FL and improve the LCC under different lubrication regimes. The current state of research on the lubrication mechanisms of textured journal bearings, which explains how surface textures influence the FL and LCC of journal bearings, is discussed in the following subchapter.

## **3.2. Lubrication mechanisms of textured journal bearings**

To elucidate how surface textures influence tribological contacts, numerous studies have been conducted to identify the underlying mechanisms. It has been reported that the lubrication mechanisms of surface textures are highly application-dependent and have not been fully clarified until now [21]. In this subchapter, four widely discussed and well-accepted mechanisms in single-texture contacts are introduced first. Subsequently, the state of the art regarding the lubrication mechanisms of textured journal bearings is summarized.

### **3.2.1. Single-texture contact**

Single-texture contact is the cell contact with one individual dimple, which enables to capture the detailed flow phenomena inside the texture. Four widely discussed and well-accepted mechanisms in single-texture contact are as follows.

#### **(a) Inlet suction effect**

As one of the earliest lubrication mechanisms, the so-called ‘inlet suction effect’ (also known as ‘entrainment suction effect’) was proposed by Fowell et al. [29] and Olver et al. [30]. They hypothesized that the lower pressure generated by the entrance zone of the texture induced a larger amount of lubricant flowing into the contact, as shown in Figure 3.3. This larger flow rate through the textured contact further enhanced the pressure ( $p$ ) build-up at the outlet [29–31]. This enhanced pressure thus increased the LCC, which was integrated by the pressure ( $p$ ).

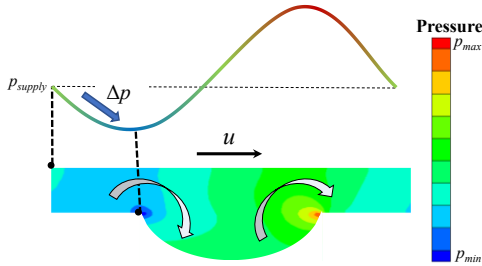


Figure 3.3 Schematic picture for inlet suction effect [29]

**(b) Cavitation effect**

Another mechanism is the so-called ‘cavitation effect’, which was first proposed by Hamilton et al. [32] and Estion et al. [33]. As shown in Figure 3.4, the pressure decreases at the entrance of the texture due to the sudden increase in flow area, followed by a positive pressure rise downstream because of the convergence of flow area. In the pressure-drop zone, if the pressure falls below the lubricant’s saturation pressure, a so-called ‘cavitation’ occurs. When the cavitation occurs, the pressure-drop is limited by the saturation pressure, leading to an asymmetric pressure [34]. Moreover, after the cavitation region, the dissolution of the gaseous phase slows the film reformation. Therefore, compared to the scenario without considering cavitation, the pressure increase after the cavitation region is delayed [35]. Simultaneously, the maximum pressure generated by the texture decreases [35]. In summary, the influence of the cavitation effect depends on the shape of the asymmetric pressure distribution [11]. When the pressure is overall positive, the positive pressure can lead to an increased separation between the surfaces [36].

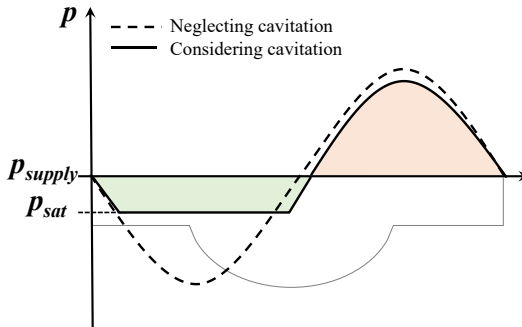


Figure 3.4 Schematic picture for cavitation effect, reproduced from [11]

### (c) Inertia effect

Another widely accepted mechanism is the so-called ‘inertia effect’. In most cases, the inertia effect is negligible when analyzing the lubrication performance of journal bearings. However, under conditions with high sliding speed, high lubricant density, high film clearance, and low viscosity, the inertia effect becomes significant [37,38]. These parameters can be summarized in the Reynolds number ( $Re$ ):

$$Re = \frac{\rho_l \cdot u_s \cdot C}{\eta_l}$$

where  $u_s$  is the sliding speed of the textured contact;  $C$  is the clearance of the contact;  $\rho_l$  is the density of the lubricant;  $\eta_l$  is the dynamic viscosity of the lubricant.

For the textured contact, the enlarged clearance ( $C$ ) leads to a higher  $Re$  value, which indicates a stronger inertia effect [39,40]. The pressure distributions at lower and higher  $Re$  values are shown in Figure 3.5 [41]. Compared to the antisymmetric pressure at the lower  $Re$  value, a positive load-carrying capacity is generated at the higher  $Re$  value. Consequently, this effect becomes considerable when analyzing the textured contact. This conclusion is also in agreement with the findings by other researchers [42,43].

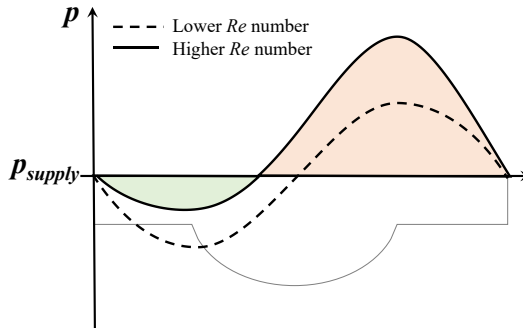


Figure 3.5 Schematic picture for inertia effect, reproduced from [41]

### (d) Vortex effect

In addition to the three aforementioned effects, vortices have also been observed within textures both experimentally and numerically, as shown in Figure 3.6 [44,45]. Furthermore, studies have shown that vortices can considerably affect the lubrication performance of textured contacts. The vortices can affect the cavitation zone and further influence the hydrodynamic pressure generated by textures [46,47]. Xie et al.

[48] also pointed out that the vortices influenced the pressure distribution within textures and further affected the local load-carrying capacity by textures. Therefore, when elucidating the lubrication mechanism of textures in journal bearings, the influence of vortices should be fully taken into consideration.

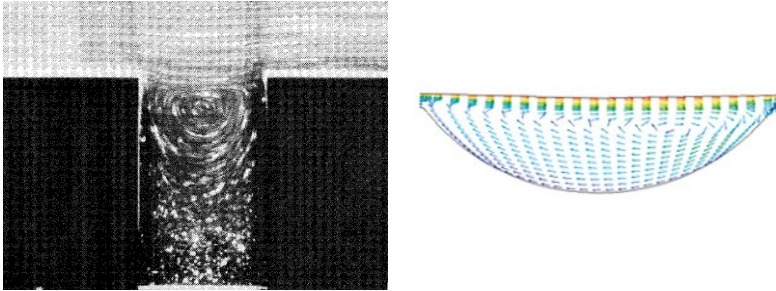


Figure 3.6 Vortices observed experimentally [44] and numerically [45]

In summary, four texture-induced microflow effects have been identified when analyzing the effect of a single texture on sliding contacts. An error of nearly 20% in the load-carrying capacity has been reported when texture-induced microflow related effects were neglected [49]. Therefore, to accurately predict the lubrication performance of textured contacts working across a wide range of operating conditions, all four texture-induced microflow effects introduced above should be considered.

### 3.2.2. Textured journal bearings

The aforementioned studies on the texture-induced microflow effects were mainly based on single-texture contacts. However, textured journal bearings in practical applications always contain multiple textures. In this section, the interactions between multiple textures as well as their interactions with journal bearings are summarized.

#### (a) Interactions between multiple textures

Based on the lubrication mechanism of the single-texture contact, a straightforward deduction is that the pressure distribution induced by multiple textures is a repetition of the pressure distribution induced by the single texture, as illustrated by the black line in Figure 3.7. However, from the pressure distribution of multiple textures illustrated by the blue line, the pressure induced by the successive texture is based on the pressure induced by the previous texture [11].

This deviation can be attributed to the interactions between textures. Specifically, the local differences in pressure and the potential perturbations of lubricant flow between textures can significantly affect the pressure build-up [50]. Consequently, the

aforementioned mechanisms for the single-texture contact cannot be directly applicable to textured journal bearings. This highlights the necessity of considering the interactions between multiple textures.

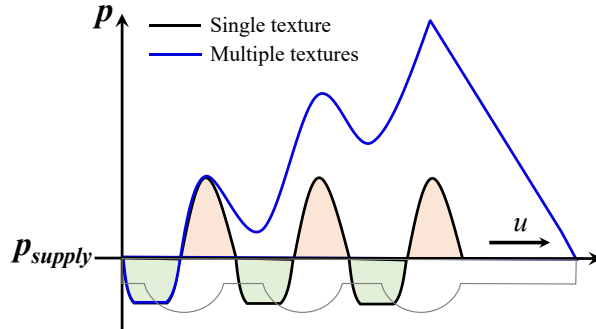


Figure 3.7 Schematic pressure distributions for single texture and multiple textures reproduced from [11]

### (b) Interactions between multiple textures and journal bearings

As introduced in Chapter 3.2.1, the microflow effects induced by textures can influence the local LCC and thereby affect the formation of the lubricating film in journal bearings. In turn, the microflow within textures is also reported to be influenced by the lubricating film. The cavitation effect is dependent on the local pressure of the lubricating film at textures [51]. Sahlin et al. [42] showed that the generation of vortices within textures was influenced by texture depth as well as the flow in the local lubricating film at textures. In addition, it has been reported that the inertia effect and the inlet suction effect highly depend on the operating conditions of the lubricating film [29,52].

In summary, the interactions between multiple textures considerably affect the pressure build-up, and further influence the FL and LCC of journal bearings. Moreover, the texture-induced microflow effects can influence the formation of the local lubricating film in journal bearings. Conversely, the flow within the lubricating film also influences these microflow effects in the textures. This demonstrates the interactions between the texture-induced microflow and the lubricating film in journal bearings.

To accurately predict the FL and LCC of textured journal bearings, all texture-induced microflow effects should be fully considered. Additionally, the interactions between multiple textures should be considered when predicting the FL and LCC of

journal bearings. Moreover, the interactions between the texture-induced microflow and the bearing lubricating film should be considered at the whole-bearing level.

### **3.3. Numerical models of textured journal bearings**

When predicting the FL and LCC of textured journal bearings, both texture-induced microflow effects and texture-interaction effects should be involved. In this subchapter, the numerical models of textured journal bearings are summarized.

#### **3.3.1. Numerical models of textured contacts**

In terms of the numerical prediction of textured contacts, two numerical models are commonly used: the Reynolds equation model and the Navier-Stokes (N-S) equations model [14]. The Reynolds equation is a simplified version of the N-S equations, derived by neglecting the inertia effect and the flow in the direction of film thickness [26]. Both the Reynolds equation and N-S equations are classified as partial differential equations. Since the closed-form analytical solutions are only available for simple geometries and flow regimes, solving these equations requires a multi-level iterative numerical approach [53]. This solution process is referred to as Computational Fluid Dynamics (CFD).

The numerical solution based on CFD begins with discretizing the fluid domain into small and interconnected cells or volumes. These small and interconnected cells or volumes are collectively referred to as the mesh [54]. Figure 3.8 schematically illustrates the differences in mesh discretization required by the N-S equations model compared with the Reynolds equation model. In contrast to the N-S equations model, the Reynolds equation model does not require the mesh discretization in the direction of film thickness, thus significantly reducing the number of mesh elements. Therefore, the Reynolds equation requires less computational cost and is more straightforward to implement due to the simplification [55]. Consequently, the numerical models based on the Reynolds equation constitute 77% of previous research on textured surfaces [11].

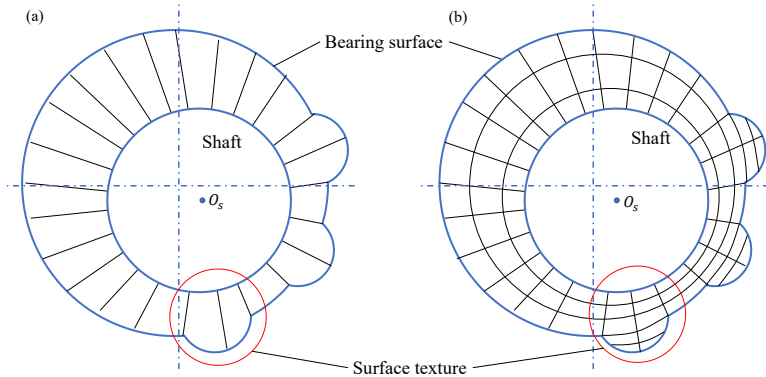


Figure 3.8 Mesh discretization of textured journal bearings: (a) Required by Reynolds equation (b) Required by N-S equations

However, the simplification of the Reynolds equation leads to limitations in the prediction of textured contacts [56]. Dobrica and Fillon [40] concluded that the Reynolds equation was invalid for textured sliders when the ratio between the length and depth of the texture was small (less than 10 in their case) and the Reynolds number was large. Li and Chen [49] reported that the Reynolds equation was inapplicable when the texture depth was higher than 10% of the film thickness. In their study, the load-carrying capacity predicted by the Reynolds equation was 20% lower than that obtained by more precise N-S equations. Wen et al. [55] conducted a comparison between the N-S equations and Reynolds equation models in the textured contacts and found differences in both the minimum film thickness and pressure distribution. The necessity of the N-S based prediction on the textured contacts has also been demonstrated in the studies by Keller et al. [57], Wang et al. [58] and Cohen et al. [59].

To elucidate the underlying reasons for the aforementioned differences, a detailed comparison between the Reynolds equation and the N-S equations in predicting the textured surfaces is concluded in Table 3.1. When predicting the LCC and FL of textured journal bearings, the Reynolds equation is not able to consider the inertia effect [39–43] and the vortex effect [44–48,60]. Consequently, the interaction effect between the texture-induced microflow and the bearing film formation also cannot be fully considered by the Reynolds equation. In contrast, the N-S equations can simultaneously consider all the texture-induced microflow effects and interaction effects. Therefore, to accurately predict the LCC and FL of textured journal bearings, the N-S based CFD model is more appropriate.

Table 3.1 Comparison of Reynolds equation and N-S equations in predicting the performance of textured surfaces

	Reynolds	N-S
<b>Texture-induced microflow effects</b>		
(a) Inlet suction effect	✓	✓
(b) Cavitation effect	✓	✓
(c) Inertia effect	✗	✓
(d) Vortex effect	✗	✓
<b>Interaction effects</b>		
(a) Between multiple textures	✓	✓
(b) Between the microflow and bearing film	Inaccurate	✓

### 3.3.2.N-S based CFD models for various lubrication regimes

Given the high accuracy of the N-S based CFD model, its applications to the textured journal bearings are presented in this section. When predicting the LCC and FL of textured journal bearings, the accuracy of the numerical model depends on its ability to capture the flow behavior of the lubricant. When applying the N-S based CFD model to journal bearings operating under various lubrication regimes, the following behaviors are essential to be considered.

#### (a) Cavitation

Cavitation is a phenomenon in fluid flow where the static pressure of a liquid falls below its saturation pressure ( $p_{sat}$ ), causing the formation of vapor bubbles [61]. Therefore, when the cavitation occurs, the lubricating oil becomes a mixture of liquid and vapor. As introduced in Subchapter 3.2.1, the cavitation effect is a critical flow behavior within textures. Besides, the distribution of the cavitation zone can significantly influence the pressure build-up and the friction behavior of the whole journal bearing [62]. Therefore, the cavitation effect is essential for capturing the flow behavior in textured journal bearings and needs to be considered into the N-S based CFD model.

#### (b) Load-balance

In addition, as introduced in the previous section, compared to the Reynolds equation, the N-S equations can consider the flow across the film thickness and the

inertia effect. Therefore, the solution of the N-S equations needs to account for an additional flow dimension and incorporate inertia effect [26]. Consequently, solving the N-S equations becomes more challenging. As a result, most existing N-S based CFD models have been simplified by assuming a fixed eccentricity ( $e$ ) and attitude angle ( $\varphi$ ) of the journal bearing, as shown in Figure 3.9 (a). In this way, the LCC is predicted as an output parameter for a given eccentricity and attitude angle. Therefore, this method neglects the equilibrium between LCC of the bearing and the external load [63]. However, setting a fixed eccentricity ratio and attitude angle makes it difficult to evaluate the journal bearings from a system's perspective, as the external load ( $L_{ext}$ ) and the speed ( $U_{rot}$ ) are system properties to define the operating condition [24,63], as shown in Figure 3.9 (b). Different operating conditions lead to different eccentricity ratios and attitude angles. Therefore, a so-called 'load-balance model', which considers the equilibrium between the LCC of the bearing and the external load, should be incorporated into the N-S based CFD model.

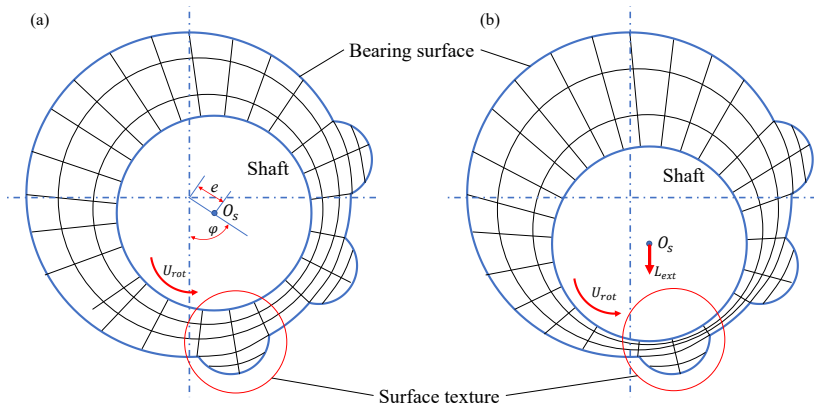


Figure 3.9 Schematic mesh for a journal bearing: (a) with the fixed eccentricity ratio and attitude angle (b) with the external load

To incorporate the load-balance model, the equilibrium between the LCC of the bearing and the external load is evaluated during the solution of the N-S equations. When the LCC cannot achieve equilibrium with the external load, the shaft moves. As a result, this movement changes the entire fluid domain. Since the N-S equations require modeling the flow across the whole lubricating film, the mesh for the entire fluid domain must be updated with the changed fluid domain [64]. To achieve this, the mesh-updating method (also known as dynamic mesh method) needs to be incorporated into the N-S based CFD model. This poses significant challenges to incorporate the load-balance model in the N-S based CFD model.

### **(c) Deformation and surface roughness**

Moreover, in many applications, including combustion engines and wind turbines, journal bearings may operate with higher loads and lower rotational speeds. These operating conditions may lead to an insufficient lubricating film thickness and asperity contact between the bearing and the shaft. This induces a considerable deformation of the bearing and the occurrence of direct asperity contact of surface roughness [65]. This condition is referred to as mixed-elastohydrodynamic lubrication (mixed-EHL). Therefore, the wide range of operating conditions causes journal bearings to operate from the HL regime to the mixed-EHL regime. This requires the further development of the N-S based CFD model which can predict the LCC and FL of the textured journal bearings from HL to mixed-EHL conditions. Therefore, in addition to the load-balance model, the elastic deformation as well as the surface roughness models should also be included into the N-S based CFD model.

Current applications of N-S based CFD models in textured journal bearings are preliminarily summarized in Table 3.2. It shows that the cavitation model has been widely included in the N-S based CFD models. However, until now, the applications of N-S based CFD models to textured journal bearings are primarily limited to the hydrodynamic lubrication regime without considering the load-balance model [11,63]. Only a few studies have developed elasto-hydrodynamic lubrication (EHL) models that include the elastic deformation of textured journal bearings [66]. One study was found to include both the elastic defamation and surface roughness, but without considering the load-balance model. Therefore, an N-S based CFD model which can accurately predict the performance of textured journal bearings from HL to mixed-EHL conditions is still missing.

Table 3.2 State of research on N-S based CFD models for textured journal bearings

		Cavitation	Load- balance	Deformation	Surface roughness
HL	Xie et al. [18,48]				
	Vilhena et al. [56]	✓	✗	✗	✗
	Han et al. [67]				
	Others [68–71]				
EHL	Zhang et al.[66]				
	Meng et al. [72]				
	Tauviqirrahman et al. [73]	✓	✗	✓	✗
	Hameed et al. [74]				
	Lin et al. [75]	✓	✓	✓	✗
Mixed- EHL	Muchammad et al. [76]	✓	✗	✓	✓

In summary, the N-S based CFD model is more accurate in predicting the performance of textured journal bearings compared with the Reynolds equation. The current N-S based CFD models are primarily limited to the hydrodynamic lubrication regime. Further development of the N-S based CFD model is essential to promote the application of textures in journal bearings under various lubrication conditions, particularly the mixed-EHL condition. However, to the best of the authors' knowledge, such a model does not exist until now.

Nevertheless, the N-S based CFD model compromises computational efficiency due to the dramatic increase in mesh cell numbers and the above-introduced multi-level iterative solution. This issue becomes even more critical under mixed lubrication conditions due to the additional consideration of elastic deformation, surface roughness and load-balance models. This high computational cost limits the rapid evaluation of potential texture configurations. Therefore, to facilitate the practical design of textured journal bearings, it is essential to integrate this highly accurate N-S-based CFD model into an efficient design strategy, which will be discussed in the following subchapter.

### 3.4. Design of textured journal bearings

Although the high accuracy of the N-S based CFD model is widely recognized, its computational efficiency has been criticized. To address this issue and integrate the N-S based CFD model into the design of textured journal bearings, this subchapter discusses current design methods for textured journal bearings. It begins with the determination of design parameters of surface textures. Following that, the efficient prediction methods of textured journal bearings are discussed. At last, the optimization design methods are presented.

#### 3.4.1. Design parameters of surface textures

In order to design surface textures for journal bearings, the critical design parameters should first be determined. Extensive studies in recent decades have concluded that the design parameters mainly encompass two aspects: geometry parameters and distribution parameters [77], as illustrated schematically in Figure 3.10. The effect of each parameter is discussed in detail below.

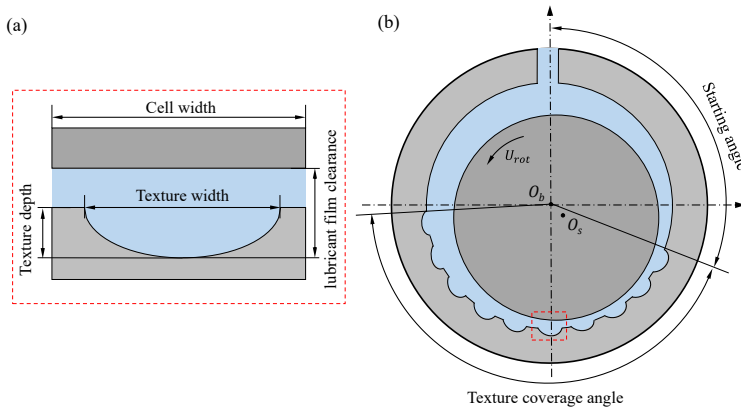


Figure 3.10 Schematic of a textured journal bearing: (a): Geometry parameters (b): Distribution parameters

#### (a) Geometry parameters

As an important geometry parameter of surface textures, the effect of texture depth has been widely studied. Zhang et al. [78] compared the variation in the LCC as a function of the texture depth. They found that as the texture depth increased, the LCC of the textured journal bearing initially increased and then decreased. This result confirmed the existence of an optimal texture depth under the specific operating

condition. The significant effect of texture depth on the journal bearings and the existence of an optimal texture depth were also reported by Guo et al. [79], Sharma et al. [80], and Mehrjardi et al. [81].

In addition to the texture depth, the texture width has also been reported as a critical parameter. Texture width determines the texture density for a given texture distribution and influences the pressure formation around a unit dimple. Mao et al. [82] compared the maximum oil film pressure and friction loss for different texture widths. In their case, an increase in texture width raised the dimensionless maximum oil film pressure (defined as the ratio of the maximum hydrodynamic pressure to the ambient pressure) by around 20%, while the friction loss was reduced by 35%. This indicated the significant effect of texture width on both the LCC and FL of journal bearings. This significant effect was also reported by other researchers [83–85].

Based on the texture depth and width, the texture geometry can be characterized by three dimensionless parameters [40]: texture depth ratio (the ratio of the texture depth to the lubricant film clearance), texture width ratio (the ratio of the texture width to the unit cell width), and aspect ratio (the ratio of the texture width to the texture depth). In this work, the lubricant film clearance and the cell width remain fixed. Consequently, when the texture depth ratio and the texture width ratio are specified, the aspect ratio is thereby determined. Therefore, the primary geometry parameters considered in this work are the texture depth ratio and the texture width ratio.

In studies of textured journal bearings, various texture shapes have also been investigated, including circular, triangular, rectangular, and hexagonal forms [86]. However, given current manufacturing techniques, circular textures are most commonly fabricated and thus represent the most widely used shape [87,88]. Therefore, this dissertation focuses exclusively on circular textures.

### **(b) Distribution parameters**

As pointed out by Arif et al. [89], the textured distribution can significantly affect the LCC and FL of journal bearings, and under certain cases even more than the textured geometry.

In studies on the effect of the texture distribution, the primary comparison is between fully textured and partially textured distributions. A fully textured distribution is defined as one in which textures cover the entire circumference of the bearing surface. In contrast, a partially textured distribution covers only a portion of the bearing surface circumference. Dobrica et al. [50] compared these two distributions and concluded that the fully textured bearings exhibited worse performance than the non-textured bearings, whereas the partially distributed textures

had the potential to improve the LCC and reduce the FL of journal bearings. This finding was later confirmed by Khatri et al. [90] and Tala-Ighil et al. [21].

For a partially textured bearing, the texture coverage angle serves as a distribution parameter, defined as the circumferential angle of the textured area on the bearing surface. By comparing 24 partially textured bearings with a non-textured bearing, Tala-Ighil et al. [21] found that when textures were distributed downstream of the hydrodynamic pressure field, partially distributed textures could generate a beneficial effect on the LCC. Kango et al. [91] observed that the texture coverage angle had a significant impact on the FL of journal bearings. At a low bearing eccentricity, as the texture coverage angle increased, the FL first decreased and then increased.

Subsequently, Gui and Meng [92] compared the effect of the texture coverage angle on the LCC and FL in both pressure-rising and pressure-falling fields. They found that the effect of the texture coverage angle was dependent on the starting angle of the textured area. This suggests that texture distribution parameters should account for both the starting angle and the coverage angle of the textured area.

### **(c) Interaction effect between various design parameters**

In addition to separate studies on the individual influence of the texture geometry and the texture distribution on the LCC and FL of journal bearings, the interaction between these two aspects has also been reported. Tala-Ighil et al. [22] investigated the influence of the texture width and distribution on the bearing performance. The results indicated that the effect of the texture width on the LCC and FL was dependent on the texture distribution. Subsequently, the synergic effect of the texture depth and texture distribution were investigated by Liang et al. [68]. They found that shallow textures were better for the convergent area, while deep textures were better for the divergent area. Additionally, the interaction between the texture geometry and the texture distribution has also been reported by other researchers [48,93].

The aforementioned findings reveal that both the geometry and distribution parameters of textures can generate a considerable effect on the LCC and FL of journal bearings. Therefore, the design of surface textures in journal bearings should consider both aspects. In addition, the interaction between various design parameters has been observed. These complexities present the high degree of freedom in design parameters of surface textures.

As concluded from subchapter 3.3, the N-S based CFD model is more accurate in predicting the LCC and FL of textured journal bearings. However, the N-S based CFD model compromises the computational efficiency. Consequently, given the high degree of freedom in texture design parameters, the prediction of textured journal

bearings requires a huge amount of computational cost from the N-S based CFD model. Therefore, to facilitate the practical design of textured journal bearings, an efficient prediction method for textured journal bearings is required, which will be discussed in the next subchapter.

### **3.4.2. Machine learning models for textured journal bearings**

As an alternative to numerical models, recent advances in machine learning (ML)-based surrogate models have shown significant potential in terms of computational efficiency. ML-based surrogate models are the statistical models developed using machine learning methods. Once successfully trained, the surrogate models can predict the desired outputs with high accuracy and with a much lower computational cost than that required by numerical models [94–96]. Therefore, these models have attracted growing attention in the fields of journal bearings and surface textures [97].

ML-based surrogate models have been successfully utilized in the performance prediction of journal bearings. Moschopoulos et al. [98] developed a ML procedure to predict the loading condition based on the sound and vibration data. Hess and Shang [99] presented an artificial neural network (ANN) model to approximate the pressure distribution of a journal bearing. Baş and Karabacak [100] compared three different ML methods for predicting the friction of radial journal bearings, including ANN, support vector machine, and regression trees. Their results showed that the ANN model achieved the highest prediction accuracy.

In addition to its applications in journal bearings, ML has also shown the potentials in textured contacts. Otero et al. [101] developed an ANN model to predict the friction coefficient of the textured surface in a ball-on-disc contact. Marian et al. [102] applied ML to qualitatively feature the influence of micro-textures in a single EHL contact, which was a tribological approximation model of rolling bearings. Li et al. [103] compared five ML algorithms for predicting the friction coefficient of sliding friction pairs with textures. According to their results, the ANN also achieved the highest prediction accuracy. However, from the literatures, the studies in which ML techniques are applied to the performance prediction of textured journal bearings are still new.

When applying ML-based surrogate models to textured journal bearings, the accuracy of the surrogate models is highly dependent on the accuracy and amount of training datasets [104,105]. As previously mentioned, the N-S based CFD model can provide training data more accurately, but it imposes a high computational burden. In addition, the high degree of freedom in design parameters of textures means that a large amount of training data is required, which further increases the time

requirements. Therefore, to predict the LCC and FL of textured journal bearings accurately and efficiently, it is crucial to explore a method that can improve the prediction accuracy of ML models without requiring additional training datasets.

In summary, ML-based surrogate models offer the potential capability to efficiently predict the LCC and FL of journal bearings. However, due to the limitation of the generation of training datasets, this efficient ML-based surrogate model has not been accurately and efficiently obtained.

### **3.4.3. Optimization design method of textured journal bearings**

Based on the aforementioned ML-based surrogate models, the relationship between texture design parameters and both the LCC and FL can be accurately and efficiently predicted. Given this relationship, the design of textured journal bearings requires the appropriate determination of optimal texture design parameters for journal bearings. The determination of optimal design parameters should be driven by the optimization objectives. According to the literature, surface textures can efficiently reduce the friction loss in journal bearings [3]. However, surface textures may also decrease the load-carrying capacity of journal bearings [11,60]. Consequently, when optimizing textured journal bearings, the objectives should include reducing the friction loss, while increasing or maintaining the load-carrying capacity. Driven by these optimization objectives, the commonly utilized optimization methods of textured journal bearings are summarized in this subchapter.

#### **(a) Single-variable parameter study**

Current optimization studies on textured journal bearings primarily employ the single-variable parameter study, in which the individual effect of each texture design parameter on the bearing performance is evaluated independently. Tala-Ighil et al. [21] examined 25 different texture distributions while keeping the texture geometry parameters constant. Singh et al. [106] compared 5 texture depths while keeping the texture distribution and width constant. Guo [107] optimized the LCC of bearings by varying the texture depth, width, and coverage. He conducted three sets of comparisons: 7 different texture widths while keeping the depth and coverage constant; 5 different texture depths while maintaining constant width and coverage; and 15 texture distributions with constant width and depth. The similar optimization design of textures based on the single-variable parameter study was also conducted by Refs. [80,108,109].

From the single-variable parameter study, optimal values for each texture parameter are obtained separately, forming an optimal texture configuration. However, this approach is often insufficiently accurate since each parameter's optimal value is

determined while the other parameters remain constant. From the aforementioned studies in Subchapter 3.4.1, there are interactions between texture design parameters [22,48,68,93]. This means the optimal value of each parameter may change as other parameters vary. A possible approach to achieving globally optimal results through the single-variable parameter study is the full-factorial design method [110]. For example, four texture design parameters, each having 10 levels, yield  $10^4$  possible combinations. By comparing the LCC and FL of all  $10^4$  combinations, the optimal combination might be identified. However, this full-factorial design method is inefficient due to extensive prediction time required and the numerous design parameters involved. Consequently, the design of surface textures in journal bearings still remains at the trial-and-error stage [13].

### (b) Optimization algorithm

Optimization algorithms offer an efficient way to address the above issue [111]. Among various optimization algorithms, the genetic algorithm (GA) has been widely used in the optimization design of textured parameters in journal bearings, as shown in Table 3.3. GA is an optimization method inspired by Darwinian's principles of natural selection and survival of the fittest individuals [112]. It employs mathematical tools to evolve a population of candidate solutions over successive generations. It excels in exploring complex search spaces and adapting to diverse problem domains [113].

Table 3.3 Studies employing GA in optimization design of textured journal bearings

Studies	Design parameters	Objectives
Zhang et al. [114,115]	Texture distribution	Minimizing friction coefficient
Shen et al.[116]	Texture depth	Minimizing friction coefficient
Xu et al. [117]	Texture depth Texture width	Maximizing the sum of inverse of friction and maximizing pressure
Khatri et al. [118]	Texture depth Texture distribution	Minimizing the sum of stability speed, the critical mass and the frictional torque

However, when it comes to handling the multi-objective optimization, the traditional GA is limited by its difficulty in effectively evaluating and balancing multiple objectives simultaneously [119]. The general approach to multiple-objective optimization by GA is to combine the individual objective functions into a single composite function [119]. As shown in Table 3.3, Khatri et al. [118] optimized the

textured depth and distribution with three objective parameters. During their optimization procedure, the objective function was defined as the sum of these three objective parameters. As a result, the optimization process may be biased toward solutions that favor certain objectives over others, rather than providing a balanced compromise among all objectives. Therefore, this aggregation is limited to handle the trade-offs among multiple, especially potentially competing objectives [120]. To address this issue, an efficient multi-objective optimization approach should be considered when designing textured journal bearings.

Due to this reason, the non-dominated sorting genetic algorithm-II (NSGA-II) was developed from the traditional GA approach. This method can generate solutions that are not inferior to any other candidates across all objectives. This means that the NSGA-II directly manages the trade-offs among multiple objectives instead of combining them into a single criterion [121]. Because of its advantages for the multi-objective optimization, this algorithm has shown promising results in the optimization design of textures in thrust bearings [122–124] and seals [125–128]. However, the multi-objective optimization of textured journal bearings based on this algorithm still remains to be explored.

In summary, the design of textured journal bearings is driven by multiple objectives, including the lower FL and the higher LCC. However, the commonly used single-variable parameter study is inefficient due to the extensive time required and the numerous design parameters involved. In addition, the traditional GA optimization method is limited to the single-objective optimization. Therefore, an efficient multi-objective optimization model is needed for the design of textured journal bearings.

### **3.5. Identification of research needs**

Although numerous studies have been conducted to apply surface textures into journal bearings, the methods for properly designing surface textures in journal bearings are primarily constrained by inadequate prediction models and trial-and-error design methods. To address this problem, the state of research is summarized and the research needs are then derived.

#### **(a) Research needs to accurately predict the LCC and FL of textured journal bearings under various lubrication conditions**

An error of nearly 20% in the LCC has been reported when texture-induced microflow-related effects were neglected. Therefore, to accurately predict the LCC and FL of textured journal bearings, the texture-induced microflow effects as well as the interaction effects between the microflow and bearing lubricating film should be

considered by employing a N-S based CFD model. However, the current N-S based CFD model is primarily limited to the HL regime. To promote the application of textures in journal bearings under various conditions, particularly under mixed lubrication conditions, a further development of the N-S based mixed-EHL model is essential to integrate the solid deformation, surface roughness and load-balance models with the N-S equations.

**(b) Research needs to efficiently predict the LCC and FL of textured journal bearings considering interactions between texture design parameters**

The texture design parameters include geometry and distribution parameters. The interactions among these parameters results in a high degree of freedom in texture design parameters. This high degree of freedom requires a huge amount of computational cost from the N-S based CFD model. Therefore, to design textured journal bearings, the LCC and FL of journal bearings under different texture parameters should be predicted not only accurately but also efficiently.

**(c) Research needs to optimize textured journal bearings with the aim of reducing the friction loss and increasing the load-carrying capacity**

Although surface textures have demonstrated promising results in reducing FL of journal bearings, their detrimental effect on the LCC has also been reported. Therefore, a multi-objective optimization should be considered in the design of textured journal bearings. However, the single-variable parameter study is inefficient due to the extensive time required and the numerous design parameters involved. Therefore, an efficient multi-objective optimization model is needed for the design of textured journal bearings.



## 4. Research concept

### 4.1. Research questions

Although surface textures are considered a promising way to enhance the LCC and reduce the FL of journal bearings, improperly designed textures have a negative effect on journal bearings. Therefore, the objective of this work is defined as:

#### **Development of a design method for surface textures in journal bearings**

To approach this objective, the main research question (RQ) is derived from the identified research needs:

**Main RQ:** How can we optimize both the friction and load-carrying capacity of journal bearings by designing and locating surface textures?

To answer this main RQ, two sub-RQs should be answered:

**Sub-RQ1:** How can we accurately predict the load-carrying capacity and friction loss of textured journal bearings with the consideration of texture-induced microflow effects and interactions between multiple textures?

**Sub-RQ2:** How can we efficiently predict the load-carrying capacity and friction loss of textured journal bearings with the consideration of interactions between design parameters of textures?

### 4.2. Solutions

To answer these three research questions, the following solutions can be identified from the current state of research in this work:

1. The N-S based CFD method is more accurate in predicting the LCC and FL of textured journal bearings under different lubrication conditions compared with the Reynolds equation. (identified from Chapter 3.3)
2. ML-based surrogate models can efficiently predict the LCC and FL of textured journal bearings. (identified from Chapter 3.4.2)
3. Multi-Objective Genetic Algorithm can be used to optimize texture parameters with the goal of reducing the FL and improving the LCC. (identified from Chapter 3.4.3)

Consequently, a model strategy is proposed in this work based on the above solutions, which includes three sub-models:

- a) N-S based mixed-EHL model (N-S based CFD model for various lubrication conditions)
- b) ML-based surrogate model
- c) Multi-objective optimization model

Each sub-model addresses a specific research question. All these three sub-models are organized into five chapters, as shown in Figure 4.1.

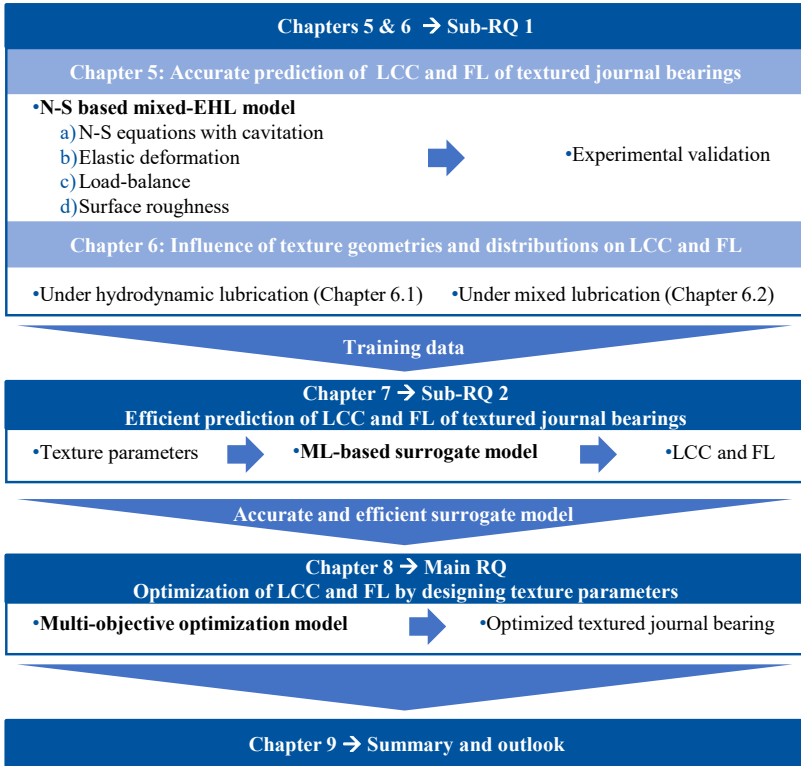


Figure 4.1 Structure of this work

To answer the sub-RQ 1, the N-S based mixed-EHL model for textured journal bearings is developed in Chapter 5. The current N-S based models are primarily limited to the hydrodynamic lubrication regime. Therefore, the N-S based mixed-EHL model is developed by integrating elastic deformation, surface roughness and load-balance models with the N-S equations. Eventually, the developed model is capable

of predicting the LCC and FL of textured journal bearings from (elasto-)hydrodynamic lubrication to mixed lubrication. Therefore, it is named as 'mixed-EHL' model. In Chapters 5.1 and 5.2, the theoretical background and setup of the developed mixed-EHL model are introduced, respectively. With this model, the LCC and FL of textured journal bearings can be accurately predicted considering the texture-induced microflow effects and interactions between multiple textures under different lubrication conditions. Subsequently, the experimental validation is conducted to verify the accuracy of the N-S based mixed-EHL model in Chapter 5.3. After the validation, in Chapter 6, this model is used to analyze the influence of texture geometries and distributions on the LCC and FL of journal bearings under two lubrication regimes: hydrodynamic lubrication and mixed lubrication.

The successful answer to sub-RQ 1 provides the basis for answering sub-RQ 2. Using the experimentally validated mixed-EHL model, the input and output parameters are defined and the training datasets are generated for the ML-based surrogate model, which is introduced in Chapter 7.1. Then, the theoretical background of ML-based surrogate model is introduced in Chapter 7.2. Subsequently, the architecture parameters as well as the initial weights and biases of the surrogate model are determined for the model setup in Chapter 7.3. The ML-based surrogate model is utilized to efficiently predict both the LCC and FL while considering the interaction between texture design parameters in Chapter 7.4. Therefore, this surrogate model answers the sub-RQ 2.

Eventually, based on the ML-based surrogate model, the multi-objective optimization model is developed in Chapters 8.1 and 8.2. Subsequently, in Chapter 8.3, the multi-objective optimization model based on the NSGA-II is utilized to optimize both the LCC and FL of journal bearings by designing texture parameters. Therefore, the main RQ can be answered and a design method for surface textures in journal bearings will be available.



## 5. Numerical model of textured journal bearings

The textured journal bearing is schematically depicted in Figure 5.1. It is composed of a smooth shaft and a journal bearing with surface textures. The smooth shaft rotates in an anti-clockwise direction with a rotational speed ( $U_{rot}$ ), while the textured bearing stays stationary. The external load ( $L_{ext}$ ) is applied vertically on the shaft. The oil is pumped into the thin clearance between the shaft and bearing from the upper inlet hole with the inlet pressure ( $p_{in}$ ) and flows out from both sides with the ambient pressure ( $p_{out}$ ). Within the thin lubricant film, hydrodynamic pressure is generated to separate the rotating shaft and the stationary bearing.

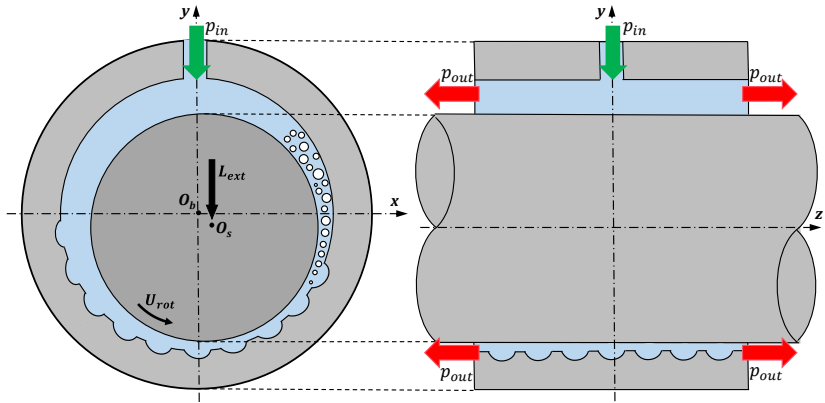


Figure 5.1 Schematic representation of a textured journal bearing

As aforementioned in the Chapter 3.3, when predicting the LCC and FL of textured journal bearings, the N-S based CFD model is more accurate compared with the Reynolds equation. However, the current N-S based CFD model is primarily limited to the hydrodynamic lubrication regime. Further development of the N-S based CFD model is essential to promote the application of textures in journal bearings under various lubrication conditions, including the mixed-EHL condition. However, such a model does not yet exist. To address this limitation, the N-S based mixed-EHL model is developed to predict the LCC and FL of textured journal bearings from the hydrodynamic lubrication regime to the mixed-EHL regime. The theoretical background is presented in the following subchapter.

## 5.1. Theoretical background of the mixed-EHL model

In this subchapter, the theoretical background of the N-S based mixed-EHL model for textured journal bearings is introduced. It starts with the governing equations of fluid flow and solid deformation, followed by modelling the effects of surface roughness and the load balance. The contribution and novelty of this model lie in integrating and connecting the models of deformation, load balance, and surface roughness with the N-S equations. To the best of the author's knowledge, this is the first N-S based CFD model capable of predicting the LCC and FL of textured journal bearings from the hydrodynamic lubrication regime to the mixed-EHL regime.

### 5.1.1. Governing equation of fluid flow

The governing equations of fluid flow are introduced in this subchapter. All the equations of fluid flow are solved in OpenFOAM, which is an open-source CFD package [129]. As introduced in Subchapter 3.3.2, one important flow behavior in textured journal bearings is the cavitation effect, which occurs when the pressure falls below the saturation pressure ( $p_{sat}$ ) [61]. The occurrence of cavitation can significantly influence the pressure build-up and friction behavior of textured journal bearings [62].

In this work, the homogeneous equilibrium cavitation model in OpenFOAM is used, which assumes the mixture of liquid and vapor to be in a mechanical and thermodynamic equilibrium [57]. Details about the cavitation model can be found in the Appendix 10.1. The outcome of this cavitation model is the mass fraction of vapor  $\gamma$ . With the value of  $\gamma$ , the mixture density  $\rho_m$  and the mixture viscosity  $\eta_m$  can be determined.

Combined with the cavitation model, the N-S equations are used to compute the fluid flow. The N-S equations consist of the mass and momentum conservation equations [130]:

$$\frac{\partial}{\partial t}(\rho_m) + \nabla \cdot (\rho_m \mathbf{U}_m) = 0 \quad (5-1)$$

$$\frac{\partial}{\partial t}(\rho_m \mathbf{U}_m) + \nabla \cdot (\rho_m \mathbf{U}_m \mathbf{U}_m) - \nabla \cdot \left( \underbrace{\bar{\tau}}_{shear\ stress} \right) = -\nabla p_h + S_v \quad (5-2)$$

where  $\mathbf{U}_m$  is the velocity vector of the mixture;  $p_h$  is the hydrodynamic pressure;  $S_v$  is the gravity term.

In this dissertation, the lubricant is assumed to be a general Newtonian fluid, whose viscosity is independent of shear stress [130]. Under this assumption, the shear stress term  $\bar{\tau}$  can be expressed as Eq. (5-3):

$$\bar{\tau} = \eta_m [\nabla \mathbf{U}_m + (\nabla \mathbf{U}_m)^T] + \frac{2}{3} \nabla \cdot \mathbf{U}_m \cdot \bar{\mathbf{I}} \quad (5-3)$$

where  $\bar{\mathbf{I}}$  is the unit tensor, and the second term on the right-hand side is the effect of volume dilation.

By solving the N-S equations (Eqs. (5-1)~(5-3)), the hydrodynamic pressure field ( $p_h$ ) and the velocity field ( $\mathbf{U}_m$ ) can be determined.

### 5.1.2. Governing equation of solid deformation

Solid deformation is usually neglected in existing N-S-based CFD models of journal bearings, as these models focus only on HL conditions [20,58,87–90,92–94]. However, the new application with the high load necessitates the consideration of surface deformation in journal bearings. In this section, by considering the deformation, the existing N-S based CFD models are extended to predict the LCC and FL of textured journal bearings under EHL conditions.

In this work, this deformation is calculated using the Elastic Half Space (EHS) method, which has been widely adopted to calculate the deformation of journal bearings based on the Reynolds equation [131,132]. According to the EHS method, the deformation of two elastic contacting surfaces (bearing and shaft in this study) can be simplified to a total elastic normal deformation  $d(\theta', z')$ . The total elastic normal deformation  $d(\theta', z')$  induced by a given pressure field  $p(\theta, z)$  can be expressed as:

$$d(\theta', z') = \frac{1}{\pi E^*} \iint_{\Omega} \frac{p(\theta, z)}{\sqrt{((\theta' - \theta)r_b)^2 + (z' - z)^2}} d\theta dz. \quad (5-4)$$

where  $\Omega$  denotes the interface between the solid and fluid domains,  $\theta$  and  $z$  are the circumferential and axial coordinates of the fluid domain,  $\theta'$  and  $z'$  are the circumferential and axial coordinates of the solid domain. Additionally,  $E^*$  is the reduced Young's modulus;  $p$  is a superposition of the hydrodynamic pressure ( $p_h$ , introduced in Chapter 5.1.1) and the asperity contact pressure ( $p_a$ , will be introduced in Chapter 5.1.3). The calculations of  $p$  and  $E^*$  are given by Eq. (5-5) and Eq. (5-6), respectively:

$$p = \underbrace{p_h}_{\text{hydrodynamic pressure}} + \underbrace{p_a}_{\text{asperity contact pressure}} \quad (5-5)$$

$$E^* = \left( \frac{1 - \nu_1^2}{E_1} + \frac{1 - \nu_2^2}{E_2} \right)^{-1} \quad (5-6)$$

where  $E_1$  and  $E_2$  are the elastic moduli of the shaft and bearing, respectively.  $\nu_1$  and  $\nu_2$  are the Poisson's ratios of the shaft and bearing, respectively. More details about the EHS method are provided in Appendix 10.2.

As a conventional way, the computational complexity of Eq. (5-4) can be reduced by constructing an influence coefficient matrix  $D_{i,j}^{k,l}$ . To compute the influence coefficient matrix  $D_{i,j}^{k,l}$ , the randomly distributed pressure within each mesh element is estimated using a zero-order shape function, as detailed in [133]. Thus, the normal nodal deformation vector  $d_{k,l}$  can be calculated by multiplying  $D_{i,j}^{k,l}$  and the nodal pressure vector  $p_{i,j}$ , as expressed in Eq. (5-7) [26,133]:

$$d_{k,l} = \frac{1}{\pi E^*} \sum_{i=1}^{N_c} \sum_{j=1}^{N_z} D_{i,j}^{k,l} p_{i,j} \quad (i, k = 1, 2, 3, \dots, N_c; j, l = 1, 2 \dots N_z) \quad (5-7)$$

where  $(i, j)$  and  $(k, l)$  are the mesh indexes of the fluid domain and solid domain,  $N_c$  and  $N_z$  are the mesh numbers in the circumstantial and axial directions,  $d_{k,l}$  is the calculated deformation at the solid domain with the mesh index  $(k, l)$  and  $p_{i,j}$  is the pressure at the fluid point with the mesh index  $(i, j)$ .

### 5.1.3. Governing equation of surface roughness

In addition to the solid deformation, another essential aspect to consider under high-load conditions is the effect of surface roughness. This effect includes two aspects: the effect on the contact pressure and the effect on the lubricant flow [134].

#### (a) Contact model

For the calculation of the asperity contact pressure, Greenwood and Tripp [135] proposed an asperity contact model, which was based on the contact of two nominally flat, random rough surfaces. The asperity contact pressure  $p_a$  can be calculated as:

$$p_a = KE^*F(H_s) \quad (5-8)$$

where  $E^*$  is the reduced elastic modulus, calculated using Eq. (5-6). The elastic factor  $K$  is a function that combines the roughness parameters of the contacting bodies, as detailed in Appendix 10.3.

The function  $F(H_s)$  relates the probability distribution of asperity height [136]:

$$F(H_s) = \begin{cases} 4.4086 \cdot 10^{-5} (4 - H_s)^{6.804} & \text{if } H_s < 4 \\ 0 & \text{if } H_s \geq 4 \end{cases} \quad (5-9)$$

where  $H_s$  is a dimensionless quantity that describes the ratio of the film thickness to the surface roughness height, which can be written as:

$$H_s = (h - \bar{\delta}_s) / \sigma_s \quad (5-10)$$

where  $\sigma_s$  is the combined asperity summit roughness of the shaft and bearing, which is defined as  $\sigma_s = \sqrt{\sigma_{s,1}^2 + \sigma_{s,2}^2}$ . The combined mean summit height  $\bar{\delta}_s$  can be defined as  $\bar{\delta}_s = \bar{\delta}_{s,1} + \bar{\delta}_{s,2}$ .  $h$  is the film thickness, which takes the elastic deformation of solid domain into consideration. The calculation of the elastic deformation has been detailed in Subchapter 5.1.2. As indicated by Eq. (5-9), if the  $H_s$  value is lower than 4, the asperity contact between the contact surfaces occurs, and the journal bearing is operating under the mixed lubrication condition.

### (b) Flow model

Except for the effect on the asperity contact pressure, the surface roughness can also generate a considerable effect on the lubricant flow under the mixed lubrication. A direct discretization of fluid equations (either the N-S equations or the Reynolds equation) on the scale of roughness requires extremely high mesh number. Given the computational resource nowadays, the simulation time would become unacceptable for journal bearings. Therefore, indirect methods were developed to consider the effect of surface roughness on lubricant flow [137,138].

Among these methods, the commonly used method in journal bearings is the so-called ‘average flow models’ introduced by Patir and Cheng [139,140]. In this model, the effect of surface roughness is considered by the pressure flow factors ( $\phi_{p,x}$  and  $\phi_{p,y}$ ) and the shear flow factor ( $\phi_s$ ). The pressure flow factors ( $\phi_{p,x}$  and  $\phi_{p,y}$ ) describe the flow due to pressure differences in the  $x$  (direction of motion) and  $y$  (axial) directions. The shear flow factor ( $\phi_s$ ) describes the flow caused by relative motion between two surfaces. The flow factors are influenced by the root-mean-square roughness ( $R_q$ ) and orientation of the surface. However, this model is derived from the Reynolds equation and is not applicable to the N-S equations [141].

To address this issue, the effect of surface roughness on the lubricant flow in this work is considered based on the roughness-viscosity model [142]. In this model, its effect on the lubricant flow is considered by a roughness-viscosity ( $\eta_s$ ). The ratio of the roughness-viscosity to the lubricant viscosity is given in Eq. (5-11). The roughness-viscosity ( $\eta_s$ ) is influenced by the lubricant viscosity ( $\eta_l$ ), the distance to the center of film ( $d_c$ ), the standard deviation of the surface roughness ( $R_q$ ) and  $Re$  number of the lubricant film. As  $d_c$  increases, the roughness-viscosity ( $\eta_s$ ) would have a higher value. This indicates the impact of surface roughness becomes stronger near the wall and gradually diminishes towards the center of the lubricant film. Therefore, this model considers the variation of roughness effects along the film thickness direction. As discussed in Subchapter 3.3, compared with the Reynolds equation, the N-S equations account for the flow in the thickness direction. Meanwhile, the presence of textures further enhances flow effects across the film thickness. Hence, this model is appropriate to incorporate the impact of roughness on fluid flow in this work. This model has been widely used in different applications [142–145].

$$\frac{\eta_s}{\eta_l} = A Re_k \frac{d_c}{R_q} \left[ 1 - \exp\left(-\frac{Re_k d_c}{Re R_q}\right) \right]^2 \quad (5-11)$$

where  $\eta_s$  is the roughness viscosity,  $\eta_l$  is the viscosity of lubricant,  $d_c$  is the distance to the centre of film,  $Re$  is the Reynolds number,  $A$  is a coefficient factor, and  $Re_k$  is the roughness Reynolds number. The calculation of  $A$  and  $Re_k$  follows a similar approach done by [142, 144] and is introduced in the Appendix 10.3.

The roughness-viscosity is superimposed with the lubricant viscosity. Therefore, when journal bearings operate under mixed lubrication conditions, the shear stress term in Eq. (5-3) is treated as:

$$\bar{\tau} = \left( \underbrace{\eta_m}_{\text{lubricant term}} + \underbrace{\eta_s}_{\text{roughness term}} \right) [\nabla \mathbf{U}_m + (\nabla \mathbf{U}_m)^T] + \frac{2}{3} \nabla \cdot \mathbf{U}_m \cdot \bar{\mathbf{I}} \quad (5-3^*)$$

#### 5.1.4. Governing equation of shaft movement

The elastic deformation of the shaft and bearing has been introduced in Section 5.1.2. In addition to the deformation, the shaft movement occurs under unbalanced load conditions. Under mixed lubrication conditions, the external force is carried by the hydrodynamic and asperity contact pressure of journal bearings [65]. The hydrodynamic pressure distribution of textured journal bearings is predicted by

solving the N-S equations in Eqs. (5-1) ~ (5-3). The asperity contact pressure is calculated by Eq. (5-8). Then, the load-carrying capacity of journal bearings can be calculated as:

$$F = \sqrt{(F_x)^2 + (F_y)^2}$$

$$\begin{cases} F_x = F_{h,x} + F_{a,x} = r_s \int_0^L \int_0^{2\pi} (p_h + p_a) \sin \theta \, d\theta dz \\ F_y = F_{h,y} + F_{a,y} = r_s \int_0^L \int_0^{2\pi} (p_h + p_a) \cos \theta \, d\theta dz \end{cases} \quad (5-12)$$

where  $F_{h,x}$  and  $F_{h,y}$  are the load-carrying capacities generated by the hydrodynamic effect in  $x$  and  $y$  directions, which are integrated from the hydrodynamic pressure ( $p_h$ ).  $F_{a,x}$  and  $F_{a,y}$  are the load-carrying capacities generated by the asperity contact in  $x$  and  $y$  directions, which are integrated from the asperity contact pressure ( $p_a$ ).

For one specific time step ( $t$ ), if the load-carrying capacity ( $F^t$ ) cannot achieve balance with the given external load ( $L_{ext}$ ), the shaft should move in the next time step ( $t + \Delta t$ ) until the load balance is achieved. Therefore, the movement of the shaft method is calculated as follows:

First, the acceleration of the shaft is calculated based on the imbalance between the load-carrying capacity and the external load:

$$\begin{cases} a_x^t = \frac{F_x^t - L_{ext,x}}{m} \\ a_y^t = \frac{F_y^t - L_{ext,y}}{m} \end{cases} \quad (5-13)$$

where  $a_x^t$  and  $a_y^t$  are the accelerations of the shaft in  $x$  and  $y$  directions at time step  $t$ , respectively;  $m$  is the mass of shaft;  $L_{ext,x}$  and  $L_{ext,y}$  are the external loads in  $x$  and  $y$  directions, respectively. Specifically, since the external load is applied vertically on the shaft in this work,  $L_{ext,x}$  is set to 0, as shown in Figure 5.1.

After that, the motion speed and the displacement of the shaft are calculated:

$$\begin{cases} V_x^t = V_x^{t-\Delta t} + a_x^t \cdot \Delta t \\ V_y^t = V_y^{t-\Delta t} + a_y^t \cdot \Delta t \end{cases} \quad (5-14)$$

$$\begin{cases} \Delta x^t = V_x^t \cdot \Delta t \\ \Delta y^t = V_y^t \cdot \Delta t \end{cases} \quad (5-15)$$

where  $V_x$  and  $V_y$  are the motion speeds of the shaft in  $x$  and  $y$  directions, respectively;  $\Delta x^t$  and  $\Delta y^t$  are the displacements of the shaft in these two directions, respectively. In this work,  $V_x^0$  and  $V_y^0$  are set to be zero to start the simulation.

### 5.1.5.Simulation procedure

In the previous subchapter, the governing equations of the N-S based mixed-EHL model have been introduced. In this section, the solution procedure is summarized. For this model, various input parameters should be specified before simulations. In this work, these input parameters are categorized into three groups: geometry parameters, operating parameters, as well as lubricant and material parameters.

The schematic geometry of a textured journal bearing is depicted in Figure 5.2. The geometry parameters of the textured journal bearing are listed in Table 5.1. The determination of texture geometry and distribution parameters is based on previous works in Refs. [21,48,50,60].

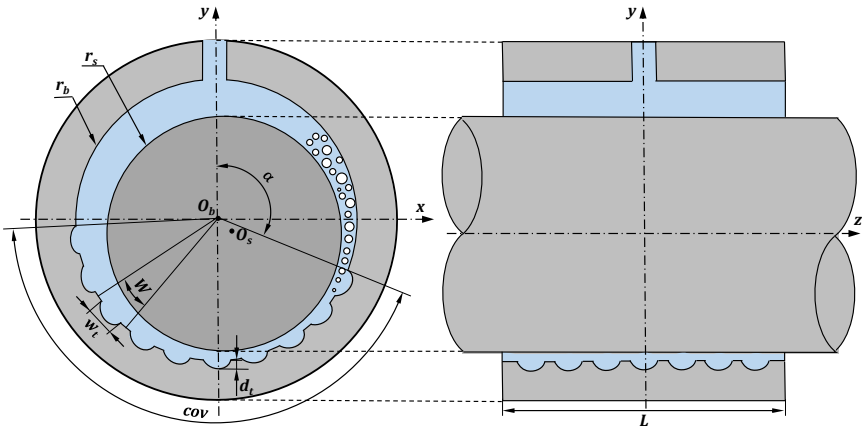


Figure 5.2 Schematic geometry of a textured journal bearing

Table 5.1 Geometry parameters of the textured journal bearing

Parameters	Value	Parameters	Value
Bearing radius $r_b$ [mm]	15	Starting angle of texture zone $\alpha$ [°]	5-180
Bearing width $L$ [mm]	20	Texture coverage angle $cov$ [°]	0-170
Shaft radius $r_s$ [mm]	14.97	Texture width ratio $w_t/W$ [-]	0.2-0.96
Clearance $C = r_b - r_s$ [mm]	0.03	Texture depth ratio $d_t/C$ [-]	0-3

The operating parameters studied in this work are listed in Table 5.2. To study the effects of textures under different lubrication conditions, two different rotational speeds are selected. The journal bearing works under the hydrodynamics lubrication at a rotational speed of 1,000 rpm, whereas it works under the mixed lubrication when the speed is reduced to 80 rpm.

Table 5.2 Operating parameters

parameters	Value	parameters	Value
External load $L_{ext}$ [N]	500	Rotational speed $U_{rot}$ [rpm]	80; 1,000
Inlet pressure $p_{in}$ [MPa]	0.3	Outlet pressure $p_{out}$ [MPa]	0.1

The lubricant and material parameters used in this work are listed in Table 5.3. These parameters are determined primarily based on the GLP30 test rig, which is introduced in Ref. [24]. The journal bearing is made of CuSn12Ni2-C-GBC with an average hardness of  $115.0 \pm 15.0$  HBW 5/250. The shaft sleeve is made of 100Cr6 (AISI 52100) with a hardness of 62 HRC. The bearing system is lubricated with the additive-free mineral oil “FVA 2” with a viscosity grade of ISO VG 32.

Table 5.3 Lubricant and material parameters

Lubricant properties			
Density of oil $\rho_l$ [ $\text{kg}\cdot\text{m}^{-3}$ ]	850	Density of vapor $\rho_v$ [ $\text{kg}\cdot\text{m}^{-3}$ ]	1.29
Kinematic viscosity of oil $\kappa_l$ [ $\text{mm}^2 \text{s}^{-1}$ ]	32	Kinematic viscosity of vapor $\kappa_v$ [ $\text{mm}^2 \text{s}^{-1}$ ]	42.4
Material properties			
Young's modulus of shaft $E_1$ [GPa]	210	Young's modulus of bearing $E_2$ [GPa]	128
Poisson's ratio of shaft $\nu_1$	0.3	Poisson's ratio of bearing $\nu_2$	0.3
Arithmetical mean roughness on shaft surface $R_a^{shaft}$ [ $\mu\text{m}$ ]	0.25	Arithmetical mean roughness on bearing surface $R_a^{bearing}$ [ $\mu\text{m}$ ]	0.30
Root-mean-square roughness on shaft surface $R_q^{shaft}$ [ $\mu\text{m}$ ]	0.45	Root-mean-square roughness on bearing surface $R_q^{bearing}$ [ $\mu\text{m}$ ]	0.38
Boundary friction coefficient $\mu_{bound}$	0.2 [24, 146]	Elastic factor $K$	0.001 [28,147]

With these input parameters of the mixed-EHL model, the simulation procedure is shown in Figure 5.3. The governing equations of deformation, surface roughness as

well as the load balance-based shaft movement and mesh update are integrated with the N-S equations. Meanwhile, as a general approximation in N-S based CFD models of textured journal bearings, the shaft misalignment and bending are neglected in this work. Similar simplification can also be found in recent work in Refs. [68,74–76]. The whole procedure is introduced in the following.

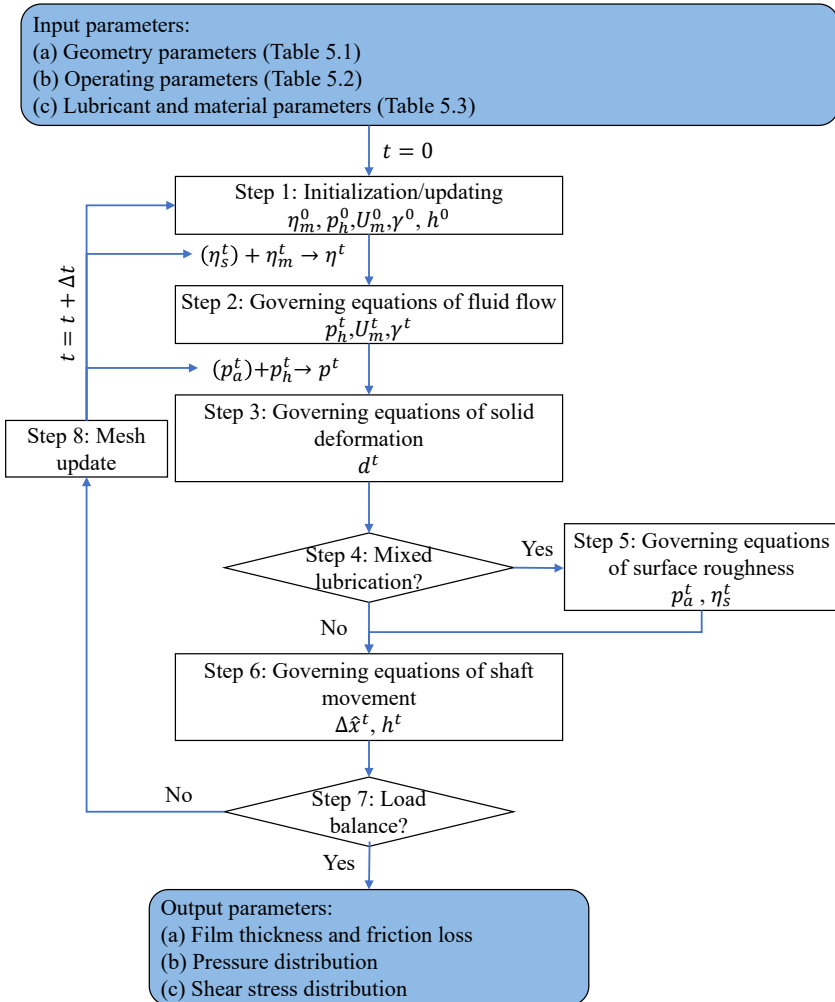


Figure 5.3 Simulation flowchart of the N-S based mixed-EHL model

**Step 1:** Initialization for the N-S based mixed-EHL model

At the beginning of the simulation ( $t = 0$ ), the fraction of the lubricating oil is initialized to be 1 ( $\gamma^0 = 0$ ), which indicates the bearing clearance is fully flooded with the lubricating oil. Therefore, the viscosity of the lubricant mixture ( $\eta_m^0$ ) is initialized to be the viscosity of the lubricating oil ( $\eta_l$ ).

Additionally, the initial film thickness is initialized to be the bearing clearance ( $C$ ). The hydrodynamic pressure is initialized to be the ambient pressure (0.1MPa), and the velocity filed is initialized to be 0.

**Step 2:** Calculation of fluid flow

The N-S equations together with the cavitation model are solved. The hydrodynamic pressure filed generated by the lubricating film ( $p_h^t$ ), the velocity file of the lubricant ( $U_m^t$ ) and the vapor fraction ( $\gamma^t$ ) can be predicted.

**Step 3:** Calculation of solid deformation

The generated hydrodynamic pressure ( $p_h^t$ ) is used by the equations of solid deformation, providing the deformation of the bearing and shaft surfaces ( $d^t$ ).

**Step 4:** Determination of the lubrication regime

The dimensionless film thickness ( $H_s$ ) is calculated on each node using Eq. (5-10). When the minimum value of the dimensionless film thickness ( $H_s$ ) is less than 4, the journal bearing operates under mixed lubrication conditions.

**Step 5:** Calculation of the effect of surface roughness

In the case of operation under mixed lubrication conditions, the effect of surface roughness should be considered. The effects of surface roughness on the contact pressure and fluid viscosity are calculated, namely the asperity contact pressure ( $p_a^t$ ) and the roughness-viscosity ( $\eta_s^t$ ). In the subsequent time step, both parameters are utilized. The roughness-viscosity ( $\eta_s^t$ ) is applied in Step 2 to calculate fluid flow. The asperity contact pressure ( $p_a^t$ ) is used in Step 3 to calculate solid deformation.

**Step 6:** Calculation of shaft movement

With the calculated hydrodynamic pressure ( $p_h^t$ ) and the calculated asperity contact pressure ( $p_a^t$ ), the shaft movement within a specified time step can be determined.

**Step 7:** Determination of load balance

After the shaft movement, the load balance condition will be checked. When  $F_{error} = |F^t - L_{ext}|/L_{ext} < 10^{-3}$ , the simulation will be stopped.

### Step 8: Mesh update

With the shaft movement and the elastic deformation of the solid materials, the fluid domain will change. Consequently, the mesh in the fluid domain needs to be updated during the simulation. To update the mesh accordingly, a dynamic mesh algorithm is proposed in this work.

- First of all, to increase the simulation efficiency, the mesh updating domain is determined. In this work, the entire mesh domain is divided into two sub-domains: the oil film gap domain and the texture domain, see Eq. (5-16):

$$\begin{cases} n_j \leq n_{total} & \text{oil film gap domain} \\ n_j > n_{total} & \text{texture domain} \end{cases} \quad (5-16)$$

where  $n_j$  is the radial reticulate layer for each mesh node  $j$ ;  $n_{total}$  is the total number of radial reticulate layers in the oil film gap domain ( $n_{total}=6$  in Figure 5.4).

The oil film gap domain refers to the area between the two blue lines in Figure 5.4(a). The shaft is moving and deforming during simulation. Therefore, the mesh nodes within the oil film gap domain should be updated. In contrast, the nodes within the texture domain are not updated, because the textured bearing is considered to be stationary in the present work.

- Secondly, the displacement of each mesh node on the shaft surface ( $\Delta\hat{x}, \Delta\hat{y}$ ) can be calculated as:

$$\begin{cases} \Delta\hat{x}^t(\theta', z') = d_x^t(\theta', z') + \Delta x^t(\theta', z') \\ \Delta\hat{y}^t(\theta', z') = d_y^t(\theta', z') + \Delta y^t(\theta', z') \end{cases} \quad (5-17)$$

- Eventually, the coordinates ( $\hat{x}_j^t, \hat{y}_j^t$ ) of each node  $j$  within the oil film gap domain at the time step  $t$  are calculated based on their radial reticulate layer  $n_j$  using Eq. (5-18):

$$\begin{cases} \hat{x}_j^t = \hat{x}_j^{t-\Delta t} + \left(1 - \frac{n_j}{n_{total}}\right) \Delta\hat{x}^t \\ \hat{y}_j^t = \hat{y}_j^{t-\Delta t} + \left(1 - \frac{n_j}{n_{total}}\right) \Delta\hat{y}^t \end{cases} \quad (5-18)$$

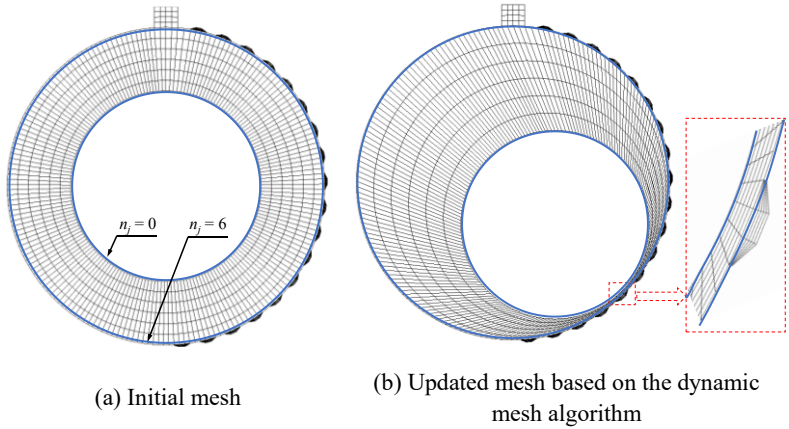


Figure 5.4 Mesh distribution of a textured journal bearing with an exaggerated clearance ( $n_{total} = 6$ ).

To clearly show the capability of this dynamic mesh algorithm, Figure 5.4 illustrates the mesh distribution of a textured journal bearing with an exaggerated clearance. As shown in Figure 5.4 (a), the above-mentioned dynamic mesh algorithm is based on the structured mesh distribution. It can be observed from Figure 5.4 (b) that, the updated mesh can keep a structured distribution even at a large eccentricity ratio. The comparison of mesh parameters is exemplarily listed in Table 5.4. After the mesh update, the number of mesh cells and points remain the same as in the initial mesh. Additionally, skewness and aspect ratio, which are commonly employed to quantify the mesh quality [148], are compared in Table 5.4. High values of skewness or aspect ratio may impair the accuracy of results and reduce the convergence speed. The thresholds for skewness and aspect ratio in OpenFOAM are 4 and 1000, respectively [148]. Consequently, as indicated in Table 5.4, the dynamic mesh algorithm in the present work can maintain a satisfactory mesh quality during the simulation.

Table 5.4 Comparison of mesh parameters for the initial and updated meshes

Item	Cells	Points	Average skewness	Average aspect ratio
Initial mesh	649,984	787,119	0.015	22.80
Updated mesh	649,984	787,119	0.021	32.00

After all the above steps, the simulation at time step  $t$  is finished. With the updated mesh and fluid properties, the equations of fluid flow, solid deformation, surface roughness and shaft movement are going to be solved again for the next time step until the load balance converges.

At the end of the simulation, the load-carrying capacity of the textured journal bearing represented by the film thickness ( $h$ ) can be calculated as:

$$h =$$

$$\sqrt{\{\hat{x}(\theta', z') - x_{bearing}(\theta', z')\}^2 + \{\hat{y}(\theta', z') - y_{bearing}(\theta', z')\}^2} \quad (5-20)$$

where  $\hat{x}(\theta', z')$  and  $\hat{y}(\theta', z')$  are the coordinates of each mesh node on the shaft surface at  $(\theta', z')$ ;  $x_{bearing}(\theta', z')$  and  $y_{bearing}(\theta', z')$  are the coordinates of each mesh node on the bearing surface at  $(\theta', z')$ .

In addition to the film thickness, the friction loss of the bearing is contributed by the fluid shear stress and the asperity shear stress. Therefore, the friction loss of the journal bearing is calculated by:

$$f = f_h + f_a = \int \int_A \bar{\tau} dA + \int \int_A \tau_a dA \quad (5-21)$$

where  $f_h$  and  $f_a$  are the fluid friction and the asperity friction, which are integrated from the fluid and the asperity shear stress. The asperity shear stress  $\tau_a$  is calculated by:

$$\tau_a = \mu_{bound} p_a \quad (5-22)$$

where  $\mu_{bound}$  is the boundary friction coefficient.

## 5.2. Mesh independence study

The mesh quality and mesh density of the model are keys to ensuring the accuracy of numerical results. To determine the appropriate mesh quantity, a mesh independence study is carried out, and the results are shown in Figure 5.5. According to the results, when the mesh number increases to  $8.65 \times 10^5$ , the maximum pressure remains nearly constant. To better capture the microflow within the textures, a mesh number of  $1.28 \times 10^6$  is chosen.

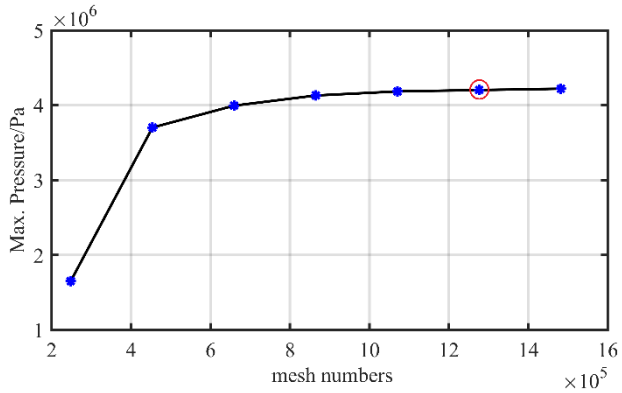


Figure 5.5 Mesh independence with the increasing mesh numbers

With this mesh number, the divisions across the film thickness and texture depth are both 6. The interval size used in the other directions is  $1.25 \times 10^{-4}$  m. The mesh model of the textured journal bearing is exemplarily shown in Figure 5.6.

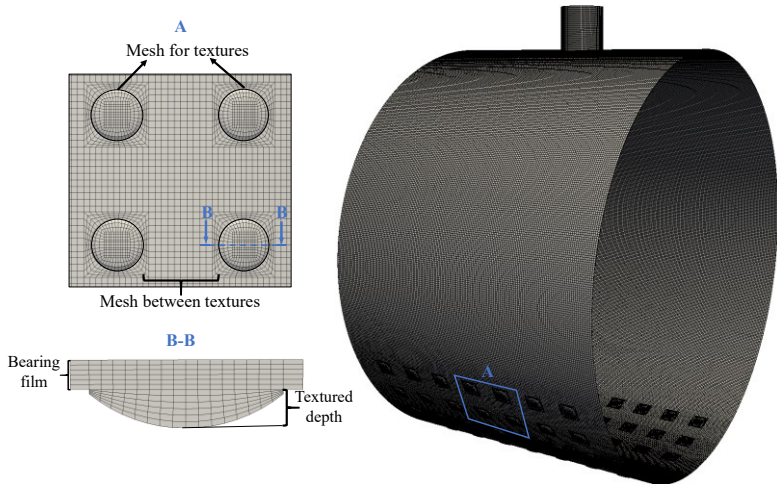


Figure 5.6 Mesh model for the textured journal bearing

### 5.3. Experimental validation

Prior to applying the N-S based mixed-EHL model to predict the LCC and FL of journal bearings, its validity should be verified by comparison with experimental results. In this work, the LCC and FL are two primary parameters. The LCC is validated using the minimum film thickness and pressure distribution. Subsequently, the FL is validated using the friction coefficient.

Additionally, the developed model is applicable to both non-textured and textured journal bearings as well as to both hydrodynamic and mixed lubrication conditions. Therefore, the experimental validation is conducted for both types of journal bearings and both lubrication conditions.

#### 5.3.1. Validation of minimum film thickness and pressure distribution

The first validation is conducted with the experimental results from Gdansk University of Technology (GTU). The test rig for the journal bearing is shown in Figure 5.7. The tested journal bearing is installed on the main shaft (1), guided by two self-aligning rolling bearings (9), and is mounted inside a rigid housing (2). The tested bearing is closed on both sides with covers with seals (3). The radial load is applied by the hydraulic cylinder (4) via a hydrostatic bearing (5).

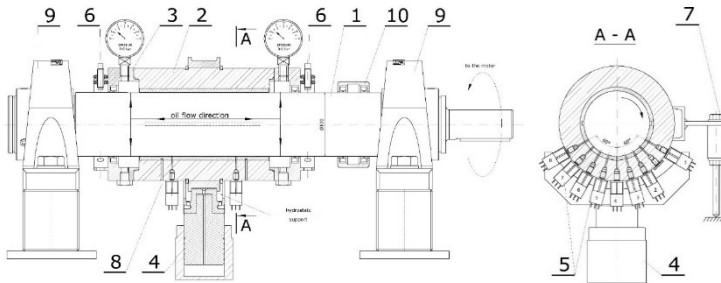


Figure 5.7 Test rig for the journal bearing from GTU [149]

On this test rig, the minimum film thickness is measured based on the shaft orbits under different rotational speeds. The shaft orbits on two sides of the tested bearing are captured by two pairs of proximity sensors (6). The detailed measurement method can be found in our paper [149].

In addition, the pressure distribution around the high-pressure region in the journal bearing is measured by 16 pressure gauges on both sides (Part 5 in Figure 5.7). There

are 8 pressure-gauge holes placed in two planes perpendicular to the shaft axis, 50mm from the bearing mid-plane.

To validate the minimum film thickness and pressure distribution, the simulations are conducted using the same lubrication and operating parameters applied in the experiments, as listed in Table 5.5. All the measurements are repeated for three times for each operating condition.

Table 5.5 Lubricant properties and operating parameters for this validation

Lubricant properties	
Kinematic viscosity [ $\text{mm}^2 \text{s}^{-1}$ ]	95.73
Density [ $\text{kg/m}^3$ ]	917.4
Operating parameters	
Bearing diameter [mm]	100.3
Bearing width [mm]	200
Relative clearance [%]	3.2
Oil inlet pressure [MPa]	0.2
Radial load [MPa]	0.6
Rotational speed [rpm]	10~660

First, a comparison of experimental and simulation results for the minimum film thickness is conducted. Figure 5.8 presents the comparison for the minimum film thickness at seven rotational speeds. The experimental and simulation results both show an increase in the minimum film thickness with increasing rotational speed, and therefore exhibit a similar trend. The maximum deviation between the experiment and the simulation is 11%, occurring at the rotational speed of 660rpm. This indicates good agreement between the experimental and simulation results in terms of the minimum film thickness.

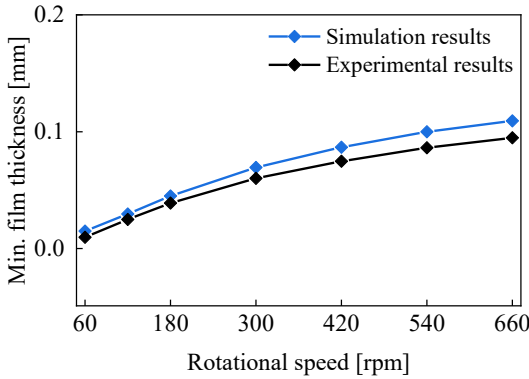
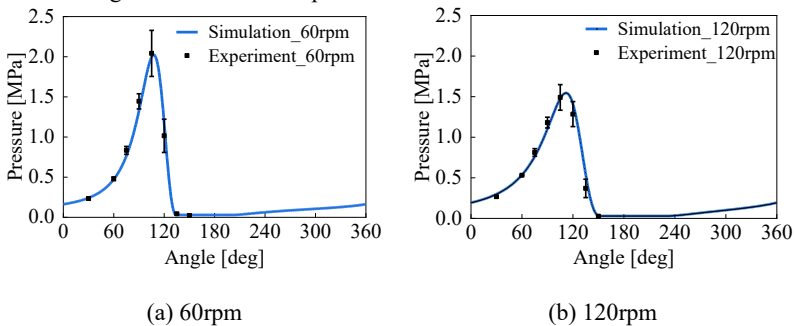


Figure 5.8 Experimental and simulation results for minimum film thickness

Additionally, a comparison for the hydrodynamic pressure at six rotational speeds is shown in Figure 5.9. The black error bars represent the standard deviation within three measurements. At various rotational speeds, the simulation results consistently exhibit a good agreement with the experimental results. Notably, at rotational speeds of 60 rpm, 120 rpm, and 180 rpm, the simulation results are in high agreement with the experimental results, with deviations below 0.05 MPa. At the higher rotational speed, the difference between the experimental and simulation results slightly increases. A possible reason for this can be that thermal effect induced by higher speeds. Nevertheless, the maximum error remains around 0.15 MPa, which still lays in an acceptable range. Therefore, the predicted pressure distributions exhibit reasonable agreement with the experimental results.



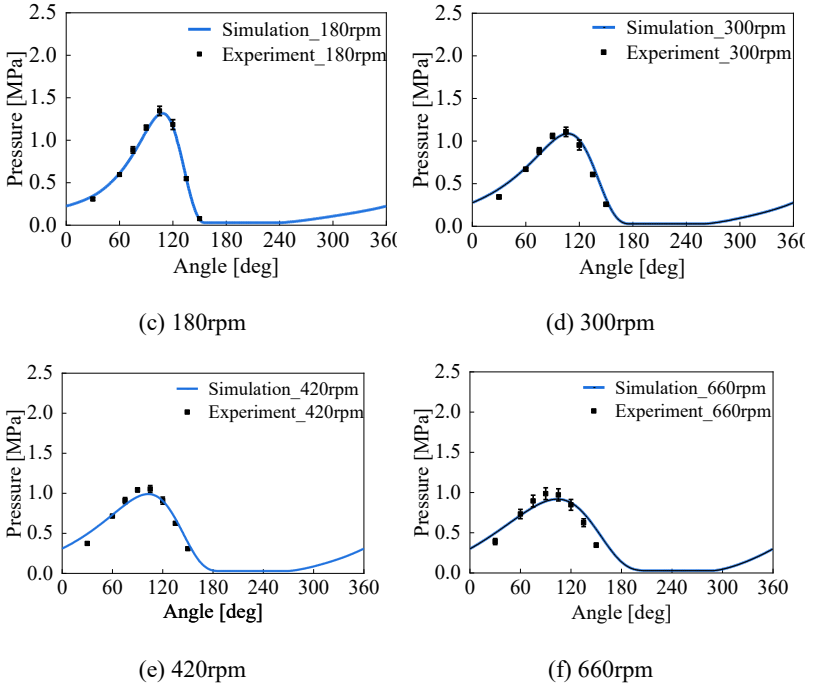


Figure 5.9 Comparison of experimental and simulation results for hydrodynamic pressure distribution

### 5.3.2. Validation of friction loss

In this section, the validation for the friction loss is carried out. The friction coefficient predicted by the N-S based mixed-EHL model are compared with experimental results from the available literature [19]. The used lubricant parameters and operating parameters has been detailed by Lu et al. [27]. Additionally, the boundary friction coefficient ( $\mu_{bound}$ ) is set as 0.17 [19] and the elastic factor  $K$  is also set to 0.001 [28,147] for the Greenwood and Tripp contact model.

The first validation is performed for the non-textured journal bearing. The comparison results are presented in Figure 5.10. As indicated by both simulation and experimental results, the friction coefficient first decreases rapidly and then slightly rises as the rotational speed increases. This indicates that within the compared speed range, the lubrication condition gradually transitions from the mixed lubrication to the

hydrodynamic lubrication. The simulation and experimental results show good agreement under both the hydrodynamic and mixed lubrication conditions.

Under the hydrodynamic lubrication, a constant difference in the friction coefficient of around 0.003 can be observed. However, considering the potential tolerances in the manufacturing, assembly, and measurement, it can be concluded that the simulation results remain within an acceptable range. Therefore, it is sufficient to demonstrate the feasibility and accuracy of the developed N-S based mixed-EHL model.

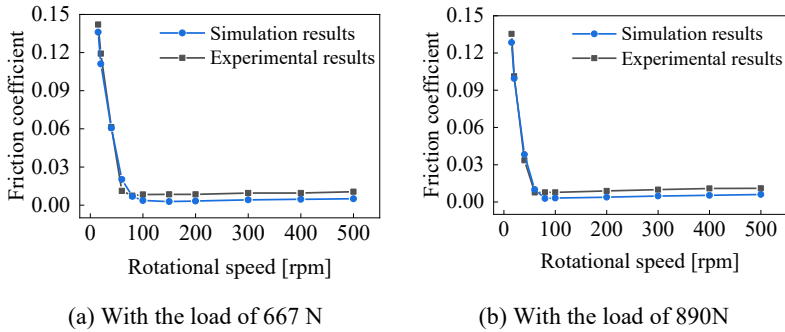


Figure 5.10 Validation of friction loss for the non-textured journal bearing

Under the same operating conditions, the friction coefficients of textured journal bearings are also validated. As shown in Figure 5.11, the simulation results also agree well with the experiments under both the hydrodynamic and mixed lubrication conditions.

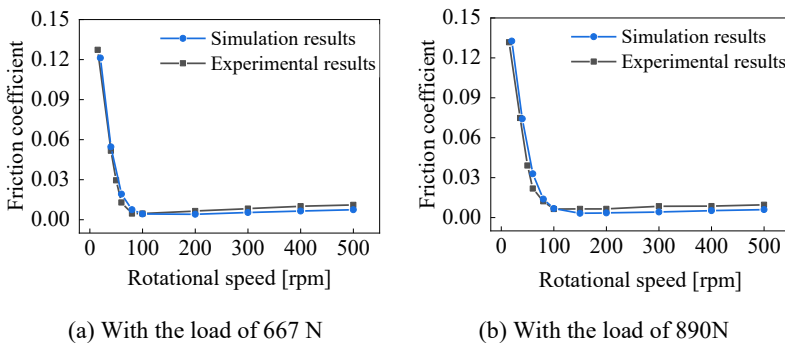


Figure 5.11 Validation of friction loss for the textured journal bearing

In summary, in order to validate the accuracy of the N-S based mixed-EHL model, the simulation results are compared with experimental results. The validation of the model is demonstrated from the good agreement between the simulation and experimental results in terms of minimum film thickness, hydrodynamic pressure and friction coefficient. Therefore, this numerical model can be used for the further study of textured journal bearings, which will be presented in the next chapter.



## 6. Influence of textures on the film thickness and friction loss of journal bearings

Based on the validated N-S based mixed-EHL model, the influence of textures on the LCC and FL of journal bearings can be studied. Notably, as introduced in Subchapter 5.1.5, the LCC can be quantitatively represented by the minimum film thickness when the external load is given. Therefore, in this chapter, the influence of textures on both the minimum film thickness and friction loss are compared and analyzed under both hydrodynamic and mixed lubrication conditions.

The studied texture parameters involve texture distribution and geometry parameters, including texture position, texture width ratio and texture depth ratio. Five texture positions are visualized in Figure 6.1, and their distribution parameters are detailed in Table 6.1. In addition, two levels are selected for both the texture width and depth ratios. A full-factorial simulation, as listed in Table 6.2, is conducted to decouple the influence of each texture parameter.

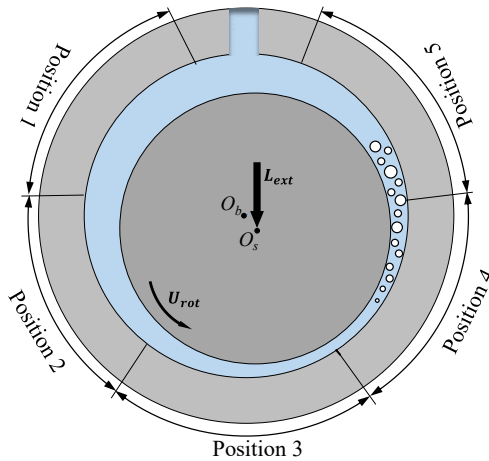


Figure 6.1 Positions of texture area

Table 6.1 Distribution parameters for five positions

Position	1	2	3	4	5
Starting angle $\alpha$ [°]	260	200	140	80	20
Coverage angle $cov$ [°]	72				

Table 6.2 Parameters of full-factorial simulation cases

Simulation case number	Texture position [-]	Texture width ratio $w_t/W$ [-]	Texture depth ratio $d_t/C$ [-]	Designation
1	Positions 1	0.4	0.5	W04D05
2			2.0	W04D20
3		0.8	0.5	W08D05
4			2.0	W08D20
5	Positions 2	0.4	0.5	Same as above
6			2.0	
7		0.8	0.5	
8			2.0	
9	Positions 3	0.4	0.5	Same as above
10			2.0	
11		0.8	0.5	
12			2.0	
13	Positions 4	0.4	0.5	Same as above
14			2.0	
15		0.8	0.5	
16			2.0	
17	Positions 5	0.4	0.5	Same as above
18			2.0	
19		0.8	0.5	
20			2.0	

### 6.1. Influence of textures under hydrodynamic lubrication

This subchapter studies the effect of textures on the minimum film thickness and friction loss of journal bearings under the hydrodynamic lubrication. The operating condition for the hydrodynamic lubrication in this work is set to a load of 500 N and a rotational speed of 1,000 rpm. This subchapter begins with a comparison of the minimum film thickness and friction loss of textured journal bearings with those of non-textured journal bearings. Subsequently, to investigate the underlying mechanisms for these effects, the pressure and shear stress distributions of textured journal bearings are analyzed.

### 6.1.1. Influence on the minimum film thickness and friction loss

#### (a) Influence on the minimum film thickness

The effect of textures on the minimum film thickness is shown in Figure 6.2. Compared with the non-textured bearing, the minimum film thickness of textured bearings can be reduced, especially when textures are distributed at Positions 3 and 4 in the present case. The reduced minimum film thickness indicates the decreased load-carrying capacity. For the smaller texture width ratio (W04D05 and W04D20), the differences between textured and non-textured bearings are all within 0.5  $\mu\text{m}$ . When the texture width ratio increases to 0.8 (W08D05 and W08D20), the effect of textures becomes more pronounced.

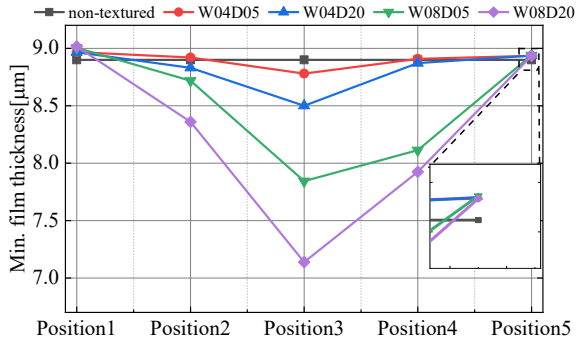


Figure 6.2 Minimum film thickness under different texture geometries and positions

#### (b) Influence on the friction loss

Figure 6.3 illustrates the friction loss under different texture geometries and positions. It can be observed that textured bearings show lower friction loss at all positions compared with the non-texture bearing in the present case. Especially when textures are distributed at Position 4, the reduction in the friction loss is more significant.

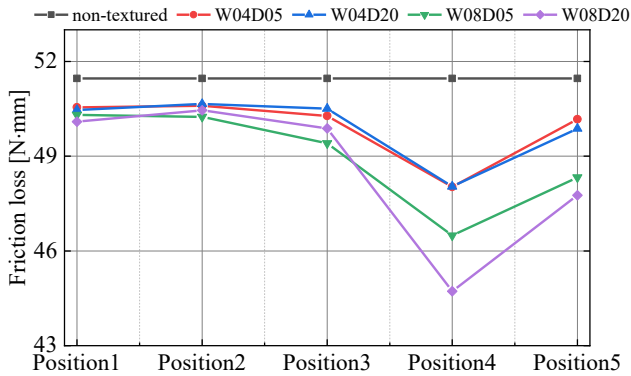


Figure 6.3 Friction loss under different texture geometries and positions

Based on the combined results from Figure 6.2 and Figure 6.3, when textures are distributed downstream of the high-pressure region of the journal bearing (Position 5), the friction loss can be reduced. Meanwhile, the minimum film thickness is slightly increased, indicating a higher load-carrying capacity. This observation is more pronounced for the texture configuration of W08D20, where friction loss is reduced by over 7.0% and the minimum film thickness increases by 0.3%.

In summary, the potential of applying textures to journal bearings is indicated by the above results. A proper design of texture geometry and distribution parameters can significantly reduce the friction loss and simultaneously increase the load-carrying capacity. To study the underlying reasons for these effects, the lubrication mechanism analysis is conducted in the following section.

### 6.1.2. Lubrication mechanism analysis

As introduced in Subchapter 5.1, when journal bearings operate under the hydrodynamic lubrication, the load-carrying capacity is obtained by integrating the hydrodynamic pressure over the shaft–bearing contact surface and the friction loss is contributed by the integration of the fluid shear stress. To analyze the lubrication mechanism of textured journal bearings, the hydrodynamic pressure and fluid shear stress distributions at various texture positions are discussed using the texture configuration of W08D05 as an example.

**(a) Position 1 and Position 2**

The textures at Positions 1 and 2 have a similar effect on both the minimum film thickness and the friction loss. Therefore, the lubrication mechanism for these two positions is discussed together.

The hydrodynamic pressure distributions at both positions are shown in Figure 6.4 and Figure 6.5. The pressure contours for both positions are shown in Figure 6.4 (a) and Figure 6.5 (a), respectively. To provide a more quantitative comparison of the hydrodynamic pressure between the textured and non-textured bearings, the pressure profiles along the bearing centerlines are additionally shown in Figure 6.4 (b) and Figure 6.5 (b) for both positions.

From the pressure contours, a high-pressure region can be observed, which is the main area to contribute the load-carrying capacity of the journal bearing [25]. Meanwhile, as observed in Figure 6.4 (b) and Figure 6.5 (b), the hydrodynamic pressure of the textured bearing is nearly identical to that of the non-textured bearing. This can be explained by the fact that the textures are positioned away from the high-pressure region for these two texture positions (see Figure 6.4 (a) and Figure 6.5 (a)). Consequently, the minimum film thickness for these two positions is relatively similar to that of the non-textured bearing (see Figure 6.2).

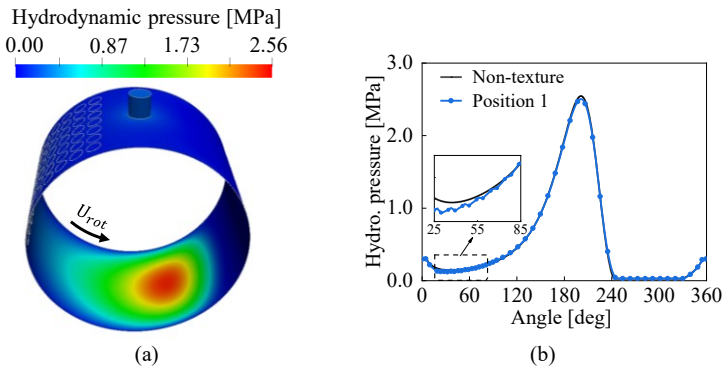


Figure 6.4 Hydrodynamic pressure distributions at Position 1 (a) Pressure contour (b) Pressure profiles

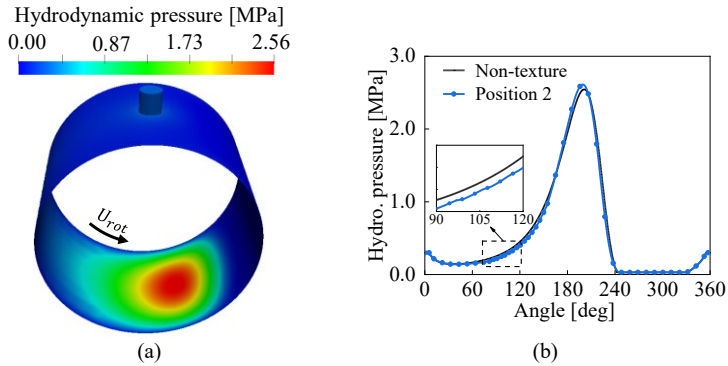


Figure 6.5 Hydrodynamic pressure distributions at Position 2 (a) Pressure contour (b) Pressure profiles

The presentation of fluid shear stress follows a similar pattern to the pressure distribution. The fluid shear stress contours and the shear stress profiles along the bearing centerlines are illustrated in Figure 6.6 and Figure 6.7. It can be observed from Figure 6.6(a) and Figure 6.7(a) that, the high shear stress region occurs at the minimum oil film area. This is the main region which contributes to the friction loss from the journal bearing [25]. In addition, the fluid shear stress at textures is significantly reduced. As shown in Figure 6.6(b) and Figure 6.7(b), the fluid shear stress can be reduced to nearly zero at textures. This significant reduction can be explained by the local increase in the oil film thickness at textures. Consequently, although the textures at these two positions are far from the high shear stress region, the friction loss can still be slightly reduced (see Figure 6.3).

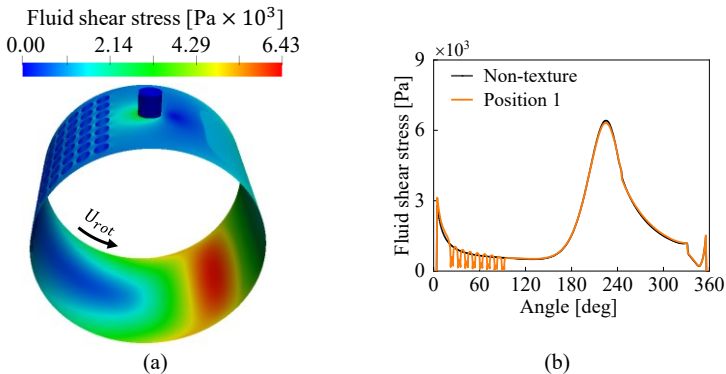


Figure 6.6 Fluid shear stress distributions at Position 1 (a) Shear stress contour (b) Shear stress profiles

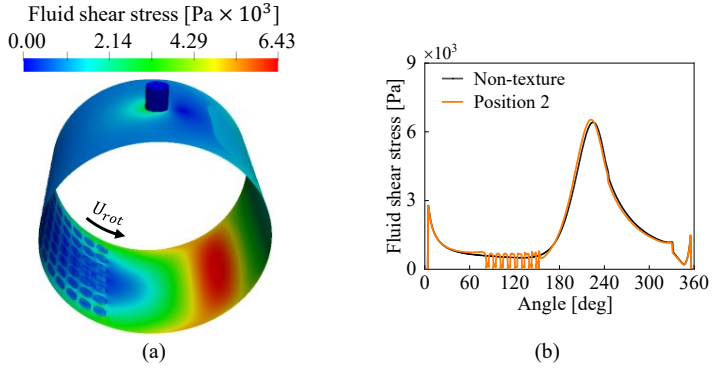


Figure 6.7 Fluid shear stress distributions at Position 2 (a) Shear stress contour (b) Shear stress profiles

**(b) Position 3 and Position 4**

This section analyzes the lubrication mechanism for Positions 3 and 4. The hydrodynamic pressure distributions at both positions are presented in Figure 6.8 and Figure 6.9, respectively. As shown in Figure 6.8(a) and Figure 6.9(a), the textures are distributed in the high-pressure region at these two positions. Consequently, the continuity of the high-pressure region is disrupted and thus the corresponding load-carrying capacity is decreased. This disruption can be explained by the interference of the sudden increase in the film thickness at textures to the original convergence effect of the journal bearing. This conclusion is in agreement with previously published work by Lin et al. [75].

Meanwhile, from the comparison of pressure profiles in Figure 6.8(b) and Figure 6.9(b), it can be observed that when the lubricant flows through a texture, a local pressure fluctuation occurs. The local pressure at the texture inlet decreases due to the increased flow area. Subsequently, the reduced flow area at the texture outlet leads to an increase in the hydrodynamic pressure. This local pressure fluctuation at the texture is referred to as micro-hydrodynamic pressure [11]. From the closer inspection of the local pressure distribution in Figure 6.8(b) and Figure 6.9(b), the local pressure reduction effect is less pronounced than the local pressure increase effect. This can be deduced from the larger yellow area compared to the green area. Hence, a positive hydrodynamic pressure can be generated at the texture, which further contributes to improve the load-carrying capacity of journal bearings. The beneficial effect of the micro-hydrodynamic pressure is also reported in Refs. [11,16,57,150].

Therefore, the effect of textures on the minimum film thickness includes a beneficial effect from the micro-hydrodynamic pressure and a negative effect from the interference with the high-pressure region. At these two positions, the beneficial effect of the micro-hydrodynamic pressure is outweighed by the negative impact of the disruption on the high-pressure region, since the minimum oil film thicknesses are significantly reduced at Positions 3 and 4 (see Figure 6.2).

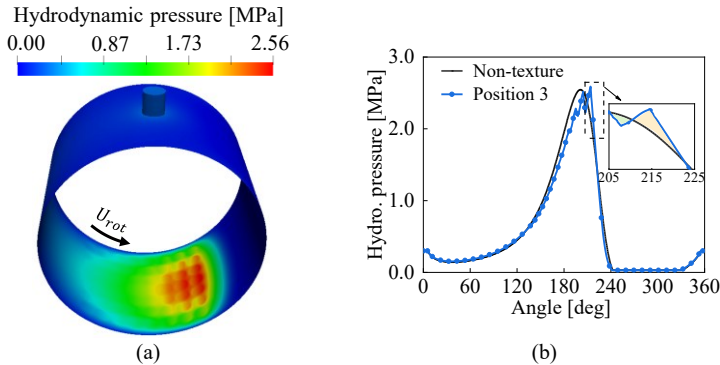


Figure 6.8 Hydrodynamic pressure distributions at Position 3 (a) Pressure contour (b) Pressure profiles

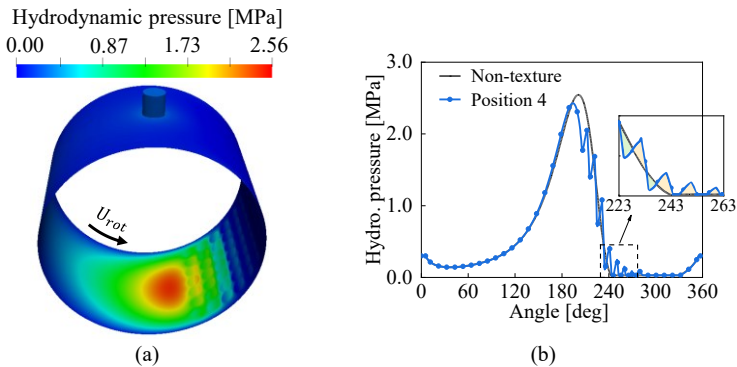


Figure 6.9 Hydrodynamic pressure distributions at Position 4 (a) Pressure contour (b) Pressure profiles

The effects of textures on the fluid shear stress at Positions 3 and 4 are shown in Figure 6.10 and Figure 6.11. The variation in the fluid shear stress is highly dependent on the film thickness. On the one hand, the reduction in the minimum film thickness of the textured bearing results in an increase in the maximum fluid shear stress. The increased fluid shear stress in the textured bearing can be observed from Figure 6.10

(b) and Figure 6.11 (b). As the friction is the integral of the fluid shear stress, this increase can lead to an increase in friction loss. On the other hand, the local increase in the film thickness at textures leads to a significant reduction in the fluid shear stress. With these two texture distributions, the textured areas are covering the high fluid shear stress region. Therefore, the reduction in the fluid shear stress significantly reduces the friction loss [3,16]. In conclusion, the impact of textures on the friction loss of the journal bearing depends on the trade-off between these two aspects. At these two positions, although the fluid shear stresses increase locally, the overall friction losses are significantly reduced by textures (see Figure 6.3).

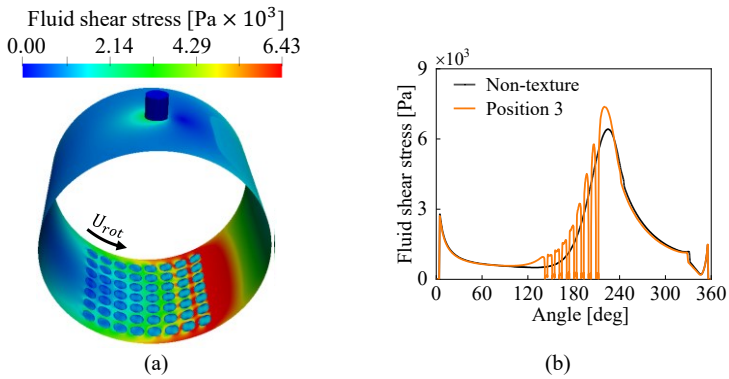


Figure 6.10 Fluid shear stress distributions at Position 3 (a) Shear stress contour (b) Shear stress profiles

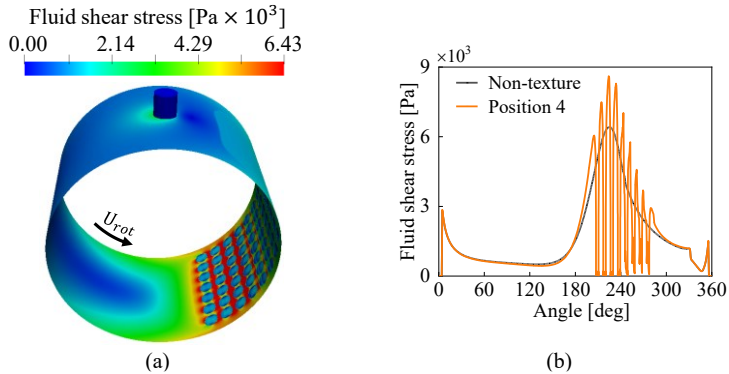


Figure 6.11 Fluid shear stress distributions at Position 4 (a) Shear stress contour (b) Shear stress profiles

**(c) Position 5**

The hydrodynamic pressure distribution at Position 5 is shown in Figure 6.12. As discussed above, the effect of textures on the minimum film thickness of journal bearings includes a beneficial effect generated from the micro-hydrodynamic pressure and a negative effect caused by interference with the high-pressure region.

As shown in Figure 6.12(a), the textured area is positioned downstream of the high-pressure region and thus is not interfering with the main bearing land. Figure 6.12(b) shows that the textured area is located within the cavitation region. The cavitation region is identified by the constant pressure region following the high-pressure region, as the pressure-drop is limited by the saturation pressure [61]. Within the cavitation region, the pressure in the non-textured bearing remains at the saturation pressure. In contrast, the textured bearing generates an additional micro-hydrodynamic pressure, as can be observed from the local enlarged view in Figure 6.12 (b). This demonstrates the cavitation effect of textures introduced in Subchapter 3.2.2. Consequently, the beneficial effect on the hydrodynamic pressure is dominating at this position, leading to a slightly higher minimum film thickness than that of the non-textured bearing (see Figure 6.2).

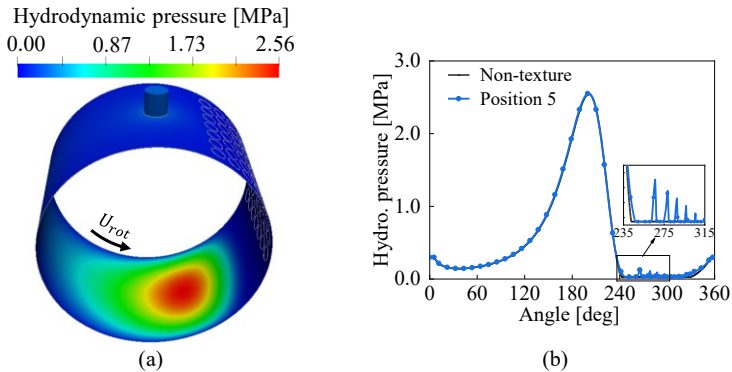


Figure 6.12 Hydrodynamic pressure distribution at Position 5 (a) Pressure contour (b) Pressure profiles

As concluded above, the impact of textures on the friction loss of the journal bearing depends on the trade-off between the increased maximum fluid shear stress caused by the decreased film thickness and the reduced fluid shear stress due to the local increase in film thickness at textures. The fluid shear stress distribution at Position 5 is illustrated in Figure 6.13. Notably, the fluid shear stress in the textured area is significantly reduced to nearly zero, without increasing the maximum shear stress. Consequently, the friction loss at this position is considerably reduced (see Figure 6.3).

Combined with the hydrodynamic pressure distribution for this position, it can be found that placing textures downstream of the high-pressure region effectively reduces friction loss, while the minimum film thickness does not decrease but instead slightly increases.

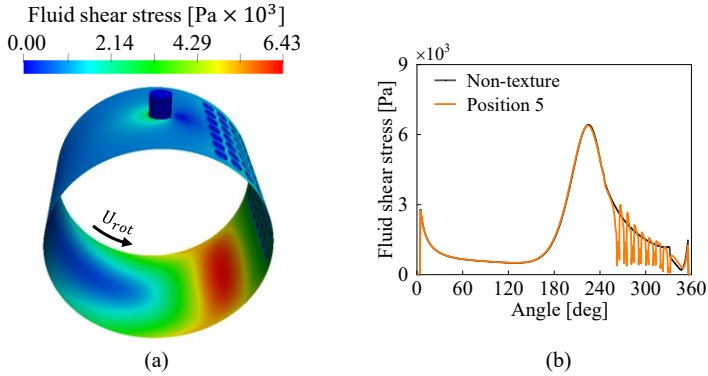


Figure 6.13 Fluid shear stress distributions at Position 5 (a) Shear stress contour (b) Shear stress profiles

In summary, textures can generate both negative and positive effects on the load-carrying capacity and the minimum film thickness, as Figure 6.14 shows. On the one hand, textures can induce a micro-hydrodynamic pressure, which contributes to the enhancement of the load-carrying capacity. On the other hand, textures can generate an interference effect on the high-pressure region. This leads to a lower load-carrying capacity and thus a lower minimum film thickness. Depending on the balance between these positive and negative effects, the load-carrying capacity of the journal bearing can be either enhanced or reduced. In the current work, the negative effect dominates, as the significant reduction in minimum film thickness is observed while its increase is slight.

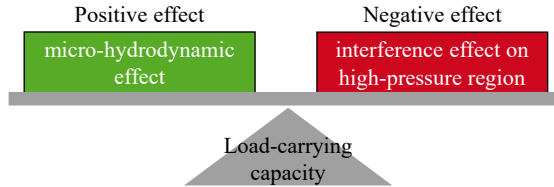


Figure 6.14 Effects of textures on the load-carrying capacity under HL condition

The effects of textures on the friction loss also depend on the balance between these positive and negative effects, as shown in Figure 6.15. Textures can reduce the local fluid shear stress due to the locally increased film thickness. In contrast, the maximum shear stress may increase due to the reduction in the minimum film thickness. In this work, the positive effect is dominant, particularly when textures are located in the region of minimum film thickness. Overall, placing textures downstream of the high-pressure region reduces the friction loss, while the minimum film thickness rises slightly.

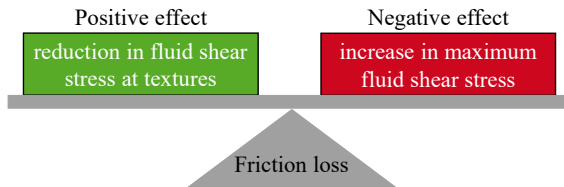


Figure 6.15 Effects of textures on the friction loss under HL condition

## 6.2. Influence of textures under mixed lubrication

This subchapter studies the influence of textures on the minimum film thickness and friction loss of journal bearings under the mixed lubrication condition. The operating condition for the mixed lubrication is set to a load of 500N and a rotational speed of 80rpm. First, the minimum film thickness and friction loss of textured journal bearings are compared with those of the non-textured journal bearing. Subsequently, the lubrication mechanisms of textured journal bearings are clarified by analyzing the pressure and shear stress distributions at five texture positions.

### 6.2.1. Influence on the minimum film thickness and friction loss

#### (a) Influence on the minimum film thickness

The effect of textures on the minimum film thickness under the mixed lubrication is examined in this section. Figure 6.16 illustrates the minimum film thickness for various combinations of texture geometry and position. From Position 1 to Position 5, the minimum film thickness initially decreases and then gradually increases. Similar to the findings under the hydrodynamic condition (see Figure 6.2), the differences between textured and non-textured bearings remain slight for the smaller texture width ratio (W04D05 and W04D20). When the width ratio increases to 0.8 (W08D05 and W08D20), the effect of textures becomes more pronounced.

It is worth highlighting the effect of textures at Position 4 on the minimum film thickness under both hydrodynamic and mixed lubrication conditions. The textures at Position 4 slightly increase the minimum film thickness under this mixed lubrication, whereas they have a detrimental effect under the hydrodynamic lubrication (see Figure 6.2). This means that the same texture configuration can yield different or even opposite effects under different operating conditions. This finding demonstrates that the texture design is highly dependent on operating conditions, which is also reported in Refs.[11,21,63].

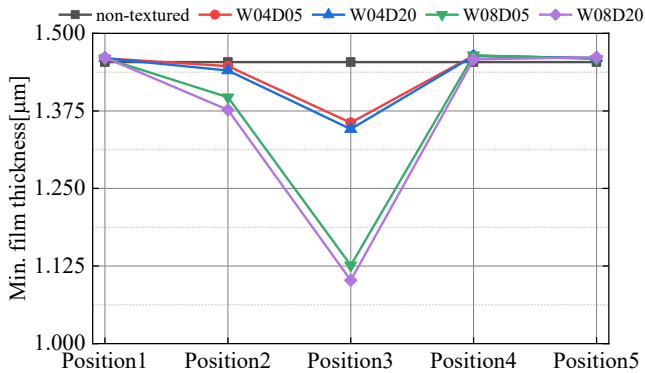


Figure 6.16 Minimum film thickness under different texture geometries and positions under mixed lubrication

**(b) Influence on the friction loss**

The effect of textures on the friction loss under the mixed lubrication condition is presented in Figure 6.17. It can be observed that textures may significantly increase the friction loss under this operating condition. Especially when textures are distributed at Position 3, the friction loss of the textured bearing can be over five times higher compared to that of the non-textured bearing.

The effect of textures on the friction loss under the mixed lubrication condition is highly different from their effect under the hydrodynamic lubrication condition. As shown in Figure 6.3 in Subchapter 6.1.1, under the hydrodynamic lubrication condition, textures can significantly reduce the friction loss at all positions. This contrast indicates that under the mixed lubrication condition, the friction loss of textured journal bearings is more sensitive to texture design parameters. Furthermore, this further highlights the necessity of optimizing texture parameters for journal bearings operating under the mixed lubrication condition.

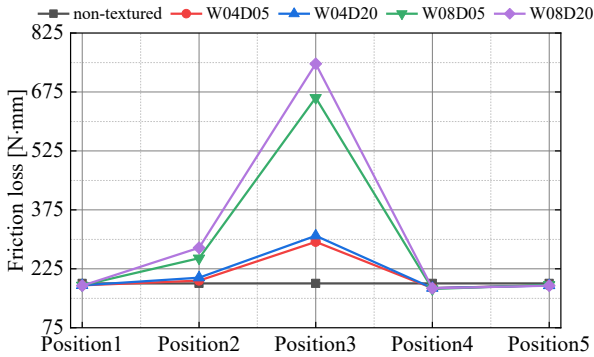


Figure 6.17 Total friction loss under different texture geometries and positions

As previously mentioned in Subchapter 5.1, the friction loss under the mixed lubrication condition arises from two sources: the fluid friction due to the fluid shear stress, and the asperity contact friction due to asperity contact. To study the underlying reasons for the significant effect on the total friction, the influences of textures on the fluid friction and asperity contact friction are presented below, respectively.

The effect of textures on the fluid friction is first shown in Figure 6.18. It can be observed that textures can still lead to a considerable reduction in the fluid friction at positions 3 and 4. Under the mixed lubrication condition in this work, the rotational speed of the shaft is only 80 rpm, which is quite low. This leads to a relatively small proportion of fluid friction in the total friction loss of textured journal bearings. Consequently, the reduction in the fluid friction is not comparable to the total friction loss.

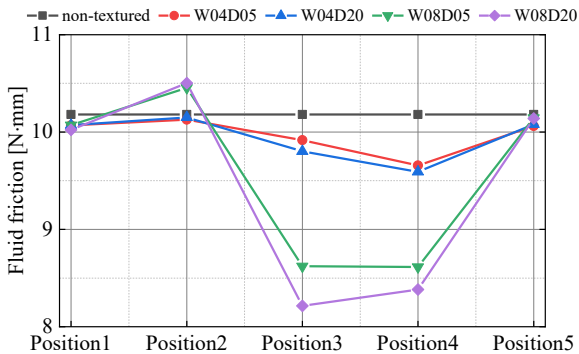


Figure 6.18 Fluid friction loss under different texture geometries and positions

The effect of textures on the friction loss induced by the asperity contact is illustrated in Figure 6.19. The asperity contact friction is significantly higher than the fluid friction. Therefore, under the mixed lubrication condition in this work, the total friction loss is primarily induced by the asperity contact friction. In addition, a significant increase in the asperity contact friction is observed at Position 3, resulting in a pronounced increase in total friction loss (see Figure 6.17).

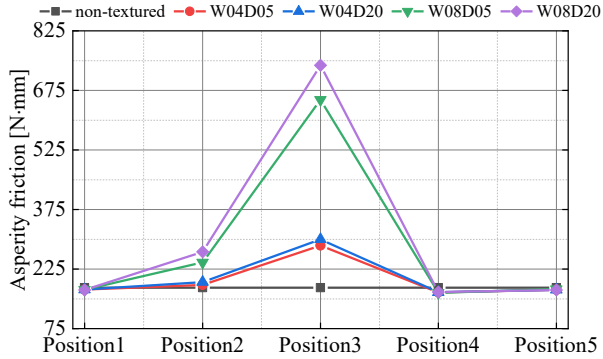


Figure 6.19 Asperity friction loss under different texture geometries and positions

## 6.2.2. Lubrication mechanism analysis

As introduced in Subchapter 5.1, when journal bearings operate under the mixed lubrication condition, the hydrodynamic pressure and asperity contact pressure are superimposed to carry the external load acting on the shaft. In addition, the friction loss arises from the integration of the fluid and asperity shear stresses. To analyze the effect of textures on the minimum film thickness and friction loss of journal bearings under the mixed lubrication condition, all the above pressure and shear stress distributions are discussed using the texture configuration of W08D05 as an example.

### (a) Position 1

The hydrodynamic and asperity contact pressure distributions for Position 1 are illustrated in Figure 6.20. Similar to the presentation under the hydrodynamic lubrication, both pressure contours and pressure profiles are shown together to provide a more quantitative comparison.

From the hydrodynamic pressure contour in Figure 6.20 (a), a notable high-pressure region can also be identified. Compared to the pressure distribution under the hydrodynamic lubrication in Figure 6.4, an increase in the maximum pressure is

observed. Additionally, the high-pressure region under the mixed lubrication condition is more concentrated.

The asperity contact pressure contour is shown in Figure 6.20 (c). Since the asperity contact pressure is directly influenced by the film thickness, the high contact pressure region is located around the minimum film thickness area. Due to the deformation caused by the high pressure at the axial center of the bearing, the maximum contact pressure occurs at both axial ends of the bearing.

In addition, as observed from pressure profiles in Figure 6.20 (b) and (d), both hydrodynamic and asperity pressures of the textured bearing are nearly identical to those of the non-textured bearing. This can be explained that the textured area is positioned away from both the high-pressure and the asperity contact regions (see Figure 6.20 (a) and (c)). Consequently, the minimum film thickness at this position is relatively similar to that of the non-textured bearing (see Figure 6.16). This conclusion is consistent with the findings under the hydrodynamic lubrication.

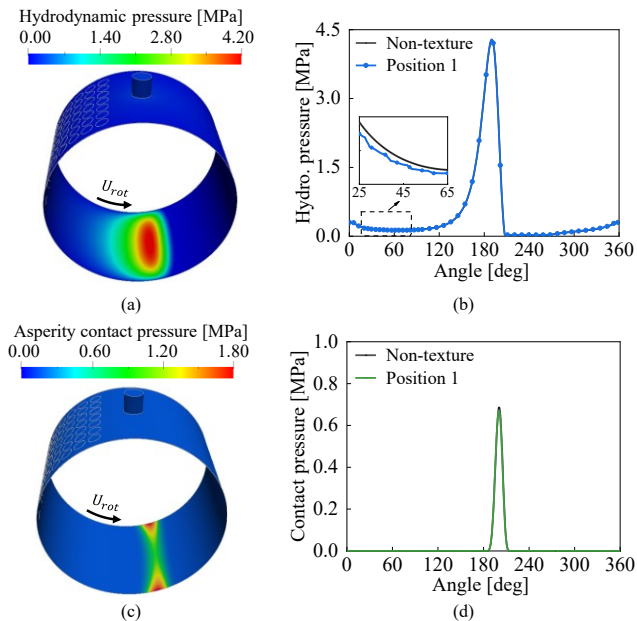


Figure 6.20 Pressure distributions at Position 1 (a) Hydrodynamic pressure contour (b) Hydrodynamic pressure profiles (c) Asperity pressure contour (d) Asperity pressure profiles

Turning the attention to the friction loss, the presentation of the shear stress follows a similar pattern of pressure distributions. The contours of the fluid and asperity shear stresses are shown in Figure 6.21 (a) and (c), while the corresponding shear stress profiles along the bearing centerlines are shown in Figure 6.21 (b) and (d). From the fluid shear stress distributions, the reduction in the fluid shear stress at textures can still be observed (see Figure 6.21 (a) and (b)). In addition, as shown in Figure 6.21 (c) and (d), the textured area at this position is away from the asperity contact region. Therefore, the asperity shear stress of the textured bearing is nearly identical with that of the non-textured bearing.

In addition, from the comparison of fluid and asperity shear stress distributions, it is evident that the asperity shear stress highly exceeds the fluid shear stress. The reason can be attributed to the low rotational speed, which results in relatively small fluid shear stress between the two surfaces. Consequently, the total friction loss under this operating condition is dominated by the asperity shear stress. The nearly identical asperity shear stress with the non-textured bearings leads to a similar total friction loss, as shown in Figure 6.17.

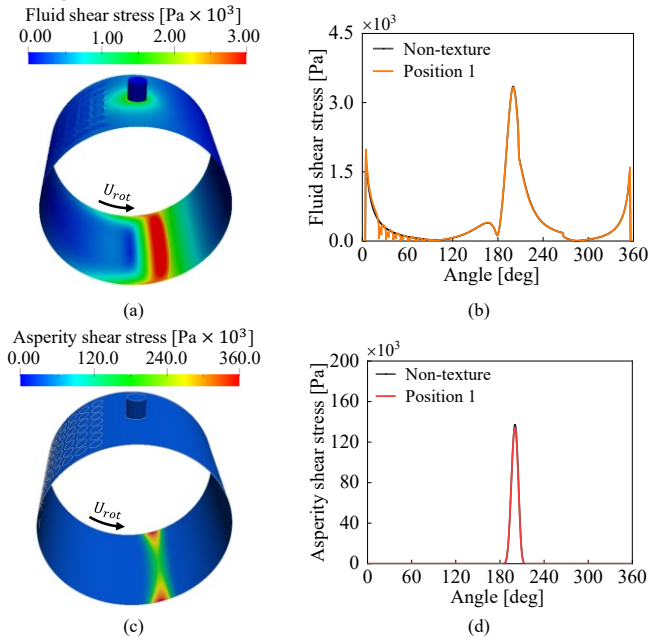


Figure 6.21 Shear stress distributions at Position 1 (a) Fluid shear stress contour (b): Fluid shear stress profiles (c) Asperity shear stress contour (d): Asperity shear stress profiles

**(b) Position 2**

The hydrodynamic and asperity contact pressure distributions for Position 2 are illustrated in Figure 6.22. As observed from the hydrodynamic pressure distribution in Figure 6.22 (a) and (b), the textured area at Position 2 starts to cover the high-pressure region. Due to the interference effect, the load-carrying capacity begins to decrease. Consequently, the minimum film thickness is slightly reduced (See Figure 6.16). The reduced minimum film thickness further increases the asperity contact pressure, as shown in Figure 6.22 (c) and (d).

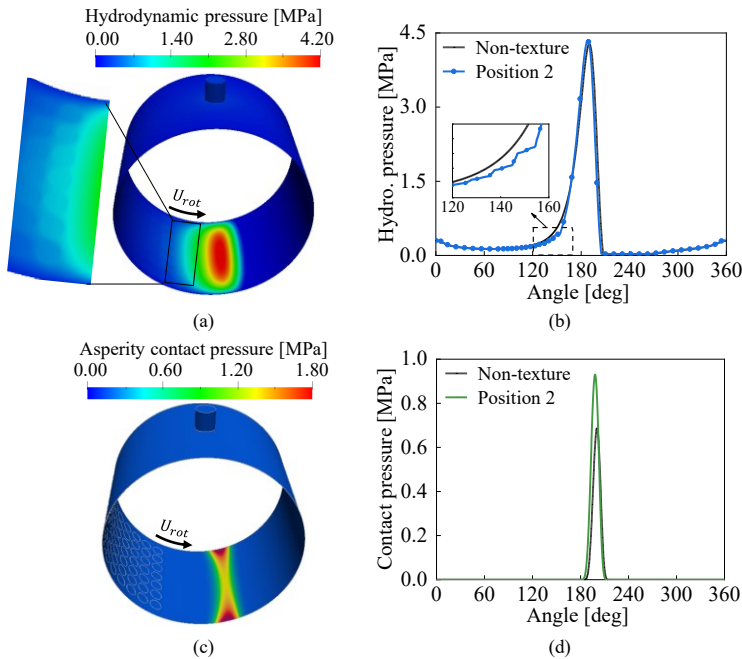


Figure 6.22 Pressure distributions at Position 2 (a) Hydrodynamic pressure contour (b) Hydrodynamic pressure profiles (c) Asperity pressure contour (d) Asperity pressure profiles

Figure 6.23 presents the shear stress distributions for Position 2. A slight reduction in the fluid shear stress at textures can also be observed in Figure 6.23 (a) and (b). In contrast, as shown in Figure 6.23 (c) and (d), the aforementioned reduced minimum film thickness leads to an increase in the asperity shear stress compared with the non-textured bearing. By comparing Figure 6.23 (b) and (d), it can be observed that the increase in asperity friction loss exceeds the slight reduction in fluid friction loss at

textures. Consequently, the total friction increases at this position, as illustrated in Figure 6.17.

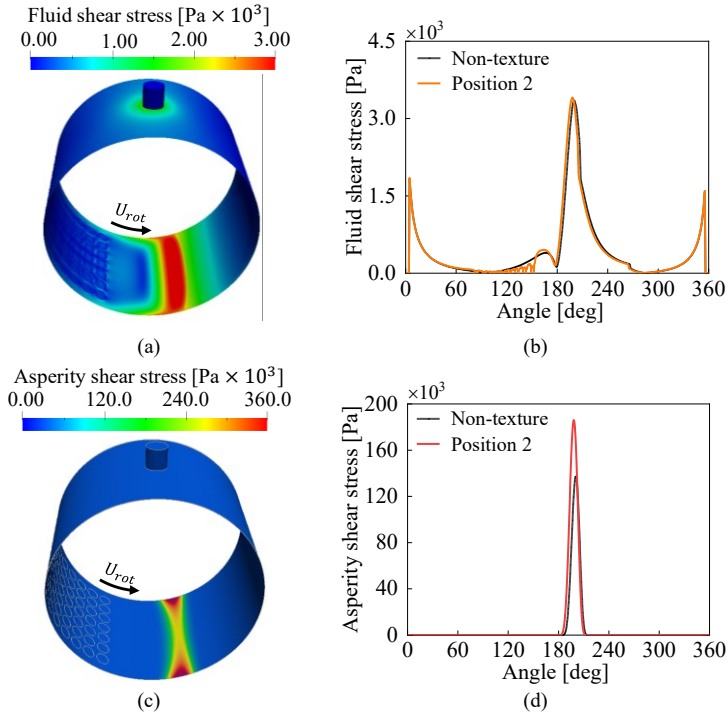


Figure 6.23 Shear stress distributions at Position 2 (a) Fluid shear stress contour (b) Fluid shear stress profiles (c) Asperity shear stress contour (d) Asperity shear stress profiles

### (c) Position 3

Figure 6.24 illustrates the hydrodynamic and asperity contact pressure distributions for Position 3. Figure 6.24 (a) and (b) show that, the continuity of the high-pressure region is completely disrupted by the textured area at this position. This interference with the overall hydrodynamic pressure distribution decreases the proportion of load supported by hydrodynamic pressure. The reduced load support from the hydrodynamic pressure further leads to a significant reduction in the minimum film thickness (see Figure 6.16).

In addition, Figure 6.24 (c) indicates that the asperity contact at textures can be avoided due to the local increase in the film thickness. However, the significant reduction in minimum film thickness intensifies the overall asperity contact. This is reflected by the expansion of the contact area in the circumferential direction and the increase in the maximum asperity contact pressure. As can be seen from Figure 6.24 (d), although the asperity contact pressure at textures is reduced to 0, the textured bearing's maximum asperity contact pressure is nearly five times higher than that of the non-textured bearing.

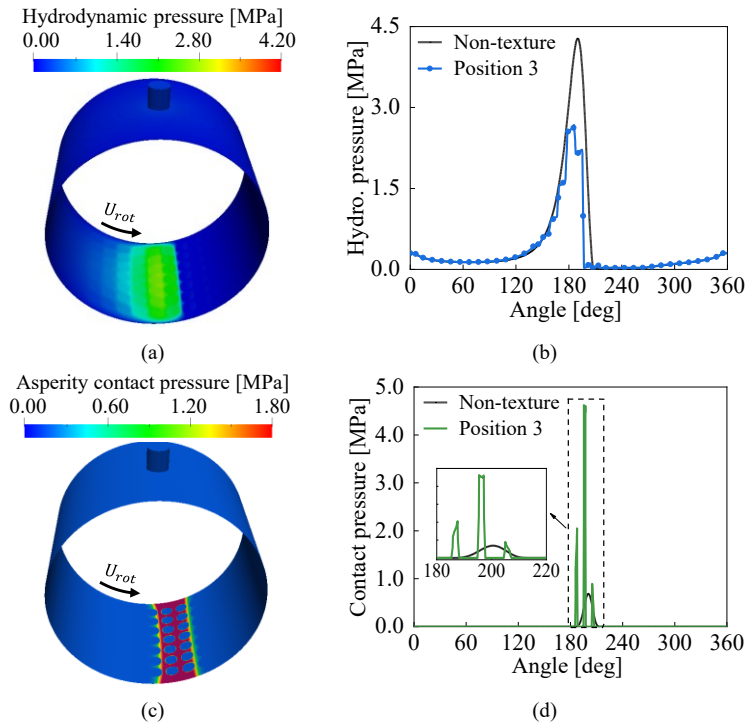


Figure 6.24 Pressure distributions at Position 3 (a) Hydrodynamic pressure contour (b) Hydrodynamic pressure profiles (c) Asperity pressure contour (d) Asperity pressure profiles

Figure 6.25 depicts the shear stress distribution at Position 3. The significant reduction in fluid shear stress at the textures can be observed from Figure 6.25 (a) and (b). Consequently, the fluid friction for Position 3 can be effectively reduced, as shown in Figure 6.18.

The asperity shear stress distributions are shown in Figure 6.25 (c) and (d). On the one hand, the asperity shear stress at textures is reduced to 0, indicating a decreased contact area at textures. On the other hand, the reduction in the film thickness leads to a significant increase in asperity shear stress within the contact region. The enlarged view in Figure 6.25 (d) reveals that, the increase in asperity shear stress exceeds the benefit from the reduced contact area at textures. This leads to a substantial increase in the asperity friction loss. Consequently, the total friction also significantly increases (see Figure 6.17).

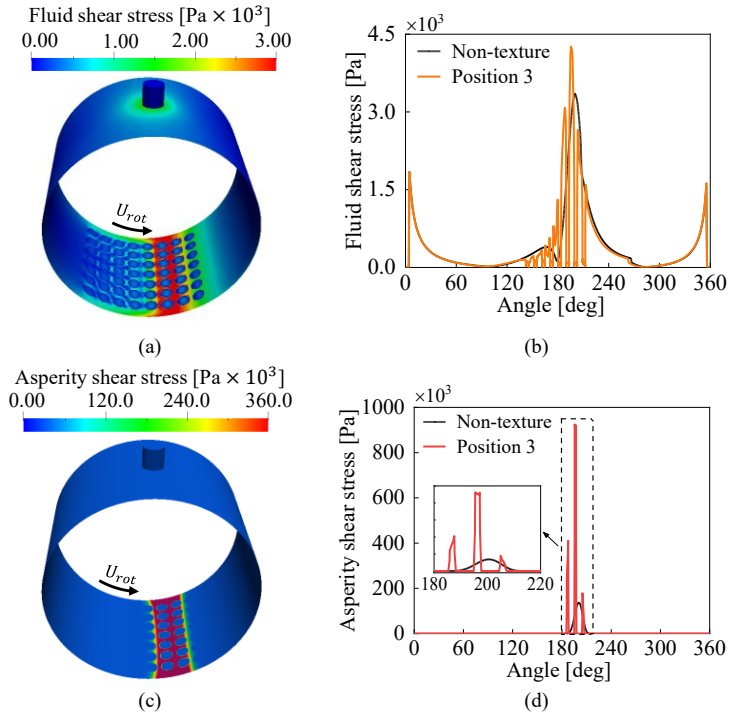


Figure 6.25 Shear stress distributions at Position 3 (a) Fluid shear stress contour (b) Fluid shear stress profiles (c) Asperity shear stress contour (d) Asperity shear stress profiles

**(d) Position 4**

When the textured area moves to Position 4, the hydrodynamic and asperity contact pressure distributions are illustrated in Figure 6.26. As can be seen from Figure 6.26 (a), the textures at this position are located downstream of the high-pressure region.

Therefore, the primary load-carrying region at this position is not interfered. This can also be observed from the nearly identical high-pressure region compared with the non-textured bearing in Figure 6.26 (b). Besides, a positive micro-hydrodynamic pressure at the cavitation region is generated. Consequently, a slight increase in the minimum film thickness is observed in Figure 6.17.

As shown in Figure 6.26 (c) and (d), the increase in the minimum film thickness leads to a slight decrease in the maximum contact pressure. In addition, the asperity contact region terminates earlier due to the increased film thickness at the textured area.

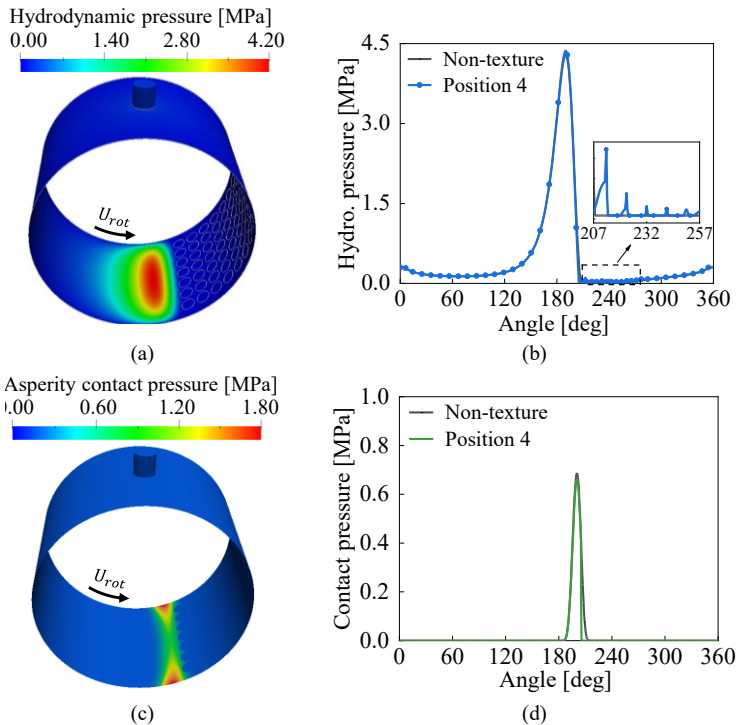


Figure 6.26 Pressure distributions at Position 4 (a) Hydrodynamic pressure contour (b) Hydrodynamic pressure profiles (c) Asperity pressure contour (d) Asperity pressure profiles

The fluid and asperity shear stress distributions at Position 4 are shown in Figure 6.27. First, the considerable reduction in the fluid shear stress can be observed in Figure 6.27 (a) and (b). This leads to a reduction in the fluid friction loss (see

Figure 6.18). In addition, as shown in Figure 6.27 (c) and (d), the increase in the minimum film thickness leads to a slight reduction in the maximum asperity shear stress. Simultaneously, these textures reduce the contact area. Therefore, a reduction in the asperity friction loss is observed in Figure 6.19. Consequently, the reduction in both the fluid and asperity friction leads to a lower total friction loss (see Figure 6.17).

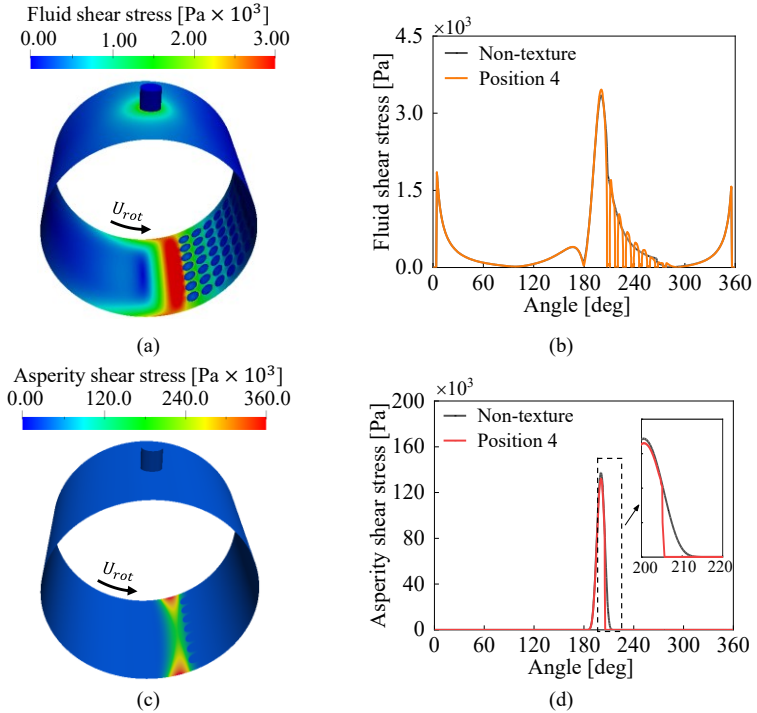


Figure 6.27 Shear stress distributions at Position 4 (a) Fluid shear stress contour (b) Fluid shear stress profiles (c) Asperity shear stress contour (d) Asperity shear stress profiles

**(e) Position 5**

The pressure and shear stress distributions are shown in Figure 6.28 and Figure 6.29. When the textures are located at Position 5, the textured area is downstream of and away from both the high-pressure and the asperity contact regions. Therefore, both the pressure and shear stress distributions are similar to those of the non-textured bearing. Consequently, both the minimum film thickness and friction loss are quite close to those of the non-textured bearing, as illustrated in Figure 6.16 and Figure 6.17.

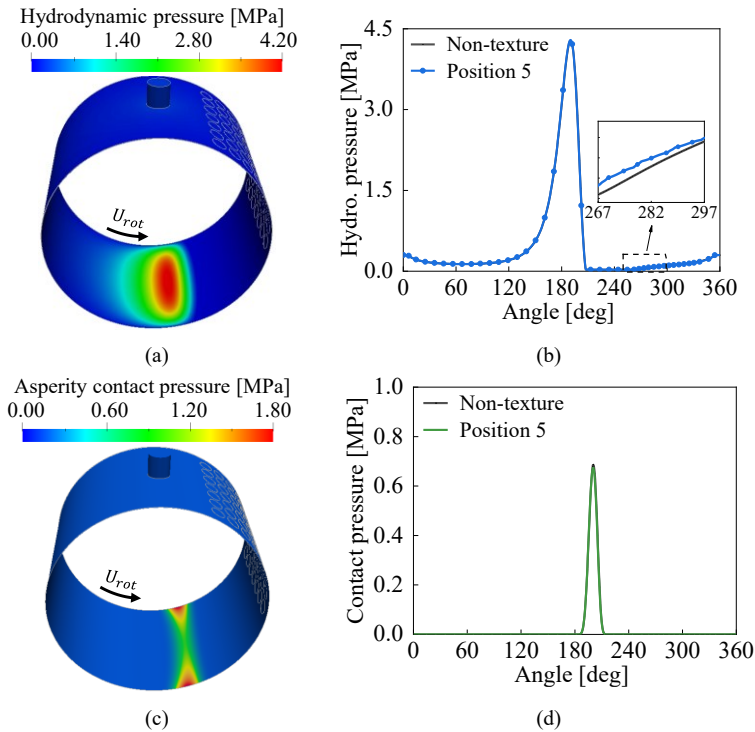


Figure 6.28 Pressure distributions at Position 5 (a) Hydrodynamic pressure contour (b) Hydrodynamic pressure profiles (c) Asperity pressure contour (d) Asperity pressure profiles

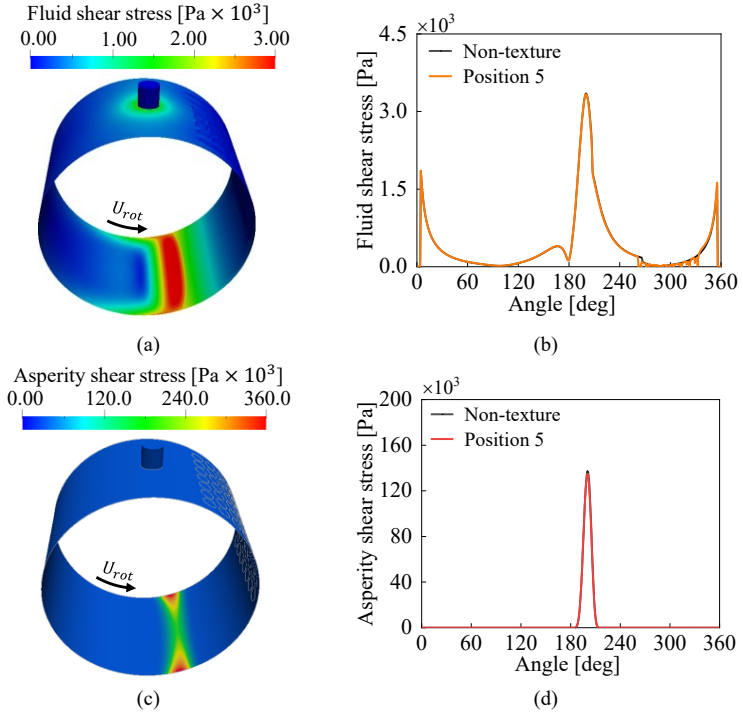


Figure 6.29 Shear stress distributions at Position 5 (a) Fluid shear stress contour (b) Fluid shear stress profiles (c) Asperity shear stress contour (d) Asperity shear stress profiles

In summary, textures can generate both negative and positive effects on the load-carrying capacity and the minimum film thickness under the mixed lubrication condition, as summarized in Figure 6.30. Both negative and positive effects are consistent with those under the hydrodynamic lubrication condition (see Figure 6.14). The contribution of textures to the load-carrying capacity depends on the balance between the beneficial micro-hydrodynamic effect and the interference effect on the high-pressure region (see Figure 6.30). Under the mixed-lubrication condition in this work, the interference effect is overall dominant.

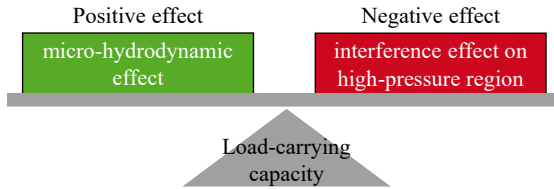


Figure 6.30 Effects of textures on the load-carrying capacity under mixed-EHL condition

The effect of textures on the friction loss under the mixed lubrication condition is governed by both fluid shear stress and asperity contact. The underlying mechanisms are summarized in Figure 6.31. Under the mixed lubrication in this work, both the positive and negative effects of textures on fluid shear stress are less pronounced than those observed under the hydrodynamic lubrication. Consequently, the effect of textures on the friction loss depends more on the asperity shear stress.

From the mechanism analysis of the asperity shear stress, textures can reduce the asperity contact area due to the locally increased film thickness. In addition, when the minimum film thickness is increased by textures, the asperity shear stress can be slightly reduced. In contrast, textures can also increase asperity shear stress when the minimum film thickness is decreased. A balance between the positive and negative effects shows that when textures are located downstream of the load-carrying region, they can slightly increase the minimum film thickness while simultaneously reducing the asperity contact area.

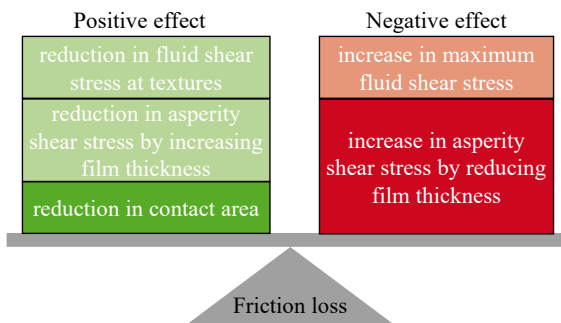


Figure 6.31 Effects of textures on the friction loss under the mixed lubrication

## 7. ML-based surrogate model of textured journal bearings

In Chapter 5, an N-S based mixed-EHL model is developed for textured journal bearings. Subsequently, in Chapter 6, this model is used to analyze the effect of texture parameters on the minimum film thickness and friction loss. The results show that both bearing performance parameters are significantly influenced by the texture geometry and distribution parameters. However, as introduced in Chapter 3.4, the N-S based CFD simulation compromises the computational efficiency. Consequently, the high degree of freedom in texture design parameters requires a huge amount of computational cost from the N-S based mixed-EHL model. To address this issue, an efficient ML-based surrogate model is developed in this chapter.

### 7.1. Input and output parameters

To develop the ML-based surrogate model, the input and output parameters should be first determined. In this work, four input parameters are selected based on the findings in Chapter 6, including texture geometry parameters (texture width ratio  $w_t/W$ , texture depth ratio  $d_t/C$ ) and texture distribution parameters (starting angle of texture area  $\alpha$ , texture coverage angle  $cov$ ). The design range of each input parameter is shown in Table 7.1. The determination of the design range is based on previous studies in Refs. [21,48,50,60]. The output parameters include the minimum film thickness and the friction loss of textured journal bearings.

Table 7.1 Design range with minimum and maximum values of input parameters

Parameters	Minimum value	Maximum value
Textured width ratio $w_t/W$ [-]	0.2	0.96
Texture depth ratio $d_t/C$ [-]	0.1	3
Starting angle of textured area $\alpha$ [°]	5	180
Texture coverage angle $cov$ [°]	5	170

Based on the design range of each input parameter, the design points are generated using the Latin hypercube sample function in MATLAB [151]. With this function, all design points are randomly distributed within the design range for each input parameter. In total, 220 design points with different input parameter combinations are generated. Then, simulations for each design point are conducted using the N-S based mixed-EHL model to calculate the output parameters under both hydrodynamic and mixed lubrication conditions. For each lubrication condition, the input design points

and their corresponding minimum film thickness and friction loss are stored as datasets ( $6 \times 220$  MATLAB structure array). Among these 220 datasets, 200 sets are used to train ML-based surrogate models. The remaining 20 datasets are used to evaluate the prediction accuracy of the trained surrogate models.

To ensure the stable and efficient training, the normalization is applied to both input and output parameters using the standardized min-max normalization function, that reads:

$$\hat{z} = \frac{z - z_{min}}{z_{max} - z_{min}}(q_{upper} - q_{lower}) + q_{lower} \quad (7-1)$$

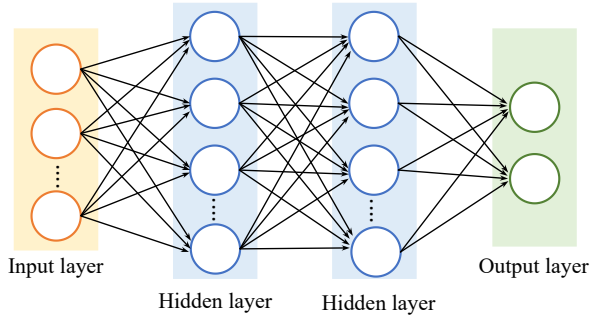
where  $\hat{z}$  is the final normalized value;  $z$  represents the original value of the data point;  $z_{min}$  and  $z_{max}$  denote the minimum and maximum values in the original datasets;  $q_{lower}$  and  $q_{upper}$  are the lower and upper normalized unit values, which are 0 and 1 in this work.

## 7.2. Theoretical background of ML-based surrogate model

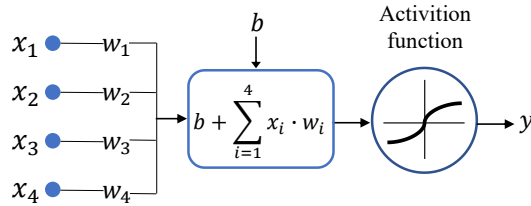
### 7.2.1. Model structure

To develop the ML-based surrogate model, the suitable algorithm needs to be selected. As a commonly used ML algorithm, Artificial Neural Network (ANN) model has demonstrated superior prediction performance compared to other ML regression models in various tribological applications [100,103,152,153]. Therefore, this work employs the ANN to predict the minimum film thickness and friction loss of textured journal bearings.

ANN is composed of interconnected nodes, designed to mimic the functioning of biological neurons [154]. The core of ANN consists of layers of artificial neurons, including an input layer, one or more hidden layers, and an output layer. The training data flows through the network in a feedforward way, from the input layer through the hidden layers to produce the outputs. Each connection between nodes is determined by the weights and biases. The structure of the whole feedforward neural network with two hidden layers as well as one neuron is exemplarily shown in Figure 7.1 [155].



(a) Structure of the neural network with two hidden layers



(b) One neuron with four inputs and one output

Figure 7.1 Architecture of the feed-forward neural network model

The training data flows from the input layer through the hidden layers to predict the outputs. By applying activation functions, the network can capture complex relationships between the inputs and outputs [152,154]. There are three popular activation functions for the hidden layer, including the hyperbolic tangent function (*tanh*) shown in Eq. (7-2), the logistic sigmoid function (*Sigmoid*) shown in Eq. (7-3), and the rectified linear unit function (*ReLU*) shown in Eq. (7-4). Regarding the activation function for the output layer, the pure linear function (*purelin*) shown in Eq. (7-5) is commonly used [152,154].

$$\tanh: f(x) = \frac{1}{1 + e^{-2x}} - 1 \quad (7-2)$$

$$\text{Sigmoid}: f(x) = \frac{1}{1 + e^{-x}} \quad (7-3)$$

$$\text{ReLU}: f(x) = \begin{cases} x, & x > 0 \\ 0, & x < 0 \end{cases} \quad (7-4)$$

$$\text{purelin: } f(x) = x \quad (7-5)$$

The parameters used to define an ANN model include the initial weights and biases, the number of layers, the number of neurons in each layer and the activation functions. The ANN parameters used in this work are shown in Table 7.2.

To avoid the unnecessary computational overhead or overfitting, the training stops when any of the following conditions is met: reaching the maximum number of epochs (1,000), achieving the target minimum error ( $10^{-4}$ ), reaching the target gradient descent value ( $10^{-6}$ ), or encountering the maximum number of consecutive failures (6). The values for each parameter are the default values provided by MATLAB [156].

Table 7.2 Design parameters for the ANN model

Parameter	Specification
Training algorithm	Levenberg-Marquardt algorithm
Number of hidden layers	Tuned based on the datasets
Number of neurons in hidden layer	Tuned based on the datasets
Activation function for hidden layer	Tuned based on the datasets
Activation function for output layer	<i>Purelin</i> [152,154]
Learning rate	Tuned based on the datasets
Initial weights and biases	Tuned based on the datasets
Division of data	Random
	70% - Training
Data division	15% - Validation
	15% - Test

---

### 7.2.2. Performance evaluation

To evaluate the prediction performance of the ANN model, the mean square error (*MSE*) and the correlation coefficient (*R*) are calculated. *MSE*, defined in Eq. (7-6), is a measure of the average squared difference between the predicted and target values.

$$MSE = \frac{1}{N} \sum_{i=1}^N (y_i - \hat{y}_i)^2 \quad (7-6)$$

where  $y_i$  represents the target value, and  $\hat{y}_i$  represents the predicted value from the ML models. A lower  $MSE$  value indicates better estimation performance, while a higher  $MSE$  value indicates poorer estimation performance.

The correlation coefficient ( $R$ ), defined in Eq. (7-7), provides information about the correlation between the predicted and target values.

$$R = \frac{\sum_{i=1}^N (y_i - \bar{y}_i) (\hat{y}_i - \bar{\hat{y}}_i)}{\sqrt{\sum_{i=1}^N (y_i - \bar{y}_i)^2 \sum_{i=1}^N (\hat{y}_i - \bar{\hat{y}}_i)^2}} \quad (7-7)$$

where  $\bar{y}_i$  and  $\bar{\hat{y}}_i$  are the mean target and predicted values, respectively. A high  $R$  value close to 1 indicates a strong relationship between the predicted and target values. Conversely, an  $R$  value of 0 suggests no correlation or a random connection between the predicted and target values [157].

### 7.3. Model setup

With the identical datasets, the prediction accuracy of the ANN model depends on the network architecture [158], as well as the appropriate initial weights and biases for each neuron [159]. To improve the prediction accuracy of the ANN model based on the current datasets, the ANN model is optimized through the cross-validation-based hyperparameter optimization and the genetic algorithm. The cross-validation (CV) method is used to evaluate various architecture parameter combinations, which helps to identify an optimal neural network architecture. Subsequently, the genetic algorithm (GA) is utilized for searching the appropriate initial weights and biases for each neuron.

#### 7.3.1. Determination of the network architecture

In this work, the architecture hyperparameters of the ANN model is determined through the widely-used 5-fold cross-validation, as shown in Figure 7.2 [160]. The datasets are split into 5 subsets of approximately equal size. The model is trained 5 rounds. For each round  $i$  (1 to 5), 4 folds are used for training and the remaining fold is used for testing. This process ensures that all the datasets are used for training and testing simultaneously and every data point is used for testing exactly once. Therefore, it ensures the high reliability and generalizability. To evaluate the overall performance

of the ANN model with different architectures, the  $MSE$  value on the test fold is calculated across all iterations. The average performance is obtained by Eq. (7-8).

$$MSE_{avg} = \frac{1}{5} \sum_{i=1}^5 MSE_i \quad (7-8)$$

where,  $MSE_{avg}$  is the average  $MSE$  value for all iterations and  $MSE_i$  is the  $MSE$  value for each iteration.

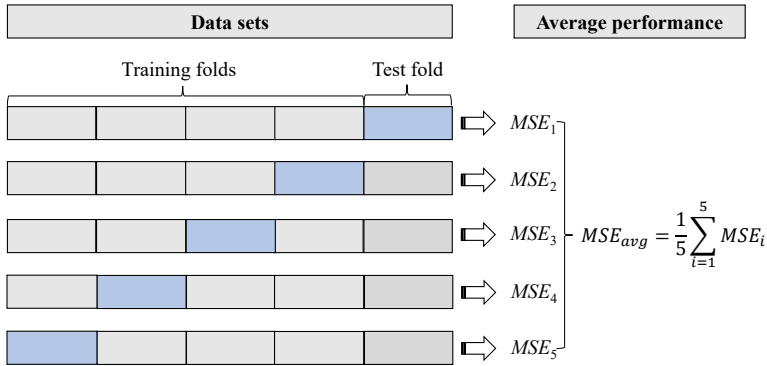


Figure 7.2 Process of the 5-fold cross-validation

In this work, four key architecture parameters of the ANN model are selected: the number of hidden layers, the number of neurons in each hidden layer, the learning rate of the ANN model and the type of activation function in hidden layers [161]. The optimization range of each parameter is shown in Table 7.3.

Table 7.3 Optimization range of architecture parameters for the ANN model

Parameter	Range
Number of hidden layers	1-3
Number of neurons in hidden layer	2-20
Learning rate	$10^{-1}$ - $10^{-5}$
Activation function in hidden layers	<i>tanh</i> , <i>sigmoid</i> , <i>ReLU</i>

As the next step, the optimization process for the architecture parameters is conducted through the following steps:

**Step 1:** The optimization range for four architecture parameters is defined as Table 7.3 shows.

**Step 2:** Based on the optimization range, four architecture parameters are fully combined using nested loops. In this work, 4275 groups of combinations are generated for each ANN model.

**Step 3:** Each combination undergoes 5-fold cross-validation. The  $MSE$  value of each combination is evaluated on the 5 different test folds, respectively.

**Step 4:** The average  $MSE$  value ( $MSE_{avg}$ ) for each combination is recorded and compared. The best parameter combination with the minimum  $MSE_{avg}$  is identified at the end.

**Step 5:** The optimal parameter combination is outputted and therefore the optimal ANN architecture is determined.

### **7.3.2.Determination of initial weights and biases**

In addition to the architecture parameters, the initial weights and biases also have a considerable impact on the prediction accuracy of the ANN model [159,162]. To further improve the prediction accuracy, the genetic algorithm (GA) is used to determine the optimal initial weights and biases based on the optimal architecture parameters. The GA is derived from the principle of natural selection and population genetic. During the process of the GA, optimization parameters are incorporated into a population of encoded individuals, which are selected, crossed over, and mutated based on an objective function [163]. The optimization process of the GA in this work is shown in Figure 7.3 [164].

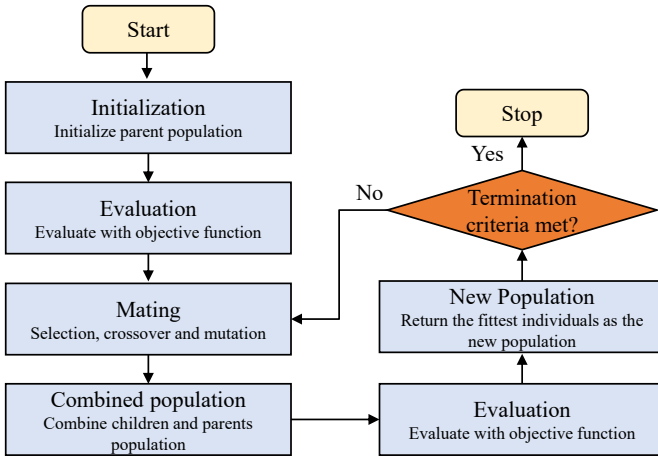


Figure 7.3 Optimization process of the GA model

The process starts from initializing the GA parameters, including the population size ( $S$ ), the crossover probability ( $P_c$ ), the mutation probability ( $P_m$ ), the generation size ( $G_s$ ), and the maximum stalled generations ( $S_{max}$ ). The values of these parameters are listed in Table 7.4.

Table 7.4 Parameters of the GA model

Parameters	Value	Parameters	Value
Population size $S$	150	Selection function	Tournament selection
Crossover probability $P_c$	0.8	Crossover function	Two-point crossover
Mutation probability $P_m$	0.15	Mutation function	Gaussian mutation
Generation size $G_s$	150	-	-
Maximum stalled generations $S_{max}$	50	-	-

In the next step, the objective function value of each individual in the population is evaluated with the objective function presented in Eq. (7-9). Minimization of the objective function value is the goal of the optimization. In the current work, the objective function value refers to the difference between 1 and the  $R$  values for training, validation, test and overall datasets.

$$fit(x) = \sum_{i=1}^4 |R_i(x) - 1| \quad (7-9)$$

where  $R_i(x)$  represents the  $R$  value under the individual  $x$ , and the indices  $i = 1, 2, 3, 4$  refer to training, validation, test and overall datasets, respectively;  $x$  is the initial weights and biases of the neural network:

$$x = [\mathbf{w}_{in,1}, \mathbf{B}_1, \mathbf{w}_{1,2}, \mathbf{B}_2, \dots, \mathbf{w}_{l,out}, \mathbf{B}_{out}] \quad (7-10)$$

where  $l$  is the number of hidden layers;  $\mathbf{w}_{in,1}, \mathbf{w}_{1,2}, \mathbf{w}_{l,out}$  represent the weight matrices from the input layer to the first hidden layer, from the first hidden layer to the second hidden layer, and from the  $l^{th}$  hidden layer to the output layer, respectively;  $\mathbf{B}_1, \mathbf{B}_2, \mathbf{B}_{out}$  represent the bias vectors of the first hidden layer, the second hidden layer, and the output layer, respectively.

The termination criteria for the optimization are either reaching the maximum generation size or no improvement in the best objective function value over the maximum number of stalled generations. If the criteria cannot be met in the current population, the mating will be initiated to recombine parent population and create offspring through selection, crossover and mutation. Subsequently, a new population is generated and will be evaluated repeatedly until the termination criteria are achieved. Eventually, after the optimization through the GA, the optimal initial weights and biases for each neuron are determined and utilized in the training process of the ANN model.

## 7.4. Results and discussion

### 7.4.1. ANN model under the hydrodynamic lubrication

In this section, the ANN model is trained to predict the minimum film thickness and friction loss of journal bearings under the hydrodynamic lubrication condition with a load of 500N and a rotational speed of 1,000rpm. First, the optimized values of each architecture parameters are determined through the CV-based hyperparameter optimization and are shown in Table 7.5. Based on the optimized architecture, the GA-based optimization is conducted to determine the optimal initial weights and biases. Then, with these optimized settings, the ANN model is trained and the  $R$  values are computed.

Table 7.5 Optimized values of architecture parameters for the ANN model

Parameter	Optimized range
Number of hidden layers	2
Number of neurons in hidden layer	[16,14]
Learning rate	$10^{-2}$
Activation function on hidden layers	<i>ReLU</i>

The  $R$  values describe the relationship between the predicted and the target values. Their values of the trained ANN model are depicted in Figure 7.4. It can be observed that the  $R$  values for the training, validation, test, and overall datasets are 0.993, 0.982, 0.984 and 0.988, respectively. Therefore, it can be deduced that the predicted values estimated by the ANN model are overall consistent with the actual values.

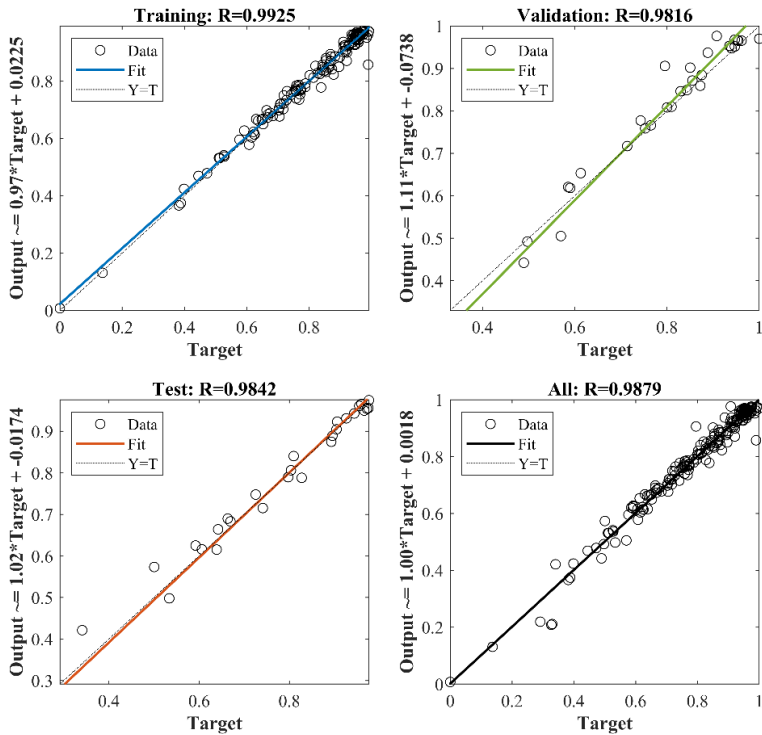
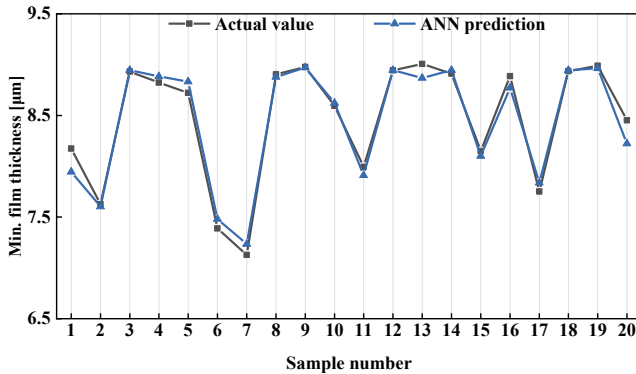
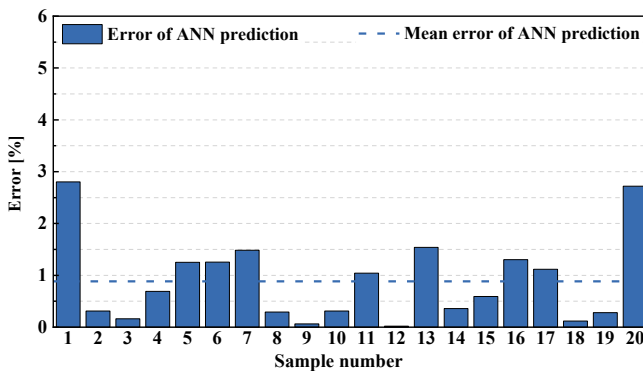


Figure 7.4  $R$  values for the training, validation, test, and overall datasets

Furthermore, to evaluate the prediction accuracy of the trained ANN model more straightforwardly, the minimum film thickness and the friction loss of 20 evaluation datasets are predicted. The predicted results are then compared with the actual results from the N-S based mixed-EHL model. The comparison results, along with the errors between the predicted and actual values, are depicted in Figure 7.5 and Figure 7.6. It can be found from Figure 7.5 (a) and Figure 7.6 (a) that the overall trend of the predicted values by the ANN model is consistent with the actual values for both parameters. Regarding the prediction accuracy for the minimum film thickness, the average accuracy stands at 99.1%, and the maximum prediction error is below 3% for all datasets. In terms of the prediction accuracy for the friction loss, the average prediction accuracy is 99.2% with the maximum error around 2%.

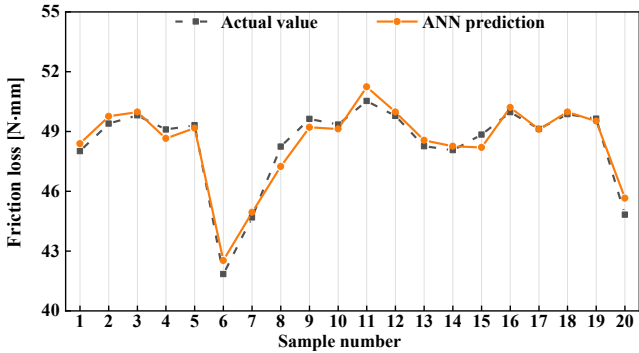


(a) Comparison of the actual and the predicted values of minimum film thickness

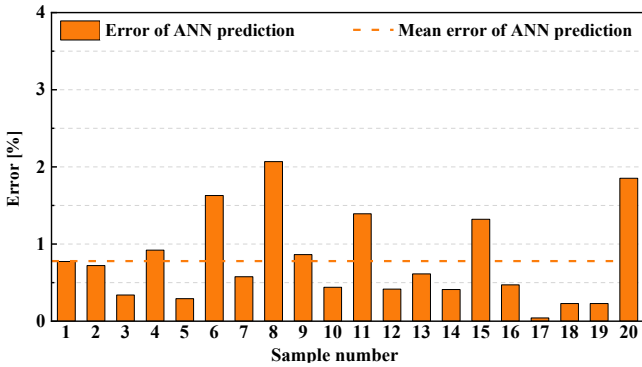


(b) Prediction errors of ANN for minimum film thickness

Figure 7.5 Prediction performance of ANN for minimum film thickness



(a) Comparison of the actual and the predicted values of friction loss.



(b) Prediction errors of ANN for friction loss.

Figure 7.6 Prediction performance of ANN for friction loss

In addition to the accuracy, the efficiency of the developed ML-based surrogate model is quantified by the prediction time for one texture design combination. For the N-S based mixed-EHL model, the simulation time under the hydrodynamic condition (excluding the time for mesh generation and boundary setup) requires approximately 300~625 core hours. All simulations of this work are conducted with the partition *c23ms* in RWTH High Performance Computing. More details of this partition can be found in Ref. [165]. With the surrogate model, the friction loss and the minimum film thickness can be predicted within 1 second for one texture design combination. In conclusion, the trained ANN model can accurately and efficiently predict the minimum film thickness and friction loss of textured journal bearings.

### 7.4.2. ANN model under the mixed lubrication

The second ANN model is trained to predict the minimum film thickness and friction loss under the mixed lubrication (with the load of 500N and the rotational speed of 80rpm). After the CV-based hyperparameter optimization, the optimized values of architecture parameters are shown in Table 7.6. Compared with the optimal architecture results for the hydrodynamic lubrication case in Table 7.5, it can be seen that the suitable network architecture is highly dependent on the specific applications and datasets, which was also demonstrated in Refs. [152,166]. The CV-based hyperparameter optimization introduced above offers a comprehensive way to determine the suitable architecture parameters for different applications and datasets.

Table 7.6 Optimized values of architecture parameters for the ANN model

Parameter	Optimized range
Number of hidden layers	3
Number of neurons in hidden layer	[14,12,12]
Learning rate	$10^{-3}$
Activation function on hidden layers	<i>ReLU</i>

Following the same optimization procedure, the ANN model for the prediction of minimum film thickness and friction loss under the mixed lubrication is also optimized by identifying the appropriate initial weights and biases for each neuron. The  $R$  values of the trained ANN model are depicted in Figure 7.7. The  $R$  values for the training, validation, test, and overall datasets are 0.999, 0.995, 0.992 and 0.998, respectively. Therefore, it can be concluded that the predicted values of the two output parameters are generally in good agreement with the actual values.

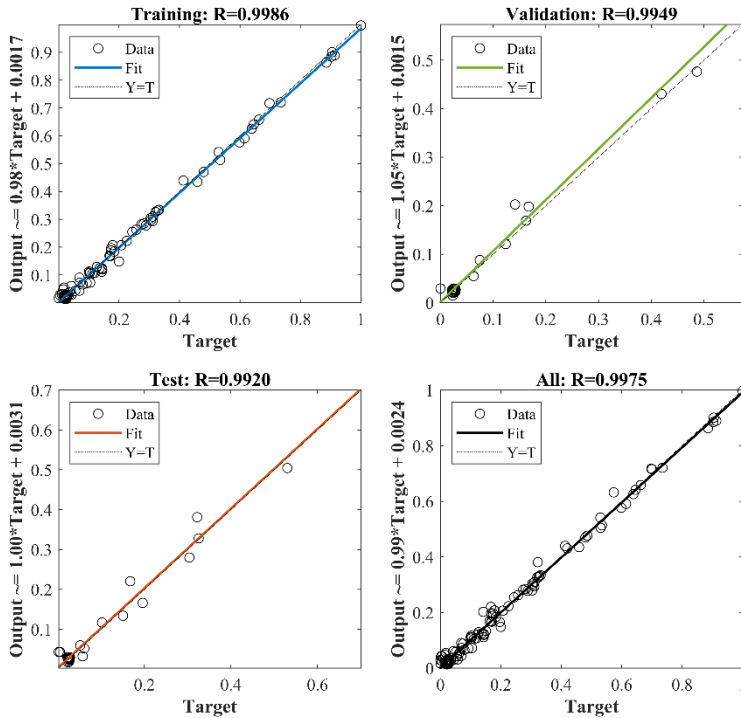
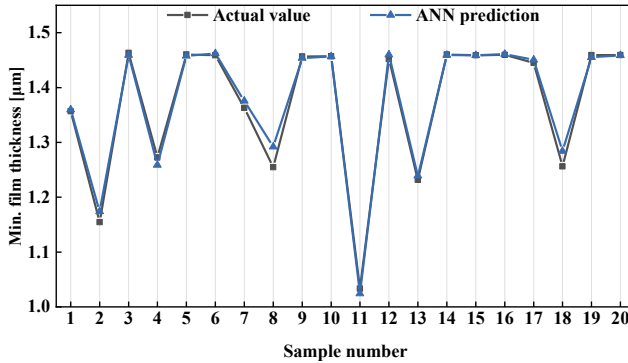
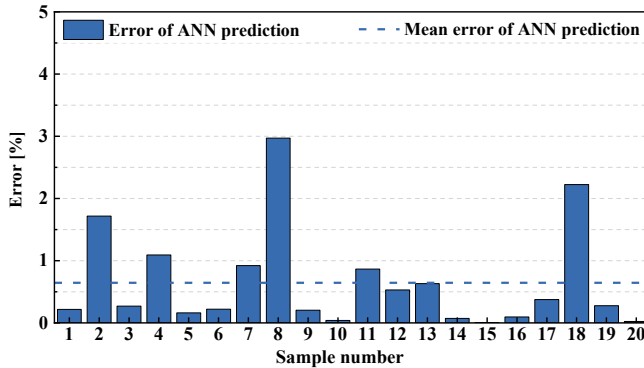


Figure 7.7 R values for the training, validation, test, and overall datasets

Based on the 20 evaluation datasets, a comparison between the actual values and the predicted values by the ANN model for the minimum film thickness is presented in Figure 7.8. Overall, the predicted minimum film thickness values closely match the actual values. Regarding the prediction accuracy, the ANN model achieves an average accuracy of 99.3%, with all prediction errors below 3%.



(a) Comparison of the actual and the predicted values of minimum film thickness



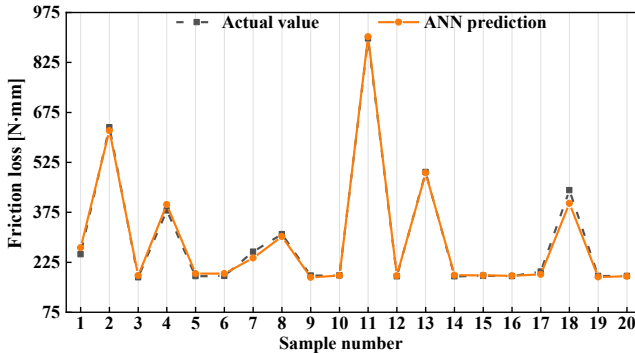
(b) Prediction errors of ANN for minimum film thickness.

Figure 7.8 Prediction performance of ANN for minimum film thickness

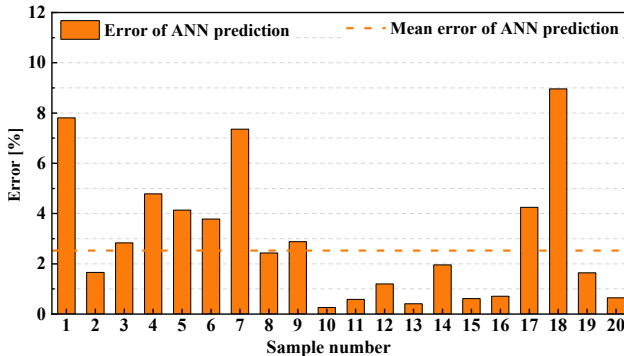
In addition, a comparison between the predicted and actual values of friction loss is presented in Figure 7.9. As illustrated in Figure 7.9(a), the predicted values of friction loss also show close agreement with the actual values. As indicated in Figure 7.9(b), the ANN model achieves a prediction accuracy of 97.1% for the friction loss. However, the maximum error is around 8.9 %, which is higher than that for the minimum film thickness. One possible explanation is that the friction loss exhibits a broader range of variation in response to changes in texture design parameters. As analyzed in Subchapter 6.2, under mixed lubrication conditions, texture design parameters influence the friction loss through several interrelated factors, including the hydrodynamic pressure, contact pressure, fluid shear stress, and contact shear stress. Hence, the prediction of friction loss is inherently more challenging than that

of the minimum oil film thickness. Consequently, the prediction error for the friction loss is higher than that for the minimum oil film thickness.

Regarding the prediction efficiency, the surrogate model can also predict both the friction loss and minimum film thickness within 1 second for each texture design combination. In contrast, one N-S based mixed-EHL simulation requires approximately 300 to 800 core hours under the mixed lubrication condition (excluding the time for mesh generation and boundary setup). This indicates the high efficiency of the surrogate model.



(a) Comparison of the actual and the predicted values of friction loss.



(b) Prediction errors of ANN for friction loss.

Figure 7.9 Prediction performance of ANN for friction loss

In summary, after the combined optimization through the CV-based hyperparameter optimization and the GA, the suitable network architecture as well as the optimized initial weights and biases can be identified for the datasets under different operating

conditions. The ANN-based surrogate models developed in this work can predict the friction loss and minimum film thickness of textured journal bearings within 1 second for each case, with the average accuracy of over 97% for both conditions. These results demonstrate both the efficiency and high accuracy of the developed surrogate models.



## 8. Optimization design of textured journal bearings

In Chapter 7, the ML-based surrogate models are developed, which can efficiently and accurately predict the minimum film thickness and friction loss under hydrodynamic and mixed lubrication conditions. Based on the surrogate models, the optimization design of texture geometry and distribution is conducted in this chapter. First, the theoretical background of the Non-Dominated Sorting Genetic Algorithm-II (NSGA-II) is introduced. Then, the multi-objective optimization model based on the NSGA-II is set up, aiming for a lower friction loss and a higher minimum film thickness of textured journal bearings. Finally, the optimized texture geometry and distribution parameters are determined for two lubrication conditions.

### 8.1. Theoretical background of optimization model

As introduced in Subchapter 3.4, NSGA-II is inspired by biological evolution. It extends the standard Genetic Algorithm (GA) by incorporating the non-dominated sorting and a crowding distance mechanism [167]. Thereby, this method is more capable of handling the optimization problems with multiple and potentially conflicting objectives [126]. The flowchart of the NSGA-II algorithm is shown in Figure 8.1, and the procedure is introduced below.

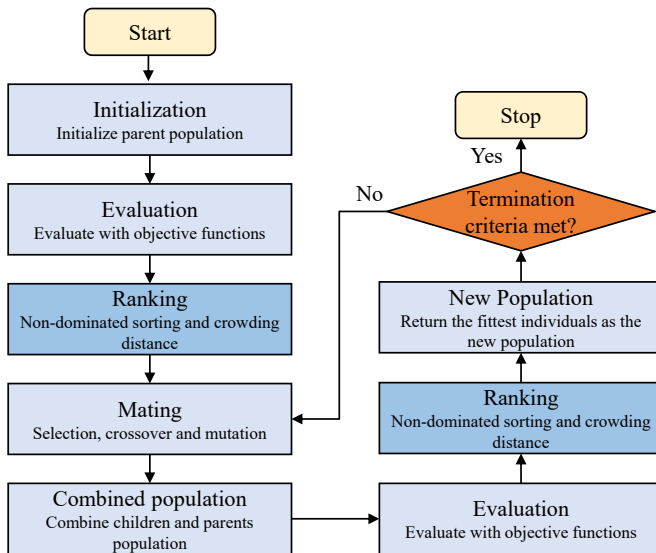


Figure 8.1 The flowchart of the NSGA-II

**Step 1:** The optimization starts from initializing a random population.

**Step 2:** The objective functions are defined and evaluated for each individual within the initialized population. The objective functions are formulated on the basis of the design variables, the objective function vector and constraints, as Eq. (8-1) shows. In word, it is to minimize the objective function vector  $f(X_d)$  by varying the design variables  $X_d$  within their design limits [168]. The function vector  $f(X_d)$  includes multiple functions  $f_1(X_d), f_2(X_d), \dots, f_m(X_d)$ , which represent multiple objectives.

$$\text{Minimize } f(X_d) = [f_1(X_d), f_2(X_d), \dots, f_m(X_d) ]$$

$$\text{by varying } X_d = (x_1, x_2, \dots, x_n) \quad (8-1)$$

$$\text{subject to } x_i \in [L_i, U_i] \quad (i= 1, \dots, n)$$

where  $f(X_d)$  is the objective function vector,  $X_d$  is a vector formed by independent design variables;  $L_i$  and  $U_i$  are the minimum and maximum limits of each design parameter, respectively;  $m$  and  $n$  are the number of objective functions and design parameters, respectively.

**Step 3:** Based on the objective function values of each individual, a rank is calculated. This ranking represents an improvement of the NSGA-II algorithm compared to the traditional GA. In single-objective optimization with GA, individuals are simply ranked according to their single-objective function value. However, in multi-objective optimization with two or more objectives, sorting based on a single-objective function value is insufficient. Therefore, the ranking process in NSGA-II involves non-dominated sorting and the calculation of crowding distance.

Regarding non-dominated sorting, one individual dominates another if all its objective function values are lower. For example, an individual dominated by  $N_d$  individuals is assigned a rank of  $N_d+1$ . Individuals with lower ranks have a higher probability of being selected. In addition, crowding distance measures the spacing between adjacent individuals. A larger crowding distance indicates better diversity. Thus, among individuals with the same rank, those with greater crowding distance have a higher probability of being selected for the parent population in the next generation [169].

**Step 4:** Based on the rank, the parent population for the next generation is selected using the tournament selection method [169]. The selected parents are then mutated and crossed over to generate the children population.

**Step 5:** The children population is combined with the parent population to form an extended population. The objective function values are evaluated again for the combined population.

**Step 6:** For each individual in the combined population, the ranking including the non-dominated sorting and the calculation of crowding distance are conducted again as introduced in Step 3.

**Step 7:** Based on the ranking, the fittest individuals are selected as the new population.

**Step 8:** The algorithm terminates when the termination criteria are met. The termination criteria for the optimization are either reaching the maximum number of generation or no improvement in the objective function values over the maximum number of stalled generations. If the criteria cannot be met in the current population, the iteration (Steps 4 to 6) is repeated [169]. Eventually, the algorithm stops and the output design variables are outputted.

**Step 9:** In multi-objective optimization, several objective variables must be optimized simultaneously, which sometimes leads to competing objectives. Accordingly, the concept of Pareto optimality is employed to identify optimal design variants. A variant is considered Pareto-optimal if it is not dominated by any other evaluated variant [170]. Specifically, one variant dominates another if it demonstrates better values for all objective variables. The set of all Pareto-optimal variants in the design space constitutes the Pareto front in the objective space. Once the optimization results are presented as a Pareto front, the most suitable design variant is usually selected based on the engineering requirements or standard methods [170].

## 8.2. Model setup

In this work, the optimization problem is defined as: minimizing the total friction loss ( $f_{\text{total}}(X_d)$ ), and the negative minimum film thickness ( $-h_{\text{min}}(X_d)$ ) by varying the design variables  $X_d$ . The minimum film thickness ( $h_{\text{min}}(X_d)$ ) is set as a negative value because it needs to be maximized. Both  $f_{\text{total}}(X_d)$  and  $h_{\text{min}}(X_d)$  are the output parameters from the ML-based surrogate models in Chapter 7.

The design variables  $X_d$  include: textured width ratio ( $w_t/W$ ), texture depth ratio ( $d_t/C$ ), starting angle of textured area ( $\alpha$ ) and texture coverage angle ( $cov$ ). The design range of each design parameter is shown in Table 7.1 in Chapter 7.

Therefore, the objective functions in Eq. (8-1) can be reformulated in this work as:

Minimize:  $f(X_d) = [f_{\text{total}}(X_d), -h_{\text{min}}(X_d)]$

by varying  $X_d = \left( \frac{w_t}{W}, \frac{d_t}{C}, \alpha, cov \right)$  (8-1)\*

within the design range shown in Table 7.1

As introduced in Step 9 of the optimization procedure in the previous section, once the optimization results are presented as a Pareto front, the most suitable design variant should be selected. In the context of textured journal bearings, the selection criterion is to minimize the friction loss without compromising the load-carrying capacity. Therefore, the final design configuration is the combination that achieves the lowest friction loss while maintaining a minimum film thickness no less than that of the non-textured journal bearing.

### 8.3. Results and discussion

In this section, following the previously introduced optimization procedure, the optimal design combinations of texture geometry and distribution parameters are first identified for both cases under hydrodynamic and mixed lubrication conditions. Subsequently, the minimum film thickness and friction losses of the optimized textured journal bearings are compared with those of the non-textured journal bearing.

#### 8.3.1. Optimization results for hydrodynamic lubrication

For the case under the hydrodynamic lubrication condition (with the load of 500N and the rotational speed of 1000rpm), the optimal texture geometry and distribution parameters are summarized in Table 8.1. The pressure and fluid shear stress for the optimized textured journal bearing are shown in Figure 8.2.

Table 8.1 Optimized value of each texture design parameters

Design Parameters	Optimized value
Textured width ratio $w_t/W$ [-]	0.89
Texture depth ratio $d_t/C$ [-]	0.78
Starting angle of textured zone $\alpha$ [°]	25.21
Texture coverage angle $cov$ [°]	94.43

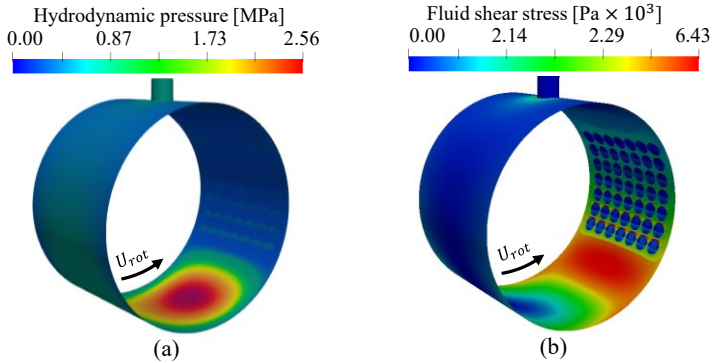


Figure 8.2 Hydrodynamic pressure and fluid shear stress distributions for the optimized textured journal bearing (a) Hydrodynamic pressure (b) Fluid shear stress

Under this operating condition, the optimal texture width ratio is determined to be 0.89. This value aligns well with the findings summarized by Marian et al. [63], which concluded that the optimized texture width ratio ranged between 0.1 and 1.0. Regarding the optimal texture depth ratio of 0.78, this result also agrees with their conclusion that the optimal texture depth ratio typically ranged between 0.4 and 0.8 [42,63].

Regarding the optimal distribution of textures in journal bearings, there is still no common conclusions [11,13,63]. From Figure 8.2, it can be observed that the optimal texture distribution in this case is located downstream of the high-pressure region, and close to the minimum film thickness region. This result aligns with the conclusions in Chapter 6.1, which indicate that placing textures downstream of the high-pressure region reduces friction loss while slightly increasing the minimum film thickness. The reduction in friction loss occurs because the fluid shear stress is effectively reduced in this configuration, as shown in Figure 8.2 (b). Additionally, with this texture distribution, the primary load-carrying region of the bearing remains undisturbed, and the micro-hydrodynamic effect within the cavitation region slightly enhances the minimum film thickness. Besides, this optimized texture distribution can be supported by the results from Tala-Ighil et al. [21], who compared 25 texture distributions and found that placing textures in the pressure-decreasing region was beneficial.

Eventually, a comparison of the minimum film thickness and friction losses between the optimized textured and non-textured journal bearings is summarized in Table 8.2. The optimized textured journal bearing demonstrates an 11.97% reduction in friction loss compared to the non-textured bearing, while the minimum film thickness slightly increases by approximately 1.46%.

Table 8.2 Comparison between the optimized and the non-textured bearing under hydrodynamic lubrication condition

	Minimum film thickness [ $\mu\text{m}$ ]	Friction loss [ $\text{N}\cdot\text{mm}$ ]
Non-textured bearing	8.89	51.45
Textured bearing	9.02	45.29
Difference [%]	+1.46	-11.97

### 8.3.2. Optimization results for mixed lubrication

Following the same optimization procedure, the optimal texture design parameters are obtained for the case under the mixed lubrication condition (with the load of 500N and the rotational speed of 80rpm). The optimized texture geometry and distribution parameters are listed in Table 8.3. Subsequently, both the hydrodynamic pressure and asperity pressure for the optimized textured journal bearing are shown in Figure 8.3. The fluid shear stress and asperity shear stress are illustrated in Figure 8.4.

Table 8.3 Optimized value of each texture design parameter

Design Parameters	Optimized value
Textured width ratio $w_t/W$ [-]	0.86
Texture depth ratio $d_t/C$ [-]	0.51
Starting angle of textured zone $\alpha$ [ $^\circ$ ]	79.23
Texture coverage angle $cov$ [ $^\circ$ ]	75.06

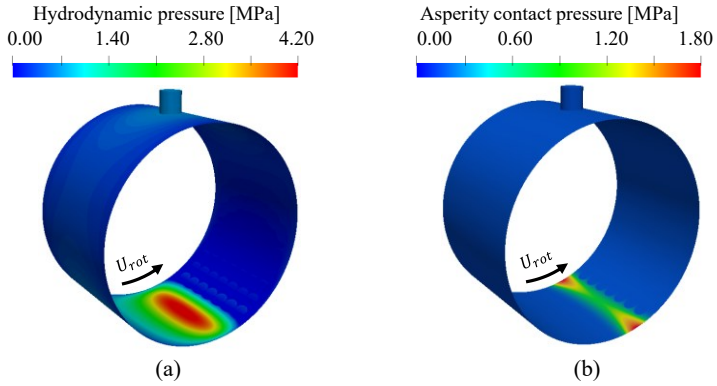


Figure 8.3 Pressure distributions for the optimized textured journal bearing (a) Hydrodynamic pressure (b) Contact pressure

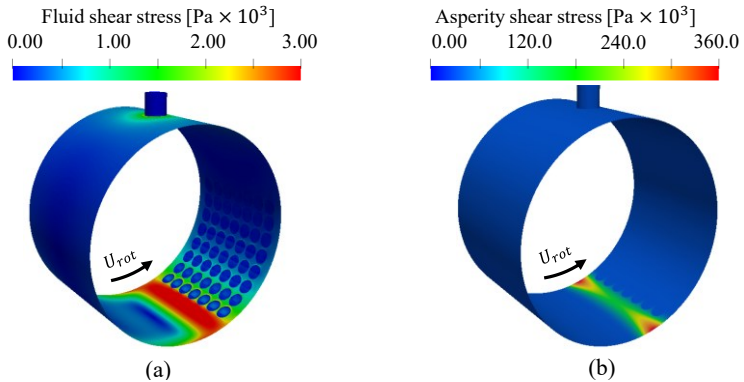


Figure 8.4 Shear stress distributions for the optimized textured journal bearing (a) Fluid shear stress (b) Asperity shear stress

Under this operating condition, the optimized value of the texture width ratio is 0.86, which still aligns with the previously concluded range of 0.1 to 1.0 by Marian et al. [63]. Moreover, the optimal texture depth ratio of 0.51 also remains within the recommended range of 0.4 to 0.8 [63]. However, compared to the optimized results for the hydrodynamic lubrication, the optimal depth ratio is decreased. This decrease may be attributed to the local influence of the film thickness on the optimal texture depth [60,68]. Due to this local influence, the shallower textures demonstrate a more pronounced contribution under a thinner film thickness. In this work, the minimum film thickness under the mixed lubrication is significantly reduced compared to that

under the hydrodynamic lubrication, thus leading to a lower optimal texture depth ratio.

For the optimized texture distribution, as shown in Figure 8.3 and Figure 8.4, the optimal texture position remains downstream of the primary load-carrying area. The optimized texture distribution under the mixed lubrication shifts upstream compared to that under the hydrodynamic lubrication. This can be explained by the conclusion in Chapter 6.2, which demonstrates a shift of the primary load-carrying region upstream under the mixed lubrication. Consequently, both the starting angle and the overall coverage of the textured area move upstream, causing the entire texture distribution to shift upstream. Meanwhile, the textures with this distribution slightly reduce the asperity contact area. Such a difference in the optimal texture distributions between the two lubrication conditions clearly indicates that optimal design parameters highly depend on the operating conditions of journal bearings. Therefore, it is necessary to consider lubrication conditions when designing textured journal bearings.

After optimizing texture design parameters under this mixed lubrication condition, a comparison of the minimum film thickness and friction loss between textured and non-textured bearings is provided in Table 8.4. Through the optimization, the friction loss of the textured bearing decreases by 10.39%, while the minimum film thickness increases by 1.38%.

Table 8.4 Comparison between the optimized and the non-textured bearing under mixed lubrication condition

	Minimum film thickness [ $\mu\text{m}$ ]	Friction loss [ $\text{N}\cdot\text{mm}$ ]
Non-textured bearing	1.45	187.82
Textured bearing	1.47	168.30
Difference [%]	+1.38	-10.39

In summary, the optimal texture width ratios remain consistent under both lubrication conditions. In contrast, the optimal texture depth ratio and texture distribution are highly dependent on operating conditions. Specifically, when the lubrication regime shifts from hydrodynamic to mixed lubrication, the optimal texture depth ratio decreases, and the optimal texture distribution moves upstream. A general recommendation is to locate textures downstream and close to the primary load-carrying region. This distribution can minimize friction loss without interfering the load-carrying capacity of journal bearings. This insight provides a fundamental guidance for the design of texture position in journal bearings.

## 9. Summary and outlook

### 9.1. Summary

Journal bearings have been widely used in many industrial applications, including various subsystems in engines and powertrains. A growing demand for energy efficiency in machinery requires lower friction loss and higher load-carrying capacity in journal bearings. Surface textures have shown promising potential in reducing the friction and improving the load-carrying capacity of journal bearings. However, their detrimental effects have also been reported in cases of improper design of textures. Therefore, a validated method for designing textured journal bearings is becoming increasingly important.

To achieve this aim, three research needs are identified in this dissertation. Based on these research needs, a design strategy is proposed, which consists of three sub-models. Each sub-model addresses a specific research need. The key findings for each research need (marked in bold) are summarized as follows:

**(a) N-S based mixed-EHL model, which can accurately predict both the load-carrying capacity and friction loss under different lubrication conditions:**

To address this research need, a N-S based mixed-EHL model for the textured journal bearings is developed in this work. The contribution and novelty of this model are integrating and connecting the existed models of deformation, load balance, and surface roughness into the accurate N-S based framework. The input parameters of this model include bearing parameters, textures parameters, operating parameters as well as lubricant and material parameters. This model is capable of predicting the minimum film thickness and friction loss of textured journal bearings from (elasto-)hydrodynamic lubrication to mixed lubrication.

Experimental validations in terms of the pressure distribution, minimum film thickness, and friction loss are conducted under both (elasto-)hydrodynamic lubrication and mixed lubrication. The comparison between numerical and experimental results demonstrates that the error in the pressure distribution remains between 2% and 15%, depending on operating conditions. The maximum error in the minimum film thickness is approximately 11%. The error in the friction coefficient is lower than 0.003. This satisfactory agreement proves that the developed mixed-EHL model can accurately predict both the load-carrying capacity and friction loss of textured journal bearings under various lubrication conditions.

Based on the mixed-EHL model, the influence of surface textures on the minimum film thickness and friction loss is studied under both the hydrodynamic and mixed lubrication conditions. Under hydrodynamic lubrication conditions, textures can generate the micro-hydrodynamic pressure, which is beneficial for increasing the load-carrying capacity and further increasing the minimum film thickness. Meanwhile, textures may interfere with the high-pressure region, which can reduce the load-carrying capacity and the minimum film thickness. Regarding the friction losses, textures can significantly reduce the fluid shear stress, thus lowering friction loss of journal bearings. In the current work, placing textures downstream of the high-pressure region leads to a considerable reduction in friction loss, with a slight increase in load-carrying capacity.

Under the mixed lubrication condition, the effect of textures on the load-carrying capacity remains consistent with that under the hydrodynamic lubrication condition. This effect is governed by a balance between the micro-hydrodynamic effect and the interference effect on the high-pressure region. The friction loss under the mixed lubrication is governed by both fluid shear stress and asperity contact. Under the mixed lubrication condition in this work, the effect of textures on the friction loss due to the asperity contact is dominating. Both positive and negative effects of textures on fluid shear stress become less significant compared to those under the hydrodynamic lubrication condition. From the mechanism analysis on the friction loss due to the asperity contact, textures can reduce the asperity shear stress by increasing film thickness or reducing the contact area. In contrast, textures may also increase asperity shear stress when the film thickness is reduced. When textures are located downstream of the load-carrying region, they can slightly increase load-carrying capacity while simultaneously reducing the asperity contact area. In contrast, improper texture design parameters can result in the friction loss increasing up to five times higher than that of the non-textured bearing.

**(b) ML-based surrogate model, which can efficiently predict the load-carrying capacity and friction loss with the consideration of interactions between texture design parameters:**

For the second research need, ML-based surrogate models based on the artificial neural network (ANN) algorithm are developed to efficiently predict the minimum film thickness and the friction loss. To develop the ANN models, the texture design parameters, including the texture geometry and distribution parameters, are identified as input parameters. The minimum film thickness and friction loss are defined as output parameters. A total of 220 training datasets is generated through the mixed-EHL model. To improve the prediction accuracy of the surrogate models using the

given datasets, the cross-validation-based hyperparameter optimization is employed to design the neural network architecture, and the genetic algorithm is applied to determine the optimal initial weights and biases.

Both the prediction accuracy and efficiency of the developed ML-based surrogate models are evaluated. Regarding the prediction accuracy, the average accuracy stands over 97% while the prediction error remains consistently below 9% for both the hydrodynamic and mixed lubrication conditions. In terms of the prediction efficiency, the trained surrogate models can predict the friction loss and the minimum film thickness of textured journal bearings within 1 second for each case. This demonstrates both the accuracy and efficiency of the surrogate models.

**(c) Multi-objective optimization model, which can optimize texture parameters with the aim of reducing the friction losses and increasing the load-carrying capacity.**

Based on the ML-based surrogate models, the optimization design of textured journal bearings can be further conducted to address the third research need. The multi-objective optimization model is developed based on the Non-Dominated Sorting Genetic Algorithm-II (NSGA-II). The design parameters include the texture geometry parameters (texture width ratio, texture depth ratio) and texture distribution parameters (starting angle of textured area, texture coverage angle). The targets of the optimization are a higher minimum film thickness and a lower friction loss.

The optimization of texture design parameters is conducted for both hydrodynamic and mixed lubrication conditions. The optimized texture parameters for both conditions show similar results on the texture width ratio but significant difference in the texture depth ratio and texture distribution. Compared to the optimized results for the hydrodynamic lubrication, the optimal texture depth ratio is lower and the optimal texture distribution shifts upstream for the mixed lubrication. This indicates that an efficient design optimization obviously depends on the specific operating condition. With the optimized texture design parameters, the minimum film thickness is increased by 1.46% while the friction loss is reduced by approximately 11.97% under the hydrodynamic lubrication condition in this work. For the mixed lubrication case in this work, the friction loss of the optimized textured bearing decreases by 10.39%, and the minimum film thickness increases by 1.38%. These results demonstrate the significant potential of surface textures to increase the energy efficiency of journal bearings in practical applications.

Eventually, the results demonstrate that an integration of the above three sub-models can provide a comprehensive strategy for designing surface textures in journal

bearings. In addition, the N-S based mixed-EHL model developed within this strategy can offer in-depth insights into textured journal bearings, as all the texture-induced microflow effects can be accurately captured.

## 9.2. Outlook

Although the proposed design strategy demonstrates a promising ability to improve the load-carrying capacity and reduce the friction loss of journal bearings in this work, there are still aspects that are worth investigating in future work.

First of all, this work conducts the first step in developing an N-S based mixed-EHL model. Although the current model demonstrates satisfactory results, the numerical model can be further extended to incorporate more factors in future work, such as temperature and real surface roughness. This extension would make the model applicable to a broader range of operating conditions for journal bearings.

Secondly, the optimization strategy in this work indicates promising results for enhancing the performance of textured journal bearings. In the current optimization, the texture distribution along the axial direction (i.e. bearing width) is fixed to a linear pattern. In addition, all textures have the same size. Considering the nonuniform distribution of the bearing's load-carrying region, a more flexible texture distribution and multi-scale textures can be considered in future work.

Thirdly, the optimization of textured journal bearings is limited to a static operating condition, including the constant external load and rotational speed. Considering the variation of operating conditions in real applications, such as wind turbines, the optimization design should be improved to cooperate with time-dependent operating conditions and identify the texture parameters which are beneficial throughout the entire operating period.

## 10. Appendix

### 10.1. Governing equations of cavitation

In this work, the cavitation effect is considered using the homogeneous equilibrium model, which assumes the mixture of liquid and vapor to be in a mechanical and thermodynamic equilibrium [171]. To consider the compressibility of the mixture flow, the cavitation model is based on the relations of the pressure and density as a closure equation, which is employed by the following equation [171]:

$$\frac{D\rho_m}{Dt} = \Psi_m \frac{Dp}{Dt} \quad (\text{A1})$$

where  $\rho_m$  is the density of the mixture of liquid and vapour;  $\Psi_m$  is the compressibility coefficient of the mixture; and  $p$  is the pressure.

Then, the mass fraction of vapor  $\gamma$  is calculated by the following equation [171]:

$$\gamma = \frac{\rho_m - \rho_{l,sat}}{\rho_{v,sat} - \rho_{l,sat}} \quad (\text{A2})$$

where  $\rho_{l,sat}$  and  $\rho_{v,sat}$  are density of the liquid and vapor at saturation pressure, respectively.

Subsequently, the mixture compressibility  $\Psi_m$  obtained by the Wallis linear model [172] and the local mixture viscosity  $\eta_m$  are computed by:

$$\Psi_m = \gamma\Psi_v + (1 - \gamma)\Psi_l \quad (\text{A3})$$

$$\eta_m = \gamma\eta_v + (1 - \gamma)\eta_l \quad (\text{A4})$$

where  $\Psi_l$  and  $\Psi_v$  are the compressibility of liquid and vapor;  $\eta_l$  and  $\eta_v$  are the viscosity of liquid and vapor.

Next, the mixture density  $\rho_m$  can be calculated by considering the fraction of vapor. The mixture's equilibrium equation of state is following [171]:

$$\rho_m = (1 - \gamma)\rho_l^0 + (\gamma\Psi_v + (1 - \gamma)\Psi_l)P_{sat} + \Psi_m(P - P_{sat}) \quad (\text{A5})$$

where  $\rho_l^0$  is the density of liquid at reference pressure;  $P_{sat}$  is the saturation pressure

### 10.2. Governing equations of deformation

According to the Boussinesq's integral EHS method, the total elastic radial deformation  $d(\theta, z)$  is induced by the pressure field from the fluid domain  $p(\theta, z)$

[133]. Therefore, the deformation of any point can be obtained through displacement-pressure relationship, as shown in the following equation [133]:

$$\begin{aligned}
 d(\theta', z') &= d_1 + d_2 \\
 &= \frac{(1 - \nu_2^2)}{\pi E_2} \iint_{\Omega} \frac{p(\theta, z)}{\sqrt{((\theta' - \theta)R)^2 + (z' - z)^2}} d\theta dz \\
 &\quad + \frac{(1 - \nu_2^2)}{\pi E_2} \iint_{\Omega} \frac{p(\theta, z)}{\sqrt{((\theta' - \theta)R)^2 + (z' - z)^2}} d\theta dz \quad (A6) \\
 &= \left[ \frac{(1 - \nu_1^2)}{\pi E_1} + \frac{(1 - \nu_2^2)}{\pi E_2} \right] \iint_{\Omega} \frac{p(\theta, z)}{\sqrt{((\theta' - \theta)R)^2 + (z' - z)^2}} d\theta dz
 \end{aligned}$$

Combining Eq. (A6) and Eq. (5-6), this deformation-pressure relationship is derived as:

$$d(\theta', z') = \frac{1}{\pi E^*} \iint_{\Omega} \frac{p(\theta, z)}{\sqrt{((\theta' - \theta)R)^2 + (z' - z)^2}} d\theta dz \quad (A7)$$

### 10.3. Governing equations of surface roughness

(a) Determination of  $K$  in Eq. (5-8)

The elastic factor  $K$  is a function which combined roughness parameters of the contacting bodies:

$$K = \frac{16 \cdot \sqrt{2} \cdot \pi}{15} (\sigma_s \cdot \bar{\beta}_s \cdot \zeta_s)^2 \cdot \sqrt{\frac{\sigma_s}{\beta}} \quad (A8)$$

where,  $\bar{\beta}_s$  and  $\zeta_s$  represent the mean summit radius and the summit density. In engineering practice, the recommended values for  $\sigma_s \bar{\beta}_s \zeta_s$  and  $\sigma_s / \bar{\beta}_s$  are typically adopted. From Greenwood and Tripp [135], the value of  $\sigma_s \bar{\beta}_s \zeta_s$  typically ranges from 0.03 to 0.08. The value of  $\sigma_s / \bar{\beta}_s$  is recommended to vary between 0.0001 and 0.1 [136,173]. In general, the elasticity factor  $K$  describes the slope of the contact pressure curve. A recommended range for journal bearings is 0.0003-0.003. In this dissertation, an elastic factor of  $K=0.001$  is selected according to the work from Sander et al. [28,147].

(b) Determination of  $A$  and  $Re_k$  in Eq. (5-11)

In this roughness-viscosity model, the effect of surface roughness on the fluid flow is considered by an additional viscosity  $\eta_s$ , which is calculated by Eq. (5-11). To calculate  $\eta_s$ ,  $A$  is a coefficient factor that can be determined [142, 144]. In this model:

$$A = 0.1306 \left( \frac{C}{2R_q} \right)^{0.3693} \cdot \exp \left[ Re \left( 6 \cdot 10^{-5} \cdot \frac{C}{2R_q} - 0.0029 \right) \right] \quad (A9)$$

Besides,  $Re_k$  is the roughness Reynolds number at surfaces of shaft and bearing, and it is obtained through the following equation [142, 144]:

$$Re_k = \frac{\rho_l R_q^2}{\eta_l} \cdot \left( \frac{dU_m}{d\vec{n}} \right) \quad (A10)$$

where  $\vec{n}$  is the normal distance to the wall.



---

## 11. References

1. Holmberg, K.; Erdemir, A. Influence of tribology on global energy consumption, costs and emissions. *Friction* **2017**, *5*, 263–284, doi:10.1007/s40544-017-0183-5.
2. Holmberg, K.; Kivikytö-Reponen, P.; Härkisaari, P.; Valtonen, K.; Erdemir, A. Global energy consumption due to friction and wear in the mining industry. *Tribology International* **2017**, *115*, 116–139, doi:10.1016/j.triboint.2017.05.010.
3. Profito, F.J.; Vladescu, S.C.; Reddyhoff, T.; Dini, D. Numerical and experimental investigation of textured journal bearings for friction reduction. *Tribology International* **2024**, *195*, 109643, doi:10.1016/j.triboint.2024.109643.
4. Bouyer, J.; Fillon, M. Experimental measurement of the friction torque on hydrodynamic plain journal bearings during start-up. *Tribology International* **2011**, *44*, 772–781, doi:10.1016/j.triboint.2011.01.008.
5. Hirani, H.; Suh, N.P. Journal bearing design using multiobjective genetic algorithm and axiomatic design approaches. *Tribology International* **2005**, *38*, 481–491, doi:10.1016/j.triboint.2004.10.008.
6. Ghani, S.N.; Alithari, A.S.; Hasan, H.S. A review: Enhancing tribological properties of journal bearings composite materials. *Open Engineering* **2024**, *14*, doi:10.1515/eng-2024-0047.
7. König, F.; Sous, C.; Jacobs, G. Numerical prediction of the frictional losses in sliding bearings during start-stop operation. *Friction* **2021**, *9*, 583–597, doi:10.1007/s40544-020-0417-9.
8. Shinde, A.B.; Pawar, P.M. Multi-objective optimization of surface textured journal bearing by Taguchi based Grey relational analysis. *Tribology International* **2017**, *114*, 349–357, doi:10.1016/j.triboint.2017.04.041.
9. Rosenkranz, A.; Grützmacher, P.G.; Gachot, C.; Costa, H.L. Surface texturing in machine elements – A critical discussion for rolling and sliding contacts. *Adv Eng Mater* **2019**, *21*, doi:10.1002/adem.201900194.
10. Etsion, I. State of the art in laser surface texturing. *Journal of Tribology* **2005**, *127*, 248–253, doi:10.1115/1.1828070.
11. Gropper, D.; Wang, L.; Harvey, T.J. Hydrodynamic lubrication of textured surfaces: A review of modeling techniques and key findings. *Tribology International* **2016**, *94*, 509–529, doi:10.1016/j.triboint.2015.10.009.
12. Arslan, A.; Masjuki, H.H.; Kalam, M.A.; Varman, M.; Mufti, R.A.; Mosarof, M.H.; Khuong, L.S.; Quazi, M.M. Surface texture manufacturing techniques and tribological effect of surface texturing on cutting tool performance: A

- review. *Critical Reviews in Solid State and Materials Sciences* **2016**, *41*, 447–481, doi:10.1080/10408436.2016.1186597.
13. Gachot, C.; Rosenkranz, A.; Hsu, S.M.; Costa, H.L. A critical assessment of surface texturing for friction and wear improvement. *Wear* **2017**, *372-373*, 21–41, doi:10.1016/j.wear.2016.11.020.
  14. König, F.; Rosenkranz, A.; Grützmacher, P.G.; Mücklich, F.; Jacobs, G. Effect of single- and multi-scale surface patterns on the frictional performance of journal bearings – A numerical study. *Tribology International* **2020**, *143*, 106041, doi:10.1016/j.triboint.2019.106041.
  15. Costa, H.L.; Im Hutchings. Some innovative surface texturing techniques for tribological purposes. *Proceedings of the Institution of Mechanical Engineers, Part J: Journal of Engineering Tribology* **2015**, *229*, 429–448, doi:10.1177/1350650114539936.
  16. Wang, Y.; Jacobs, G.; König, F.; Zhang, S.; Goedel, S. von. Investigation of microflow effects in textures on hydrodynamic performance of journal bearings using CFD simulations. *Lubricants* **2023**, *11*, 20, doi:10.3390/lubricants11010020.
  17. Galda, L.; Sep, J.; Olszewski, A.; Zochowski, T. Experimental investigation into surface texture effect on journal bearings performance. *Tribology International* **2019**, *136*, 372–384, doi:10.1016/j.triboint.2019.03.073.
  18. Xie, Z.; Zhang, Y.; Zhou, J.; Zhu, W. Theoretical and experimental research on the micro interface lubrication regime of water lubricated bearing. *Mechanical Systems and Signal Processing* **2021**, *151*, 107422, doi:10.1016/j.ymsp.2020.107422.
  19. Lu, X.; Khonsari, M.M. An experimental investigation of dimple effect on the Stribeck curve of journal bearings. *Tribology Letters* **2007**, *27*, doi:10.1007/s11249-007-9217-x.
  20. Fowell, M.T.; Medina, S.; Olver, A.V.; Spikes, H.A.; Pegg, I.G. Parametric study of texturing in convergent bearings. *Tribology International* **2012**, *52*, 7–16, doi:10.1016/j.triboint.2012.02.013.
  21. Tala-Ighil, N.; Fillon, M.; Maspeyrot, P. Effect of textured area on the performances of a hydrodynamic journal bearing. *Tribology International* **2011**, *44*, 211–219, doi:10.1016/j.triboint.2010.10.003.
  22. Tala-Ighil, N.; Maspeyrot, P.; Fillon, M.; Bounif, A. Effects of surface texture on journal-bearing characteristics under steady-state operating conditions. *Proceedings of the Institution of Mechanical Engineers, Part J: Journal of Engineering Tribology* **2007**, *221*, 623–633, doi:10.1243/13506501JET287.
  23. GfT-Arbeitsblatt 7: Verschleiß, Reibung; Definitionen, Begriffe, Prüfung, Gesellschaft für Tribologie, 2002.

- 
24. Florian König. Wear prediction of plain bearings under mixed friction conditions. Doctoral Thesis, Aachen, 2020.
  25. Jacobs, G.; Plogmann, M. *Tribology*; Druck & Verlagshaus Mainz: Aachen, 2017.
  26. Wen, S.; Huang, P. *Principles of tribology (second edition): Mo ca xue yuan li (di 2 ban) / Wen Shizhu, Huang Ping zhu*, Di 1 ban; Qing hua da xue chu ban she: Beijing, 2017, ISBN 978-7-302-48526-1.
  27. Lu, X.; Khonsari, M.M.; Gelinck, E.R.M. The Stribeck curve: Experimental results and theoretical prediction. *Journal of Tribology* **2006**, *128*, 789–794, doi:10.1115/1.2345406.
  28. Sander, D.E. A validated elasto-hydrodynamic simulation for journal bearings operating under severe conditions. Doctoral Thesis, Austria, 2016.
  29. Fowell, M.; Olver, A.V.; Gosman, A.D.; Spikes, H.A.; Pegg, I. Entrainment and inlet suction: Two mechanisms of hydrodynamic lubrication in textured bearings. *Journal of Tribology* **2007**, *129*, 336–347, doi:10.1115/1.2540089.
  30. Olver, A.V.; Fowell, M.T.; Spikes, H.A.; Pegg, I.G. ‘Inlet suction’, a load support mechanism in non-convergent, pocketed, hydrodynamic bearings. *Proceedings of the Institution of Mechanical Engineers, Part J: Journal of Engineering Tribology* **2006**, *220*, 105–108, doi:10.1243/13506501JET168.
  31. Yagi, K.; Sugimura, J. Balancing wedge action: A contribution of textured surface to hydrodynamic pressure generation. *Tribol Lett* **2013**, *50*, 349–364, doi:10.1007/s11249-013-0132-z.
  32. Hamilton, D.B.; Walowit, J.A.; Allen, C.M. A theory of lubrication by microirregularities. *Journal of Basic Engineering* **1966**, *88*, 177–185, doi:10.1115/1.3645799.
  33. Etsion, I.; Kligerman, Y.; Halperin, G. Analytical and experimental investigation of laser-textured mechanical seal faces. *Tribology Transactions* **1999**, *42*, 511–516, doi:10.1080/10402009908982248.
  34. Miyanaga, N.; Miwa, R.; Ishii, R.; Khonsari, M. On the measurement of pressure in textured dimples. *Tribology International* **2025**, *209*, 110719, doi:10.1016/j.triboint.2025.110719.
  35. Qiu, Y.; Khonsari, M.M. On the prediction of cavitation in dimples using a mass-conservative algorithm. *Journal of Tribology* **2009**, *131*, doi:10.1115/1.3176994.
  36. Ausas, R.; Ragot, P.; Leiva, J.; Jai, M.; Bayada, G.; Buscaglia, G.C. The impact of the cavitation model in the analysis of microtextured lubricated journal bearings. *Journal of Tribology* **2007**, *129*, 868–875, doi:10.1115/1.2768088.
-

37. Salem, E.A.; Shawky, M. Lubricant inertia effects in externally pressurized rectangular gas bearings. *Wear* **1979**, *54*, 201–209, doi:10.1016/0043-1648(79)90114-5.
38. Syed, I.; Sarangi, M. Hydrodynamic lubrication with deterministic micro textures considering fluid inertia effect. *Tribology International* **2014**, *69*, 30–38, doi:10.1016/j.triboint.2013.08.011.
39. Ma, X.; Meng, X.; Wang, Y.; Liang, Y.; Peng, X. Fluid inertia effect on spiral-grooved mechanical face seals considering cavitation effects. *Tribology Transactions* **2021**, *64*, 367–380, doi:10.1080/10402004.2020.1846829.
40. Dobrica, M.B.; Fillon, M. About the validity of Reynolds equation and inertia effects in textured sliders of infinite width. *Proceedings of the Institution of Mechanical Engineers, Part J: Journal of Engineering Tribology* **2009**, *223*, 69–78, doi:10.1243/13506501JET433.
41. Arghir, M.; Roucou, N.; Helene, M.; Frene, J. Theoretical analysis of the incompressible laminar flow in a macro-roughness cell. *Journal of Tribology* **2003**, *125*, 309–318, doi:10.1115/1.1506328.
42. Sahlin, F.; Glavatskih, S.B.; Almqvist, T.; Larsson, R. Two-dimensional CFD-analysis of micro-patterned surfaces in hydrodynamic lubrication. *Journal of Tribology* **2005**, *127*, 96–102, doi:10.1115/1.1828067.
43. Hilmy, F.; Muchammad, M.; Tauviquirrahman, M.; Jamari, J. Inertia effect of textured lubricated contact on the bearing performance using CFD approach. *J. Phys.: Conf. Ser.* **2018**, *1090*, 12041, doi:10.1088/1742-6596/1090/1/012041.
44. Shankar, P.N.; Deshpande, M.D. Fluid mechanics in the driven cavity. *Annu. Rev. Fluid Mech.* **2000**, *32*, 93–136, doi:10.1146/annurev.fluid.32.1.93.
45. Meng, F.M.; Yang, T. Preliminary study on mechanism of cavitation in lubricant of textured sliding bearing. *Proceedings of the Institution of Mechanical Engineers, Part J: Journal of Engineering Tribology* **2013**, *227*, 695–708, doi:10.1177/1350650112468560.
46. Wang, W.; He, Y.; Zhao, J.; Li, Y.; Luo, J. Numerical optimization of the groove texture bottom profile for thrust bearings. *Tribology International* **2017**, *109*, 69–77, doi:10.1016/j.triboint.2016.12.006.
47. Wang, W.; He, Y.; Li, Y.; Wei, B.; Hu, Y.; Luo, J. Investigation on inner flow field characteristics of groove textures in fully lubricated thrust bearings. *Industrial Lubrication and Tribology* **2018**, *70*, 754–763, doi:10.1108/ILT-08-2017-0224.
48. Xie, Z.; Li, J.; Tian, Y.; Du, P.; Zhao, B.; Xu, F. Theoretical and experimental study on influences of surface texture on lubrication performance of a novel bearing. *Tribology International* **2024**, *193*, 109351, doi:10.1016/j.triboint.2024.109351.

- 
49. Li, J.; Chen, H. Evaluation on applicability of Reynolds equation for squared transverse roughness compared to CFD. *Journal of Tribology* **2007**, *129*, 963–967, doi:10.1115/1.2768619.
  50. Dobrica, M.B.; Fillon, M.; Pascovici, M.D.; Cicone, T. Optimizing surface texture for hydrodynamic lubricated contacts using a mass-conserving numerical approach. *Proceedings of the Institution of Mechanical Engineers, Part J: Journal of Engineering Tribology* **2010**, *224*, 737–750, doi:10.1243/13506501JET673.
  51. Wang, J.; Yan, Z.; Fang, X.; Shen, Z.; Pan, X. Observation and experimental investigation on cavitation effect of friction pair surface texture. *Lubr. Sci.* **2020**, *32*, 404–414, doi:10.1002/lr.1520.
  52. Das, D.; Kakoty, S.K. Effect of lubricant inertia on textured journal bearing implementing mass conserving (JFO) boundary conditions. *ILT* **2024**, *76*, 1186–1196, doi:10.1108/ILT-07-2024-0276.
  53. Taylor, C.; Hood, P. A numerical solution of the Navier-Stokes equations using the finite element technique. *Computers & Fluids* **1973**, *1*, 73–100, doi:10.1016/0045-7930(73)90027-3.
  54. Lintermann, A. Computational meshing for CFD simulations, **2021**, 85–115, doi:10.1007/978-981-15-6716-2\_6.
  55. Wen, C.; Meng, X.; Li, W. Numerical analysis of textured piston compression ring conjunction using two-dimensional-computational fluid dynamics and Reynolds methods. *Proceedings of the Institution of Mechanical Engineers, Part J: Journal of Engineering Tribology* **2018**, *232*, 1467–1485, doi:10.1177/1350650118755248.
  56. Vilhena, L.; Sedlaček, M.; Podgornik, B.; Rek, Z.; Žun, I. CFD modeling of the effect of different surface texturing geometries on the frictional behavior. *Lubricants* **2018**, *6*, 15, doi:10.3390/lubricants6010015.
  57. Keller, D.; Jacobs, G.; Neumann, S. Development of a low-friction radial shaft seal: using CFD simulations to optimise the microstructured sealing lip. *Lubricants* **2020**, *8*, 41, doi:10.3390/lubricants8040041.
  58. Wang, H.; Lin, N.; Yuan, S.; Liu, Z.; Yu, Y.; Zeng, Q.; Li, D.; Fan, J.; Wu, Y. Numerical simulation on hydrodynamic lubrication performance of bionic multi-scale composite textures inspired by surface patterns of subcrenata and clam shells. *Tribology International* **2023**, *181*, 108335, doi:10.1016/j.triboint.2023.108335.
  59. Cohen, I.; Goltsberg, R. Partial surface texturing in hydrodynamic lubrication: A CFD-based investigation. *Lubricants* **2023**, *11*, 395, doi:10.3390/lubricants11090395.
-

60. Wang, Y.; Jacobs, G.; Zhang, S.; Klinghart, B.; König, F. Lubrication mechanism analysis of textures in journal bearings using CFD simulations. *Industrial Lubrication and Tribology* **2025**, *77*, 2–14, doi:10.1108/ILT-01-2024-0031.
61. Sawicki, J.; Rao, T. Cavitation effects on the stability of a submerged journal bearing. *The International Journal of Rotating Machinery* **2004**, *10*, 227–232, doi:10.1080/10236210490426370.
62. Grando, F.P.; Priest, M.; Prata, A.T. A two-phase flow approach to cavitation modelling in journal bearings. *Tribol Lett* **2006**, *21*, 233–244, doi:10.1007/s11249-006-9027-6.
63. Marian, M.; Almqvist, A.; Rosenkranz, A.; Fillon, M. Numerical micro-texture optimization for lubricated contacts—A critical discussion. *Friction* **2022**, *10*, 1772–1809, doi:10.1007/s40544-022-0609-6.
64. Wang, Y.; Jacobs, G.; Zhang, S.; Klinghart, B.; König, F. Development of a machine learning-based surrogate model for friction prediction in textured journal bearings. *Friction* **2024**, doi:10.26599/FRICT.2025.9441051.
65. Xiang, G.; Han, Y.; Wang, J.; Wang, J.; Ni, X. Coupling transient mixed lubrication and wear for journal bearing modeling. *Tribology International* **2019**, *138*, 1–15, doi:10.1016/j.triboint.2019.05.011.
66. Zhang, Y.; Chen, G.; Wang, L. Effects of thermal and elastic deformations on lubricating properties of the textured journal bearing. *Advances in Mechanical Engineering* **2019**, *11*, 168781401988379, doi:10.1177/1687814019883790.
67. Han, J.; Fang, L.; Sun, J.; Ge, S. Hydrodynamic lubrication of microdimple textured surface using three-dimensional CFD. *Tribology Transactions* **2010**, *53*, 860–870, doi:10.1080/10402004.2010.496070.
68. Liang, X.; Liu, Z.; Wang, H.; Zhou, X.; Zhou, X. Hydrodynamic lubrication of partial textured sliding journal bearing based on three-dimensional CFD. *Industrial Lubrication and Tribology* **2016**, *68*, 106–115, doi:10.1108/ILT-04-2015-0055.
69. Cupillard, S.; Glavatskih, S.; Cervantes, M.J. Computational fluid dynamics analysis of a journal bearing with surface texturing. *Proceedings of the Institution of Mechanical Engineers, Part J: Journal of Engineering Tribology* **2008**, *222*, 97–107, doi:10.1243/13506501JET319.
70. Kumar, M.; Singh, S. Parametric study of textured hydrodynamic journal bearing for turbulent flow using CFD analysis. *Int J Interact Des Manuf* **2025**, *19*, 2987–2997, doi:10.1007/s12008-024-02147-9.
71. Nie, T.; Yang, K.; Zhou, L.; Wu, X.; Wang, Y. CFD analysis of load capacity of journal bearing with surface texture. *Energy Reports* **2022**, *8*, 327–334, doi:10.1016/j.egy.2022.05.073.

- 
72. Meng, F.M.; Zhang, L.; Liu, Y.; Li, T.T. Effect of compound dimple on tribological performances of journal bearing. *Tribology International* **2015**, *91*, 99–110, doi:10.1016/j.triboint.2015.06.030.
  73. Tauviqirrahman, M.; Jamari, J.; Bagir, M.; Caesarendra, W.; Paryanto, P. Elastohydrodynamic behavior analysis on water-lubricated journal bearing: a study of acoustic and tribological performance based on CFD-FSI approach. *J Braz. Soc. Mech. Sci. Eng.* **2022**, *44*, doi:10.1007/s40430-021-03314-9.
  74. Hameed, M.R.; Ali, S.A.; Hadwan, H.H.; Toman, A.A.; Mahdi, M.A. CFD-FSI analysis of textured journal bearing working with nano lubricant. *Diagnostyka* **2024**, *25*, 1–10, doi:10.29354/diag/188391.
  75. Lin, Q.; Bao, Q.; Li, K.; Khonsari, M.M.; Zhao, H. An investigation into the transient behavior of journal bearing with surface texture based on fluid-structure interaction approach. *Tribology International* **2018**, *118*, 246–255, doi:10.1016/j.triboint.2017.09.026.
  76. Muchammad, M.; Tauviqirrahman, M.; Rizki, Y.M.; Syafaat, I.; Maharani, F.; Ammarullah, M.I. Elastohydrodynamic analysis of multistep texture effects and partial surface roughness on the tribological performance of steel journal bearings. *Discov Appl Sci* **2025**, *7*, doi:10.1007/s42452-025-06789-6.
  77. Sharma, S.; Jamwal, G.; Awasthi, R.K. Enhancement of steady state performance of hydrodynamic journal bearing using chevron-shaped surface texture. *Proceedings of the Institution of Mechanical Engineers, Part J: Journal of Engineering Tribology* **2019**, *233*, 1833–1843, doi:10.1177/1350650119847369.
  78. Zhang, H.; Dong, G.; Hua, M.; Guo, F.; Chin, K.S. Parametric design of surface textures on journal bearing. *Industrial Lubrication and Tribology* **2015**, *67*, 359–369, doi:10.1108/ILT-08-2013-0089.
  79. Guo, B. Optimal surface texture design of journal bearing with axial grooves. *IJHT* **2017**, *35*, 267–272, doi:10.18280/ijht.350206.
  80. Sharma, S.; Jamwal, G.; Awasthi, R.K. Numerical study on steady state performance enhancement of partial textured hydrodynamic journal bearing. *ILT* **2019**, *71*, 1055–1063, doi:10.1108/ILT-03-2019-0083.
  81. Mehrjardi, M.Z.; Shooroki, A.R.; Rabani, M.; Rabani, M. Effect of surface texture depth with various geometric shapes on the steady-state performance and dynamic stability of noncircular lobed journal bearings. *Applied Sciences* **2025**, *15*, 4412, doi:10.3390/app15084412.
  82. Mao, Y.; Li, D.; Li, L.; Zheng, J. Effect of textured parameters on tribological properties of hydrodynamic journal bearing. *ILT* **2024**, *76*, 102–109, doi:10.1108/ILT-09-2023-0305.
-

83. Brizmer, V.; Kligerman, Y. A laser surface textured journal bearing. *Journal of Tribology* **2012**, *134*, doi:10.1115/1.4006511.
84. Tala-Ighil, N.; Maspeyrot P.; Fillon, M.; Bounif, A. Hydrodynamic effects of texture geometries on journal bearing surfaces. **2007**, In International Conference on Tribology, Bucharest, Romania.
85. Lu, P.; Wood, R.; Gee, M.; Wang, L.; Pfleging, W. The friction reducing effect of square-shaped surface textures under lubricated line-contacts—An experimental study. *Lubricants* **2016**, *4*, 26, doi:10.3390/lubricants4030026.
86. Shen, C.; Khonsari, M.M. Numerical optimization of texture shape for parallel surfaces under unidirectional and bidirectional sliding. *Tribology International* **2015**, *82*, 1–11, doi:10.1016/j.triboint.2014.09.022.
87. Vencl, A.; Ivanović, L.; Stojanović, B.; Zadorozhnaya, E.; Miladinović, S.; Svoboda, P. Surface texturing for tribological applications: A review. *PES* **2019**, *1*, 227–239, doi:10.24874/PES01.01.029.
88. Putignano, C.; Parente, G.; Profito, F.J.; Gaudiuso, C.; Ancona, A.; Carbone, G. Laser microtextured surfaces for friction reduction: Does the pattern matter? *Materials (Basel)* **2020**, *13*, doi:10.3390/ma13214915.
89. Arif, M.; Shukla, D.K.; Kango, S.; Sharma, N. Implication of surface texture and slip on hydrodynamic fluid film bearings: A comprehensive survey. *Tribology Online* **2020**, *20 // 15*, 1–25, doi:10.2474/trol.15.265.
90. Khatri, C.B.; Sharma, S.C. Influence of textured surface on the performance of non-recessed hybrid journal bearing operating with non-Newtonian lubricant. *Tribology International* **2016**, *95*, 221–235, doi:10.1016/j.triboint.2015.11.017.
91. Kango, S.; Sharma, R.K.; Pandey, R.K. Comparative analysis of textured and grooved hydrodynamic journal bearing. *Proceedings of the Institution of Mechanical Engineers, Part J: Journal of Engineering Tribology* **2014**, *228*, 82–95, doi:10.1177/1350650113499742.
92. Gui, C.; Meng, F. Comparative study of spherical dimple and bump effects on the tribological performances of journal bearing. *Proceedings of the Institution of Mechanical Engineers, Part J: Journal of Engineering Tribology* **2019**, *233*, 139–157, doi:10.1177/1350650118770355.
93. Kango, S.; Singh, D.; Sharma, R.K. Numerical investigation on the influence of surface texture on the performance of hydrodynamic journal bearing. *Meccanica* **2012**, *47*, 469–482, doi:10.1007/s11012-011-9460-y.
94. Angione, C.; Silverman, E.; Yaneske, E. Using machine learning as a surrogate model for agent-based simulations. *PLoS One* **2022**, *17*, e0263150, doi:10.1371/journal.pone.0263150.
95. Aderyani, F.R.; Jafarzadegan, K.; Moradkhani, H. A surrogate machine learning modeling approach for enhancing the efficiency of urban flood

- modeling at metropolitan scales. *Sustainable Cities and Society* **2025**, *123*, 106277, doi:10.1016/j.scs.2025.106277.
96. Marian, M.; Tremmel, S. Current trends and applications of machine learning in tribology—A review. *Lubricants* **2021**, *9*, 86, doi:10.3390/lubricants9090086.
  97. König, F.; Wirsing, F.; Singh, A.; Jacobs, G. Machine-learning-based wear prediction in journal bearings under start–stop conditions. *Lubricants* **2024**, *12*, 290, doi:10.3390/lubricants12080290.
  98. Moschopoulos, M.; Rossopoulos, G.N.; Papadopoulos, C.I. Journal bearing performance prediction using machine learning and octave-band signal analysis of sound and vibration measurements. *Polish Maritime Research* **2021**, *28*, 137–149, doi:10.2478/pomr-2021-0041.
  99. Hess, N.; Shang, L. Machine learning prediction of journal bearing pressure distributions, considering elastic deformation and cavitation. *Fluid Power Systems Technology* **2021**, doi:10.1115/FPMC2021-68483.
  100. Baş, H.; Karabacak, Y.E. Machine learning-based prediction of friction torque and friction coefficient in statically loaded radial journal bearings. *Tribology International* **2023**, *186*, 108592, doi:10.1016/j.triboint.2023.108592.
  101. Otero, J.E.; Ochoa, E.D.L.G.; Vallinot, I.B.; Tanarro, E.C. Optimising the design of textured surfaces for reducing lubricated friction coefficient. *Lubrication Science* **2017**, *29*, 183–199, doi:10.1002/lis.1363.
  102. Marian, M.; Grützmaier, P.; Rosenkranz, A.; Tremmel, S.; Mücklich, F.; Wartzack, S. Designing surface textures for EHL point-contacts - Transient 3D simulations, meta-modeling and experimental validation. *Tribology International* **2019**, *137*, 152–163, doi:10.1016/j.triboint.2019.03.052.
  103. Li, Z.; Li, J.; An, B.; Li, R. The design method for surface texture of sliding friction pairs based on machine learning under mixed lubrication. *Tribology International* **2024**, *194*, 109563, doi:10.1016/j.triboint.2024.109563.
  104. Budach, L.; Feuerpfeil, M.; Ihde, N.; Nathansen, A.; Noack, N.; Patzlaff, H.; Naumann, F.; Harmouch, H. The effects of data quality on machine learning performance. *Proceedings of the VLDB Endowment* **2022**, *15*, ISSN 2150-8097, doi:10.48550/arXiv.2207.14529.
  105. Chen, H.; Chen, J.; Ding, J. Data evaluation and enhancement for quality improvement of machine learning. *IEEE Transactions on Reliability* **2021**, *70*, 831–847, doi:10.1109/TR.2021.3070863.
  106. Singh, N.; Awasthi, R.K. Influence of texture geometries on the performance parameters of hydrodynamic journal bearing. *Proceedings of the Institution of Mechanical Engineers, Part J: Journal of Engineering Tribology* **2021**, *235*, 2056–2072, doi:10.1177/1350650120982691.

107. Guo, B. Optimal surface texture design of journal bearing with axial grooves. *IJHT* **2017**, *35*, 267–272, doi:10.18280/ijht.350206.
108. Shinde, A.B.; Pawar, P.M.; Ronge, B.P.; Bhuse, P.K.; Parkhe, A.K.; Jadhav, P.V. Optimization of multiple performance characteristics of surface micro-textured journal bearing, **2020**, 377–389, doi:10.1007/978-3-030-16962-6\_39.
109. Lin, Q.; Bao, Q.; Li, K.; Khonsari, M.M.; Zhao, H. An investigation into the transient behavior of journal bearing with surface texture based on fluid-structure interaction approach. *Tribology International* **2018**, *118*, 246–255, doi:10.1016/j.triboint.2017.09.026.
110. Antony, J. *Design of Experiments for Engineers and Scientists*; Elsevier, 2014.
111. Vagaská, A.; Gombár, M.; Straka, E. Selected mathematical optimization methods for solving problems of engineering practice. *Energies* **2022**, *15*, 2205, doi:10.3390/en15062205.
112. Beg, A.H.; Islam, M.Z. Advantages and limitations of genetic algorithms for clustering records, **2016**, 2478–2483, doi:10.1109/ICIEA.2016.7604009.
113. Gallagher, K.; Sambridge, M. Genetic algorithms: A powerful tool for large-scale nonlinear optimization problems. *Computers & Geosciences* **1994**, *20*, 1229–1236, doi:10.1016/0098-3004(94)90072-8.
114. Zhang, H.; Hafezi, M.; Dong, G.; Liu, Y. A design of coverage area for textured surface of sliding journal bearing based on genetic algorithm. *Journal of Tribology* **2018**, *140*, doi:10.1115/1.4039958.
115. Zhang, H.; Liu, Y.; Hua, M.; Zhang, D.; Qin, L.; Dong, G. An optimization research on the coverage of micro-textures arranged on bearing sliders. *Tribology International* **2018**, *128*, 231–239, doi:10.1016/j.triboint.2018.07.033.
116. Shen, Z.; Li, S.; Wu, Z.; Dong, B.; Luo, W.; Zeng, L. Optimization design of irregular grooved texture on the surface of sliding pair based on adaptive genetic algorithm. *ILT* **2023**, *75*, 1208–1218, doi:10.1108/ILT-06-2023-0196.
117. Xu, S.; Nguyen, V.; Guo, X.; Yuan, H. Lubrication efficiency of crankpin bearing using square-cylindrical textures of partial textures optimized by genetic algorithm. *ILT* **2021**, *73*, 1248–1257, doi:10.1108/ILT-07-2021-0284.
118. Khatri, C.B.; Yadav, S.K.; Thakre, G.D.; Rajput, A.K. Design optimization of vein-bionic textured hydrodynamic journal bearing using genetic algorithm. *Acta Mech* **2024**, *235*, 167–190, doi:10.1007/s00707-023-03734-9.
119. Konak, A.; Coit, D.W.; Smith, A.E. Multi-objective optimization using genetic algorithms: A tutorial. *Reliability Engineering & System Safety* **2006**, *91*, 992–1007, doi:10.1016/j.ress.2005.11.018.

120. Papon, A.; Riou, Y.; Dano, C.; Hicher, P.-Y. Single - and multi - objective genetic algorithm optimization for identifying soil parameters. *Num Anal Meth Geomechanics* **2012**, *36*, 597–618, doi:10.1002/nag.1019.
121. Deb, K.; Pratap, A.; Agarwal, S.; Meyarivan, T. A fast and elitist multiobjective genetic algorithm: NSGA-II. *IEEE Trans. Evol. Computat.* **2002**, *6*, 182–197, doi:10.1109/4235.996017.
122. Yu, X.; Shi, G.; Jiang, H.; Dai, R.; Jia, W.; Yang, X.; Gao, W. Effect of texture parameters on the lubrication performance of static and dynamic pressure thrust bearings and multi-objective optimization. *ILT* **2024**, *76*, 526–536, doi:10.1108/ILT-10-2023-0340.
123. Tang, H.; Ren, Y.; Kumar, A. Optimization tool based on multi-objective adaptive surrogate modeling for surface texture design of slipper bearing in axial piston pump. *Alexandria Engineering Journal* **2021**, *60*, 4483–4503, doi:10.1016/j.aej.2021.03.013.
124. Li, Q.; Wang, Y.; Zhang, S.; Xu, W.-W.; Bai, L.; Wang, Z. Investigation and optimization of textured thrust bearings with spirally distributed dimples using multi-objective optimization method. *ILT* **2020**, *72*, 749–759, doi:10.1108/ILT-10-2019-0435.
125. Li, Y.; He, Y.; Luo, J. Multi-objective optimization of surface texture shape in fluid mechanical face seals using mass-conserving cavitation boundary condition. *Proceedings of the Institution of Mechanical Engineers, Part J: Journal of Engineering Tribology* **2024**, *238*, 581–599, doi:10.1177/13506501241228890.
126. Wang, X.; Shi, L.; Huang, W.; Wang, X. A multi-objective optimization approach on spiral grooves for gas mechanical seals. *Journal of Tribology* **2018**, *140*, doi:10.1115/1.4038864.
127. Zhang, N.; Liu, Y.; Li, Z.; Zhan, X. Sealing performance and optimization design of squamous textured mechanical seal. *Tribology International* **2024**, *193*, 109425, doi:10.1016/j.triboint.2024.109425.
128. Zhang, N.; Liu, Y.; Fan, C. Multi-objective optimization design on squamous texture for the sealing performance **2024**, *155*, 1035–1043, doi:10.1007/978-981-97-0922-9\_65.
129. OpenFOAM®. Available online: <https://www.openfoam.com/governance/overview>.
130. Greenshields, C.J.; Weller, H.G. *Note on computational fluid dynamics: General principles*; CFD Direct <https://cfd.direct>: Royaume-Uni, 2022, ISBN 978-1-3999-2078-0.
131. Dobrica, M.B.; Fillon, M.; Maspeyrot, P. Mixed elasto-hydrodynamic lubrication in a partial journal bearing—Comparison between deterministic and

- stochastic models. *Journal of Tribology* **2006**, *128*, 778–788, doi:10.1115/1.2345404.
132. Meng, F.; Chen, Y. Analysis of elasto-hydrodynamic lubrication of journal bearing based on different numerical methods. *Industrial Lubrication and Tribology* **2015**, *67*, 486–497, doi:10.1108/ILT-03-2015-0026.
133. Wang, Q.J.; Zhu, D. *Interfacial mechanics: Theories and methods for contact and lubrication*; CRC Press: First edition. | Boca Raton, FL : CRC Press/Taylor & Francis Group, 2019.
134. Wang, W.; Chen, H.; Hu, Y.; Wang, H. Effect of surface roughness parameters on mixed lubrication characteristics. *Tribology International* **2006**, *39*, 522–527, doi:10.1016/j.triboint.2005.03.018.
135. Greenwood, J.A.; Tripp, J.H. The contact of two nominally flat rough surfaces. *Proceedings of the Institution of Mechanical Engineers* **1970**, *185*, 625–633, doi:10.1243/PIME\_PROC\_1970\_185\_069\_02.
136. Hu, Y.; Cheng, H.S.; Arai, T.; Kobayashi, Y.; Aoyama, S. Numerical simulation of piston ring in mixed lubrication—A nonaxisymmetrical analysis. *Journal of Tribology* **1994**, *116*, 470–478, doi:10.1115/1.2928867.
137. Bonneau, D.; Fatu, A.; Souchet, D. Mixed lubrication in hydrodynamic bearings **2014**, doi:10.1002/9781119004905.
138. Leighton, M.; Rahmani, R.; Rahnejat, H. Surface-specific flow factors for prediction of friction of cross-hatched surfaces. *Surf. Topogr.: Metrol. Prop.* **2016**, *4*, 25002, doi:10.1088/2051-672X/4/2/025002.
139. Patir, N.; Cheng, H.S. An average flow model for determining effects of three-dimensional roughness on partial hydrodynamic lubrication. *Journal of Lubrication Technology* **1978**, *100*, 12–17, doi:10.1115/1.3453103.
140. Patir, N.; Cheng, H.S. Application of average flow model to lubrication between rough sliding surfaces. *Journal of Lubrication Technology* **1979**, *101*, 220–229, doi:10.1115/1.3453329.
141. Morris, N.J.; Shahmohamadi, H.; Rahmani, R.; Rahnejat, H.; Garner, C.P. Combined experimental and multiphase computational fluid dynamics analysis of surface textured journal bearings in mixed regime of lubrication. *Lubrication Science* **2018**, *30*, 161–173, doi:10.1002/lc.1414.
142. Mohiuddin Mala, G.; Li, D. Flow characteristics of water in microtubes. *International Journal of Heat and Fluid Flow* **1999**, *20*, 142–148, doi:10.1016/S0142-727X(98)10043-7.
143. Weilin, Q.; Mohiuddin Mala, G.; Dongqing, L. Pressure-driven water flows in trapezoidal silicon microchannels. *International Journal of Heat and Mass Transfer* **2000**, *43*, 353–364, doi:10.1016/S0017-9310(99)00148-9.

- 
144. Ji, Y.; Liu, F.; Li, X.; Li, J. Effect of surface roughness on laminar flow in closed channels. *Physics of Fluids* **2022**, *34*, doi:10.1063/5.0078368.
  145. Wang, Y.; Lei, Z.; Xu, Z.; Liu, Y.; Zhou, Q.; Liu, P. Occurrence and flow behavior for oil transport in mixed wetting nanoscale shale bedding fractures. *Langmuir* **2024**, *40*, 14399–14412, doi:10.1021/acs.langmuir.4c00983.
  146. Lv, F.; Jiao, C.; Ta, N.; Rao, Z. Mixed-lubrication analysis of misaligned bearing considering turbulence. *Tribology International* **2018**, *119*, 19–26, doi:10.1016/j.triboint.2017.10.030.
  147. Sander, D.E.; Allmaier, H.; Pribsch, H.H.; Witt, M.; Skiadas, A. Simulation of journal bearing friction in severe mixed lubrication – Validation and effect of surface smoothing due to running-in. *Tribology International* **2016**, *96*, 173–183, doi:10.1016/j.triboint.2015.12.024.
  148. Moukalled, F.; Mangani, L.; Darwish, M. *The Finite Volume Method in Computational Fluid Dynamics: An Advanced Introduction with OpenFOAM® and Matlab*, 1st ed. 2016; Springer International Publishing; Imprint: Springer: Cham, 2016, ISBN 978-3-319-16874-6.
  149. Bürger, M.; Wang, Y.; Litwin, W.; Wasilczuk, M.; Wodtke, M.; Jacobs, G.; König, F.; Reimers, M. Potentials and risks of using EALs in Marine Stern Tube bearings – an experimental and numerical study (under review) **2025**.
  150. Niu, Y.; Hao, X.; Xia, A.; Wang, L.; Liu, Q.; Li, L.; He, N. Effects of textured surfaces on the properties of hydrodynamic bearing. *The International Journal of Advanced Manufacturing Technology* **2022**, *118*, 1589–1596, doi:10.1007/s00170-021-08022-1.
  151. Mathworks Matlab. Latin hypercube sample. Available online: <https://de.mathworks.com/help/stats/lhsdesign.html>.
  152. Marian, M.; Mursak, J.; Bartz, M.; Profito, F.J.; Rosenkranz, A.; Wartzack, S. Predicting EHL film thickness parameters by machine learning approaches. *Friction* **2023**, *11*, 992–1013, doi:10.1007/s40544-022-0641-6.
  153. Tošić, M.; Marian, M.; Habchi, W.; Lohner, T.; Stahl, K. Application of machine learning for film thickness prediction in elliptical EHL contact with varying entrainment angle. *Tribology International* **2024**, *199*, 109940, doi:10.1016/j.triboint.2024.109940.
  154. Walker, J.; Questa, H.; Raman, A.; Ahmed, M.; Mohammadpour, M.; Bewsher, S.R.; Offner, G. Application of tribological artificial neural networks in machine elements. *Tribology Letters* **2023**, *71*, doi:10.1007/s11249-022-01673-5.
  155. Cardenas, L.L.; Mezher, A.M.; Barbecho Bautista, P.A.; Astudillo Leon, J.P.; Igartua, M.A. A multimetric predictive ANN-based routing protocol for
-

- vehicular ad hoc networks. *IEEE Access* **2021**, *9*, 86037–86053, doi:10.1109/ACCESS.2021.3088474.
156. Mathworks Matlab. Levenberg-Marquardt backpropagation. Available online: <https://de.mathworks.com/help/deeplearning/ref/trainlm.html>.
157. Ostasevicius, V.; Paleviciute, I.; Paulauskaite-Taraseviciene, A.; Jurenas, V.; Eidukynas, D.; Kizauskiene, L. Comparative analysis of machine learning methods for predicting robotized incremental metal sheet forming force. *Sensors* **2021**, *22*, doi:10.3390/s22010018.
158. Benardos, P.G.; Vosniakos, G.-C. Optimizing feedforward artificial neural network architecture. *Engineering Applications of Artificial Intelligence* **2007**, *20*, 365–382, doi:10.1016/j.engappai.2006.06.005.
159. Chang, Y.-T.; Lin, J.; Shieh, J.-S.; Abbod, M.F. Optimization the initial weights of artificial neural networks via genetic algorithm applied to hip bone fracture prediction. *Advances in Fuzzy Systems* **2012**, *2012*, doi:10.1155/2012/951247.
160. Pu, Y.; Apel, D.B.; Wei, C. Applying machine learning approaches to evaluating rockburst liability: A comparison of generative and discriminative models. *Pure and Applied Geophysics* **2019**, *176*, 4503–4517, doi:10.1007/s00024-019-02197-1.
161. Abdolrasol, M.G.M.; Hussain, S.M.S.; Ustun, T.S.; Sarker, M.R.; Hannan, M.A.; Mohamed, R.; Ali, J.A.; Mekhilef, S.; Milad, A. Artificial neural networks based optimization techniques: A review. *Electronics* **2021**, *10*, 2689, doi:10.3390/electronics10212689.
162. Qiu, M.; Song, Y. Predicting the direction of stock market index movement using an optimized artificial neural network model. *PLoS One* **2016**, *11*, e0155133, doi:10.1371/journal.pone.0155133.
163. Katoch, S.; Chauhan, S.S.; Kumar, V. A review on genetic algorithm: past, present, and future. *Multimed. Tools Appl.* **2021**, *80*, 8091–8126, doi:10.1007/s11042-020-10139-6.
164. Boga, C.; Koroglu, T. Proper estimation of surface roughness using hybrid intelligence based on artificial neural network and genetic algorithm. *Journal of Manufacturing Processes* **2021**, *70*, 560–569, doi:10.1016/j.jmapro.2021.08.062.
165. IT Center of RWTH Aachen university. Partitions. Available online: <https://help.itc.rwth-aachen.de/service/rhr4fjuttff/article/9108f4a6f43c40a3a168919afd36839d/>.
166. Singh, A.; Wolf, M.; Jacobs, G.; König, F. Machine learning based surrogate modelling for the prediction of maximum contact temperature in EHL line contacts. *Tribology International* **2023**, *179*, 108166, doi:10.1016/j.triboint.2022.108166.

167. Ahmad, M.; Alkanhel, R.; El-Shafai, W.; Algarni, A.D.; El-Samie, F.E.A.; Soliman, N.F. Multi-objective evolution of strong S-Boxes using Non-Dominated Sorting Genetic Algorithm-II and Chaos for secure telemedicine. *IEEE Access* **2022**, *10*, 112757–112775, doi:10.1109/ACCESS.2022.3209202.
168. Martins, J.R.R.A.; Ning, A. *Engineering Design Optimization*; Cambridge University Press, 2022.
169. Deb, K.; Pratap, A.; Agarwal, S.; Meyarivan, T. A fast and elitist multiobjective genetic algorithm: NSGA-II. *IEEE Trans. Evol. Computat.* **2002**, *6*, 182–197, doi:10.1109/4235.996017.
170. Li, H.; Zhang, Q. Multiobjective optimization problems with complicated Pareto sets, MOEA/D and NSGA-II. *IEEE Trans. Evol. Computat.* **2009**, *13*, 284–302, doi:10.1109/TEVC.2008.925798.
171. Feldermann, A.; Neumann, S.; Jacobs, G. CFD simulation of elastohydrodynamic lubrication problems with reduced order models for fluid–structure interaction. *Tribology - Materials, Surfaces & Interfaces* **2017**, *11*, 30–38, doi:10.1080/17515831.2017.1279846.
172. Wallis, G.B. *One-dimensional two-phase flow*; Dover Publications Inc: Garden City New York, 2020, ISBN 9780486842820.
173. Beheshti, A.; Khonsari, M.M. An engineering approach for the prediction of wear in mixed lubricated contacts. *Wear* **2013**, *308*, 121–131, doi:10.1016/j.wear.2013.10.004.